Title
Biosensors for Mitochondrial Membrane Potential Analysis

Author
Zand, Katayoun

Publication Date
2014

Peer reviewed|Thesis/dissertation

UNIVERSITY OF CALIFORNIA,
IRVINE

Biosensors for Mitochondrial Membrane Potential Analysis

DISSERTATION

submitted in partial satisfaction of the requirements
for the degree of

DOCTOR OF PHILOSOPHY

in Electrical Engineering and Computer Science

by

Katayoun Zand

Thesis Committee:
Professor Peter John Burke, Chair
Professor Abraham Lee
Professor Kumar Wickramasinghe

2014

Table of Contents

LIST OF FIGURES

Page

LIST OF TABLES

Page

LIST OF ABBREVIATIONS

$\Delta\psi_m$ – mitochondrial membrane potential

ADP – adenosine diphosphate

AFM – atomic force microscope

APTES - (3-Aminopropyl)triethoxysilane

ATP – adenosine triphosphate

BSA – Bovine serum albumin

C – Centigrade

CCCP - Carbonyl cyanide *m*-chlorophenyl hydrazone

CCD – charge-coupled device

CNT – carbon nanotube

CNTFET – carbon nanotube field effect transistor

DMSO –dimethyl sulfoxide solution

DNA – deoxyribonucleic acid

ETC – electron transport chain

Heb7A – HeLa-derived cell line

HMDS – Hexamethyldisilazane

IPA – Isopropanol

ISE – ion-selective electrode

min – minute

MMP – mitochondrial membrane permeabilization

MTG – MitoTracker Green

mtDNA – mitochondrial DNA

mtPTP – mitochondrial permeability transition pore

NADH – nicotinamide adenine dinucleotide (reduced)

ND1 and ND2 – NADH dehydrogenase subunit 1 and 2

OXPHOS – oxidative phosphorylation

PDMS - Polydimethylsiloxane

Pi – inorganic phosphate

PM – pyruvate and malate

PTP – permeability transition pore

PVC – Polyvinyl chloride

redox – reduction-oxidation

ROS – reactive oxygen species

Si- Silicon

SNR – signal to noise ratio

SWCNT – single walled carbon nanotube

THF - Tetrahydrofuran

TMRE – tetramethylrhodamine ethyl ester

TMRM – tetramethylrhodamine methyl ester

TPP^+ - tetraphenylphosphonium

ACKNOWLEDGMENTS

First and foremost I would like to thank my dissertation advisor, Professor Peter Burke. Without his invaluable advice and persistent help this dissertation would not have been possible. I also wish to express my gratitude to Professor Douglas Wallace for his precious advice and support. I would like to thank my committee members, for their valuable discussions, advices and efforts on my dissertation.

The members of UCI Nanotechnology group have contributed immensely to my time at UC Irvine. The group has been a source of friendships as well as good advice and collaboration. Thanks to Tae-Sun Lim, Ted Pham, Nima Rouhi, Dheeraj Jain, Will Wang, Weiwei Zhou, Phi Pham and Jinfeng Li. I am also grateful to the team of INRF, and staff members at the Electrical Engineering department and Clait2 facility at UC Irvine.

Lastly, I would like to thank my parents and my two brothers for all their love and encouragement and most of all my loving and patient husband Tooraj, whose support during the course of this Ph.D. is so appreciated.

I thank the RCS and ACS for permission to include the published articles in chapters 2 and 3 of my dissertation.

CURRICULUM VITAE

Katayoun Zand

Education

University of California-Irvine (Summer 2014)

Ph.D., Electrical Engineering, Semiconductor Devices and Nano-electronics, GPA: 3.98

University of Tehran

M.Sc. Electrical Engineering (Oct 2008), Semiconductor Devices and Materials, GPA: 3.74

B.Sc. Electrical Engineering (June 2006), Electronics

Research and work Experience

University of California-Irvine

Graduate Student Researcher (Sep. 2009-Present)

Integrated Nanosystems Research Facility (INRF), UCI Nanotechnology Lab

- Engineered the first microfluidic platform with integrated carbon nanotube transistors for capacitive sensing of the membrane potential of single mitochondria. Designed, fabricated and tested microfluidic devices for fluorescence interrogation of individual mitochondria (in collaboration with researchers from Center for Mitochondrial and Epigenomic Medicine in Children's Hospital of Philadelphia)

University of Tehran

Research Assistant (Jan. 2007-December 2008)-Thin Film and Nanoelectronics Laboratory

- Fabricated flexible plasma display panels on polymer substrates . Studied surface modification of Polyethylene terephthalate (PET) substrates, Improved permeability of PET by 4 times using Hydrogen plasma treatment

Peimann Khotoot Gostar Co.

Internship, (Summer 2004)

- Worked on Supervisory Control and Data Acquisition (SCADA) systems

Awards and Honors

- UCI Henry Samueli school of Engineering student research and travel grant award (Feb. 2013)
- Orange County Engineering Council Outstanding Student Award (Feb. 2012)
- University of California Irvine EECS Fellowship award (2009)
- Ranked 2nd among Semiconductor Device graduate Students in University of Tehran (2008)
- Ranked 617 among 450000 participants of Iranian nationwide university entrance exam (2001)

In The News (Research highlighted in high-ranked news and media)

- "Spying On Subcellular Structures", ACS C&EN News, May 2013
- "Tuning In to Graphene", Communications of the ACM, October 2013
- "Tangled Nanotubes Make Speedy Transistors" , IEEE Spectrum, July 2011

Publications and Talks

Journals:

[1] **K. Zand**, T. Pham, W. Zhou, P. Burke, "Resistive Flow Sensing of Vital Mitochondria with Nanoelectrodes", Preprint

[2] **K. Zand**, T. Pham, A. Davilla, P. Burke, D. Wallace, "Nanofluidic Platform for Single Mitochondria Analysis Using Fluorescence Microscopy", Analytical Chemistry, DOI: 10.1021/ac4010088 (2013)

[3] Y. Wang, T. D. Pham, **K. Zand**, P. J. Burke, "Charging the Quantum Capacitance of Graphene with a Single Biological Ion Channel", ACSNano, DOI: 10.1021/nn501376z, (2014)

[4] T. Lim, A. Dávila, **K. Zand**, D. Wallace, P. Burke, "Wafer-scale mitochondrial membrane potential assays", Lab Chip, 12, DOI: 2719-2725 (2012)

[5] N. Rouhi, D. Jain, **K. Zand**, P. J. Burke, "Fundamental Limits on the Mobility of Nanotube-Based Semiconducting Inks", Advanced Materials, DOI: 10.1002/adma.201003281 (2010).

[6] N. Rouhi, S. Capdevila, D. Jain, **K. Zand**, Y. Wang, E. Brown, L. Jofre, P. Burke, "Terahertz Graphene Optics", Nano Research, DOI: 10.1007/s12274-012-0251-02 (2012)

[7] Z. Sanaee, S. Mohajerzadeh, **K. Zand**, F. S. Gard and H. Pajouhi, "Minimizing permeability of PET substrates using Oxygen plasma treatment," Journal of Applied Surface Science, Volume 96, Issue 20, pp. 2218-2225 (2011)

[8] Z. Sanaee, **K. Zand**, S. Mohajerzadeh and F. S. Gard, "Improved permeability of PET substrates using oxygen and hydrogen Plasma," Journal of Vacuum, Volume 85, pp 290-296, (2010)

Conferences:

[1] **K. Zand**, T. Pham, A. Davila Jr, D. C. Wallace, P. Burke," Nanochannel Devices for Single Mitochondrion Membrane Potential Assays" MRS Spring meeting 2014, April 2014, San Francisco, CA.

[2] **K. Zand**, T. Pham, A. Davila Jr, D. C. Wallace, P. Burke, "Nanochannel Trap Arrays For Monitoring Single Mitochondrion Behavior", Biophysical Society 58th Annual Meeting, February 2014, San Francisco, CA.

[3] **K. Zand**, T. Pham, A. Davila Jr, D. C. Wallace, P. Burke, "Trapping And Study Of Individual Mitochondria Using Nanofluidic Technology" Mitochondrion 13 (6), 943

[4] **K. Zand**, T. Pham, A. Davila Jr, D. C. Wallace, P. Burke, "Novel Approach Towards Trapping and Imaging of Individual Mitochondria", MMB 2013 Technical Digest, April 2013, Marina del Rey, CA

[5] N. Rouhi, D. Jain, **K. Zand**, and P. Burke, "Performance Control of High Mobility, Printed Thin Film Transistors using Semiconducting Nanotube Ink", MRS Spring meeting 2011, April 2011, San Francisco, CA.

[6] D. Jain, N. Rouhi, **K. Zand**, P. Burke, "All-Semiconducting nanotube networks Thin Film Transistors: An insight towards High Performance Printed Nanoelectronics", Bulletin of the American Physical Society, March 2011, Dallas, TX

[7] N. Rouhi, D. Jain, **K. Zand**, P. J. Burke, "All-semiconducting Nanotube Networks: Towards High Performance Printed Nanoelectronics", MRS fall meeting 2010, November 2010, Boston, MA, USA.

[8] N. Rouhi, D. Jain, **K. Zand**, P. J. Burke, "Semiconducting-Enriched Printed Carbon Nanotube Mat used for Fabrication of Thin Film Transistors", IEEE NANO 2010, (2010)

[9] N. Rouhi, D. Jain, **K. Zand**, P. J. Burke, " Semiconductor-Enriched Carbon Nanotube Thin Film Transistors", International Symposium on Spectral Sensing Research (ISSSR 2010), June 2010, Springfield, MO, USA.

[10] N. Rouhi, D. Jain, **K. Zand**, P. J. Burke, "Carbon Nanotube Field Effect Transistors using Printed Semiconducting Tubes", NSTI-Nanotech (2010)

[11] N. Rouhi, D. Jain, **K. Zand**, P. J. Burke, "All-Semiconducting Nanotube Devices for RF and Microwave Applications", International Microwave Symposium Digest (MTT), 2010 IEEE MTT-S (2010)

[12] Z. Sanaee , **K. Zand**, P.Saber and S. Mohajerzadeh, "Plasma Treatment of PET Substrates to Reduce Air Penetration in Sub-Atmospheric and Vacuum Devices", 3rd Iranian Vacuum Conference, 2008 (in Persian)

[13] K.Baghbani Parizi, **K. Zand**, M.Fathipour, "Investigation of Effects of Cell Size and Asymmetric Arrangement on Performance and Meta-Stable Energy of Quantum-Dot Cellular Automata", Iranian Physics Conference, 2008 (in Persian)

[14] Z. Sanaee , **K. Zand** , S. Mohajerzadeh , N. Zehforoush , S. Darbari and A. Akhavan, "Realization of Flexible Lateral Pixels on PET Substrates for DC-PDP Structures", Eurodisplay'07 Proceedings (2007)

Invention Disclosures

[1] P. Burke, Y. Wang, **K. Zand**, T. Pham, "Graphene Supported Lipid Bilayer Platform For Detecting Single Ion Channel Activity", UC Case No. 2013-729-1, July 29, 2013

[2] P. Burke, **K. Zand**, T. Pham, T. Lim, A. Davila, D. Wallace "NANOFLUIDIC PLATFORM FOR SINGLE MITOCHONDRIA ANALYSIS" , UC Case No. 2013-063-1, August 20, 2012

[3] P. Burke, T. Lim, A. Davila, D. Wallace, **K. Zand**, "DEVICE AND METHOD FOR MITOCHONDRIAL MEMBRANE POTENTIAL ASSESSMENT", UC Case No. 2010-851-2, March 5, 2012

Book Chapters

[1] Ted Pham**, Katayoun Zand**, Douglas Wallace, Peter Burke, "Fluorescence Analysis of Single Mitochondria with Nanofluidic Channels" ,(to be published) in Volkmar Weissig, Mitochondrial Medicine: Methods and Protocols, Springer

ABSTRACT OF THE DISSERTATION

Biosensors for Mitochondrial Membrane Potential Analysis

By

Katayoun Zand

Doctor of Philosophy in Electrical Engineering and Computer Science

University of California, Irvine, 2014

Professor Peter Burke, Chair

New generation of biosensors based on nanofabrication techniques show great promise for clinical analysis, diagnosis of diseases and drug discovery. One of the areas in which development of new techniques and technologies is crucial is the field of analysis of individual sub-cellular organelles. Mitochondria not only produce cellular energy, they are also involved in cellular signaling and control the cell fate. Mitochondrial dysfunction is implicated in many human diseases; development of new technologies for mitochondrial analysis is essential to understanding the mechanism of these illnesses and finding a cure for them.

During the course of this research, three different types of devices for analyzing mitochondria were designed, fabricated and characterized. First a miniaturized on-chip ion-selective device for mitochondrial membrane potential assays was developed. This

device facilitates mitochondrial evaluations when the available mitochondrial sample is very small and therefore commercial sensors cannot be used. The second device is a Nanofluidic platform to trap individual mitochondria and is extremely useful for fluorescence microscopy studies of different characteristics of individual mitochondria. Single mitochondrion membrane potential studies were demonstrated using this device. Finally, a novel method was developed for mitochondrial studies; this method is based on capacitive sensing of individual mitochondrion's membrane potential using carbon nanotube transistors integrated into a microfluidic channel. Assays of mitochondrial membrane potential using the prototype device is presented and shows unprecedented temporal resolution compared to prior studies.

CHAPTER 1 : INTRODUCTION

Mitochondria

Mitochondria are semiautonomous organelles inside eukaryotic cells and are the main regulators of bioenergetics in a cell. Adenosine triphosphate (ATP), a nucleoside triphosphate, is produced by mitochondria and is responsible for transport of chemical energy within the cell. It is used by enzymes and proteins to energize different cellular processes.[1] Because of the major role of mitochondria in production of ATP, they are usually nicknamed as "the powerhouse of the cell".

Mitochondria have two phospholipid bilayer membranes (Figure 1.1). The outer membrane that encloses the organelle has numerous pores and is permeable to most molecules up to 5000 daltons. The inner membrane separates the intermembrane space from the protein-rich matrix. Most of the enzymatic machinery of ATP generation is located in the inner membrane. This membrane is compartmentalized and the folds are referred to as cristae. This morphology results in a high surface area and therefore more working space.

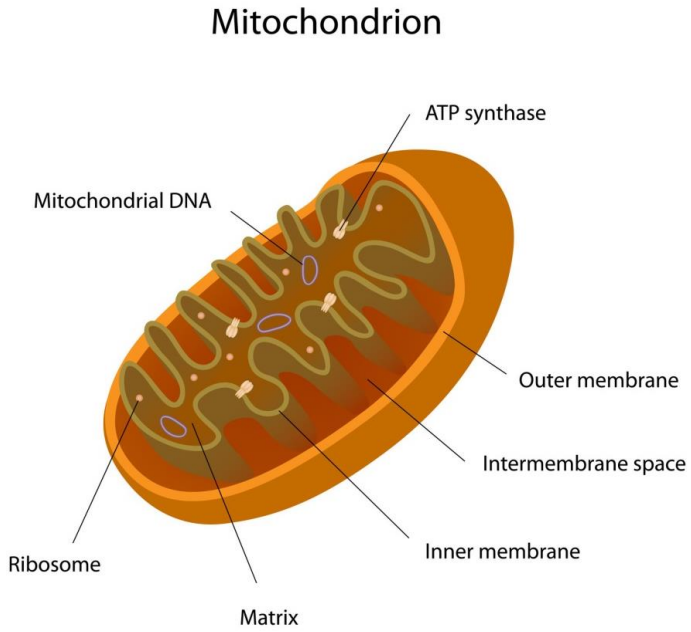

Figure 1.1. Structure of a mitochondrion.

Unlike the outer membrane the inner membrane is permeable only to water and oxygen. Specific molecules can cross the membrane through sophisticated ion transporters.[2] This impermeability isolates the matrix from the cytosolic environment chemically and electrically and is essential for conversion of energy from substrates to ATP. Mitochondria retain their own genome, which allows the synthase of proteins essential for mitochondrial respiration. Mitochondrial DNA encodes only a small number of genes compared to the nucleus DNA.

Mitochondria are involved in other processes such as fatty acid synthesis, regulation of cellular Ca^{+2} concentration, [3] and cellular signaling pathways.[4] Mitochondria affect the cellular signaling in two ways: by serving as a platform on which protein-protein interactions occur, and by adjusting the concentration of intracellular signaling molecules such as Ca^{+2} and ROS (reactive oxygen species).[3] Calcium ions are important signaling molecules and are involved in a variety of physiological roles such as muscle contraction and neuronal transmission. Mitochondria influence the interacellular calcium concentration by sequestering Ca^{+2} from the cytosol through a channel in the inner membrane known as the mitochondria calcium uniporter or releasing Ca^{+2} into cytosol though ion exchangers NCX and HCX that exchange calcium ions with Na^{+} and H^{+} respectively.[5]

Mitochondria control the fate of the cell through a process known as apoptosis or programmed cell death. Cells can commit suicide by activating an intracellular death program. In adult tissue the cell death rate should exactly balance the cell division, otherwise the tissue will grow or shrink.[6] The intracellular death pathway is triggered by factors such as toxic chemicals, mechanical cell injury, radiation, increased Ca^{+2} levels, *etc*. Once this pathway is activated, specific proteins known as BAX and BAK migrate to mitochondrial

surface and permeabilize the mitochondrial membrane; this releases the contents of the matrix, including the electron carrier protein, cytochrome c and SMAC in to the cytosol. Release of cytochrome c activates caspases, which bring about cell death (Figure 1.2).[7]

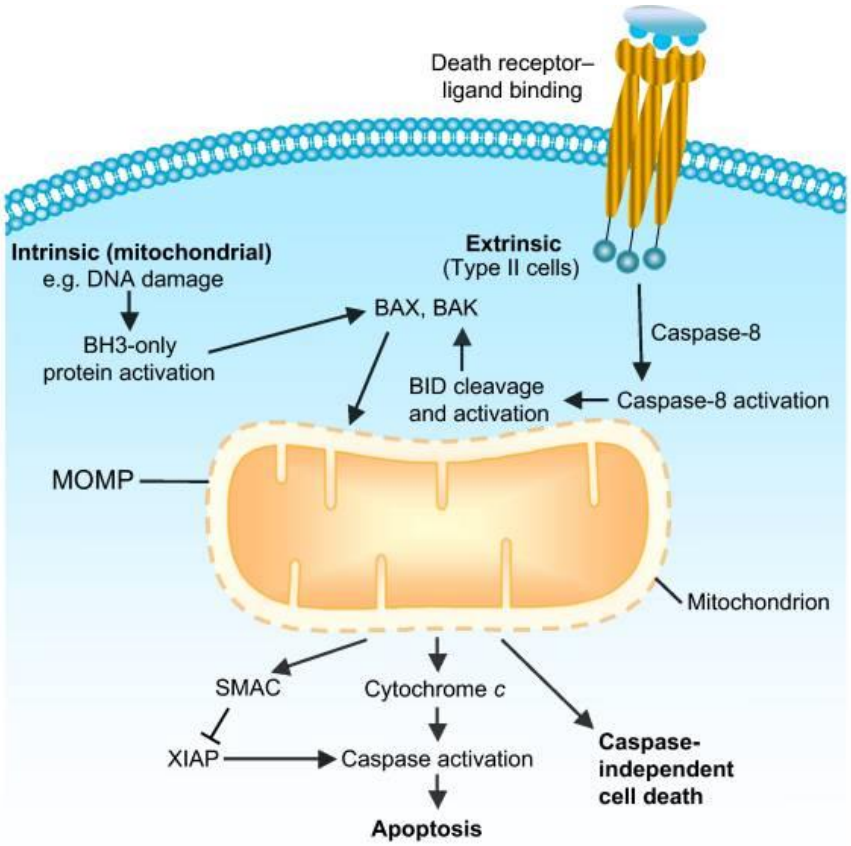

Figure 1.2. Mitochondrial regulation of apoptosis. (Reproduced from[3])

Oxidative Phosphorylation and Membrane Potential

Oxidative phosphorylation is the metabolic pathway through which mitochondria generate ATP. Mitochondria need a flow of respiratory substrates across the membrane into the matrix. These substrates are used by the Krebs cycle, a metabolic pathway formed mainly by enzymes inside the mitochondrial matrix to oxidize acetyl-CoA and generate NADH and $FADH_2$ as byproducts. The inner mitochondrial membrane houses a chain of five protein complexes that form the mitochondrial respiratory chain. As a result of the redox

reactions through these protein compounds, electrons from the byproducts of the Krebs cycle, are transferred in small steps to oxygen, forming water. As electrons are passed from one carrier to another, protons are pumped into the intermembrane space. These protons are pumped by complexes I, III and IV. This creates a strong hydrogen concentration gradient. This electrochemical gradient is known as proton motive force (Δp) and has two components. An electrical potential across the membrane $(\Delta\psi_m)$ and a pH component (ΔpH_m). At 37^o C, Δp can be represented as:

$$\Delta p = \Delta\psi_m - 60\Delta pH_m \qquad \text{(Equation 1.1)}$$

Some typical values for these parameters are, 150 mV for $\Delta\psi_m$, -0.5 for ΔpH_m, and 180 mV for Δp.[8] The proton motive force energizes the phosphorylation of ADP to ATP through the F_0F_1 ATP synthase (complex V). This process is called oxidative phosphorylation or OXPHOS (Figure 1.3). The ATP is then transported out of the mitochondria to energize different cellular functions.

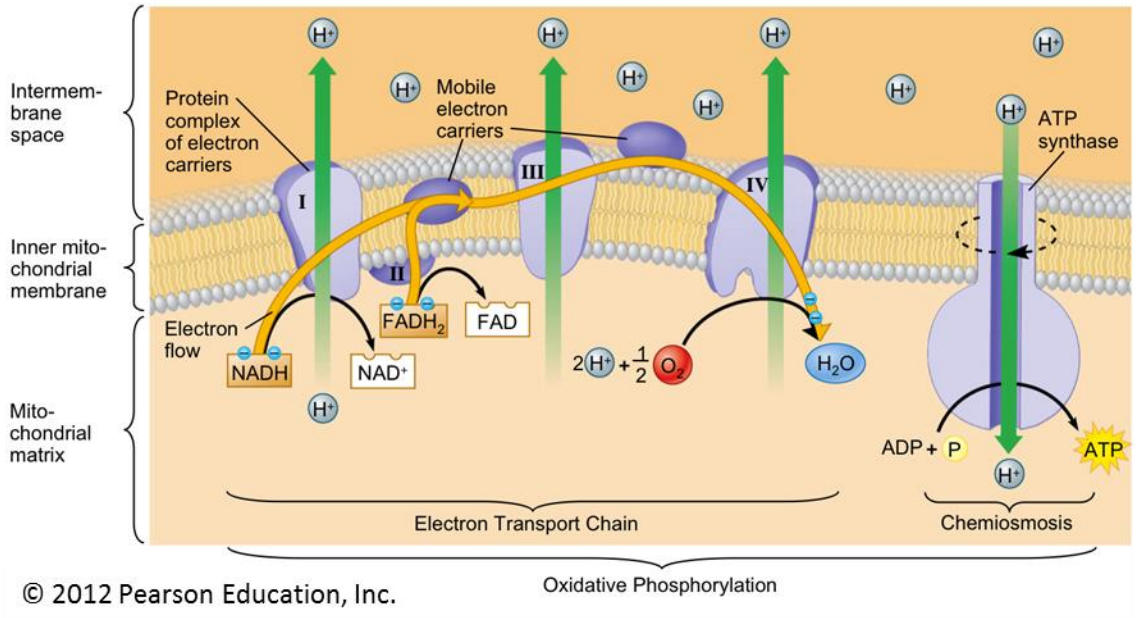

Figure 1.3. Oxidative Phosphorylation in mitochondria inner membrane. (downloaded from: http://www.unm.edu/~lkravitz/Exercise%20Phys/ETCstory.html)

Membrane potential is an important physiologic parameter of mitochondria and regulates all the major bioenergetic functions of the organelle including ATP production and calcium accumulation. It provides a force to drive the influx of ions including Ca^{+2} into the matrix. Loss of the membrane potential may indicate several different mechanisms, including deprivation of respiratory substrates, inhibition of respiration or some kind of uncoupling mechanism that dissipated the proton gradient by permeabilizing the membrane to protons.

Mitochondria Respiratory States

The mitochondrial respiration rate is controlled by the proton motive force; the lower proton gradients, the energy required to move protons across the membrane is smaller so the respiration rate is higher. Inhibition of ATP synthase, results in an increase in the membrane potential and slower respiration. Therefore the mitochondrial ATP production and respiratory rate are coupled through the membrane potential.[9]

In isolated mitochondria respiration experiments, information on mitochondrial processes can be obtained by arranging the incubation conditions in a way that a specific step becomes dominant in determining the overall rate of the process. For experiments measuring the respiration rate of mitochondria, Chace and Williams proposed[10] a protocol for typical order of addition of agents during an experiment. Different variations of this protocol have been proposed. One conventional protocol that is commonly used is given in[11] and reproduced in Table 1.1:

Table 1.1. Definition of mitochondrial respiratory states. (Reproduced from [11])

State 1: mitochondria alone (in the presence of Pi)
State 2: substrate added, respiration low due to lack of ADP
State 3: a limited amount of ADP added, allowing rapid respiration
State 4: All ADP converted to ATP, respiration slows
State 5: Anoxia

This protocol starts with addition of mitochondria to a respiration buffer containing inorganic phosphate. Due to lack of substrates respiration rate and membrane potential are low in this state. In state 2 respiratory substrates (such as Pyruvate/Malate or Succinate) are added, this increases the membrane potential but respiration rate is still low due to lack of ADP. Addition of ADP changes the mitochondrial state to 3, where respiration is high, membrane potential is still high but lower than state 3. Once all the ADP is consumed mitochondria transition to state 4 and respiration slows down. Finally respiration becomes oxygen limited.

Mitochondria and Disease

A wide range of degenerative disease symptoms ranging from neurodegenerative disorders such as Alzheimer's disease to diabetes and various cancers have been linked to mitochondrial disorders.[12]

Mitochondrial dysfunction can be result of mutations in mitochondrial DNA (mtDNA). Each mitochondrion contains several copies of the mtDNA and a cell contains numerous mitochondria. So each cell has many copies of the mtDNA. The mtDNA has a high sequence evolution rate which results in the formation of a large number of deleterious mutations. As a

result mtDNA population in the same cell is heterogeneous, therefore mitochondria are heteroplasmic. When the percentage of mtDNA copies in a cell that carry a mutation exceeds a threshold (about 50-60%), the cell will show signs of mitochondrial dysfunction. Consequently, diseases of the mitochondria have a delayed-onset and progressive course.[13] The mtDNA mutations are associated with numerous disorders including stroke, dementia, heart failure, pneumonia, diabetes, and a variety of other diseases.[14]

Also there is evidence that mitochondria play a role in the progression of both aging-related complex diseases[13] and cancer. Mitochondria are the main producers of reactive oxygen species. One effect of the oxidative phosphorylation process is the generation of unpaired electrons. The leak of electrons seems to be linked to the membrane potential. Higher membrane potential results in generation of a higher number of unpaired electrons.[15] These unpaired electrons react with O_2 and generate highly reactive free radicals. Although mitochondrial ROS molecules have signal transduction purposes; ROS can also damage the cell membranes and the DNA, including the mitochondrial DNA (mtDNA). Therefore mitochondria itself is a major target of the ROS. It is believed that mitochondrial ROS is a major source of cellular damage that accumulates over time and might be responsible for aging.

1 in 200 individuals is thought[16] to harbor deleterious mutations in their mitochondrial genes, which do not present clinically, because of the heterogeneity of mitochondrial genome. Investigation of this heterogeneity presents many unmet challenges to scientists. Development of novel technologies is necessary to aid the discovery of underlying genetic mechanisms that link mitochondria to different diseases.

Standard Methods for Membrane Potential Measurement

The two main conventional methods of mitochondrial membrane potential assessment are electrochemical methods and fluorescence probes. These methods are based on assays of the distribution of lipophilic probe ions across the mitochondria membrane.[17–19]

Electrochemical method, used for isolated mitochondria, takes advantage of a reference electrode and an ion-selective working electrode. The two electrodes are inserted inside a medium that contains a known concentration of the lipophilic cation. Once isolated mitochondria are added to the buffer, depending on the membrane potential of the mitochondria, some of the lipophilic ions diffuse into the mitochondrial matrix. The concentration ratio is related to $\Delta\Psi_m$ through the Nernst equation:

$$\Delta\Psi_m = 2.303\frac{RT}{zF}\log\frac{[C_{out}]}{[C_{in}]} \qquad \text{(Equation 1.2)}$$

Where C_{in} and C_{out} are ion concentrations inside the mitochondria and in the respiration buffer, T the temperature, z the charge on the ion, F the Faraday's constant and R the ideal gas constant, respectively. Due to redistribution of the lipophilic ions into mitochondria, the concentration of these ions in the medium decreases. This change in the concentration is detectable through the change in the voltage across the working and reference electrodes. The change in the lipophilic ion concentration indicates the amount of ions that have diffused into mitochondria, and it is possible to find the membrane potential through the Nernst equation. This method is precise and renders quantifiable data. However, commercial ion-selective membrane potential electrodes are commonly used when a large amount of isolated mitochondria are available but are not suitable for experiments where only a small amount of sample is available. Examples of such samples where the commercially available electrodes are not suitable are human embryonic stem cells that are difficult to culture to large quantities and biopsies from

patients. The advantages and drawbacks of this method are discussed with more depth in chapter 2.

The fluorescence measurement method for mitochondrial membrane potential measurement follows a similar principle. Mitochondria are incubated with a voltage sensitive fluorescent dye whose intensity of fluorescence changes depends on $\Delta\psi_m$. Fluorescence intensity of the dye is detected inside and outside of the mitochondrion and the ratio is used to calculate the membrane potential from the Nernst equation. With this method the average membrane potential of a population of mitochondria can be detected using a fluorimeter. It is also possible to assay the membrane potential of individual mitochondria using a fluorescence microscope. This is a powerful method for single mitochondria studies, but has some limitation. Movement of mitochondria out of the plane of focus and background fluorescence from out of focus mitochondria are some the difficulties of this technique. The strengths and pitfalls of single mitochondria fluorescence microscopy are further discussed in chapters 3 and 4.

On Chip Devices for Mitochondrial Membrane Potential Measurement

Even though a thorough understanding of mitochondrial bioenergetics, genetics and role of mitochondria in cellular signaling pathways is crucial to recognize the causes of many human diseases and to find a cure for those illnesses, due to limitations of current technologies, such an understanding has not been obtainable. Development of novel methods and devices are essential to achieve conclusive results on the mechanisms of mitochondrial functions. This shows the need for development of innovative, advanced technologies appropriate for single mitochondrion studies.

The advent of microfluidics and nanofluidics can be utilized to address the shortcomings of traditional approaches. The ability to control fluids in small volumes enables assays requiring significantly less sample size, and the precise control delivery of chemicals makes it ideal for testing specific hypotheses involving different processes. Using microfluidics, particles can be precisely manipulated. Extensive research this decade has been advanced to assay and analyze individual cells using flow cytometry and microfluidic devices[20]. This has given rise to extraordinary technological capabilities, such as the possibility of finding one circulating tumor cell per 10^9 healthy cells in whole blood for cancer diagnosis[21]. In contrast, the field of analysis of individual sub-cellular organelles is in its infancy.

More recently biosensors based on nanomaterials such as nanowires, SWCNTs and graphene have been actively used for electrical analysis biological entities. Due to their high sensitivity to electric charge and small size which is comparable to biological entities, nanomaterials are very well suited for integration into biosensors. Devices based on nanomaterials have been used to study DNAs[22,23], single molecule dynamics[24], protein interactions[25,26], antibodies[27], viruses,[28] neuronal signals[29] and intracellular recordings[30]. But there have been very few examples of characterization of whole cells or membrane bound organelles using nanomaterials.

The goal of this work is to make use of advances in microfluidics, nanofluidics and nanotechnology to design and fabricate on chip devices for detection of mitochondrial membrane potential.

Overview of Dissertation

In this dissertation I will present my work on development of three on chip device designs for mitochondrial membrane potential studies. Chapter 1 provide a brief introduction of mitochondrial bioenergetics, importance of mitochondrial assays and motivation for this work.

Chapter 2 focuses on the working principles, design and fabrication of a novel miniaturized on-chip mitochondrial membrane potential ion-selective sensor. Using this device, the membrane potential for mitochondria isolated from various cell lines is assayed. Next I will focus on the experimental procedure and error analysis for the developed sensor.

Chapter 3 describes the fabrication and use of a Nanofluidic platform to capture and analyze individual, isolated mitochondria. Fluorescence labeling demonstrates the immobilization of mitochondria at discrete locations along the channel. Interrogation of mitochondrial membrane potential with different potential sensitive dyes indicates the trapped mitochondria are vital in the respiration buffer. This device provides a solution to some of the common difficulties in single mitochondria fluorescence microscopy.

In chapter 4, I describe label free detection of single isolated mitochondria with high sensitivity using nanoelectrodes. Electrical measurement of the conductance of carbon nanotube transistors embedded in a microfluidic channel show discrete membrane potential sensitive changes of conductance as individual mitochondria flow over the nanoelectrode in the microfluidic channel. Next I perform an analysis of the accuracy of membrane potential measurements using the new technique compared to fluorescence microscopy.

Finally, in chapter 5, I will summarize my work with a discussion about the future perspectives.

CHAPTER 2 : Wafer-scale Mitochondrial Membrane Potential Assays

Introduction

The mitochondrial membrane potential ($\Delta\Psi_m$) plays a crucial role in the production of ATP as an energy source of the cell. The electron transport chain (complex I, II, III, IV) positioned at the mitochondrial inner membrane generates this electrochemical potential gradient across the inner membrane by pumping protons through the mitochondrial inner membrane while sequentially transporting electrons through the complexes. This proton gradient is utilized by ATP synthase (complex V) to synthesize ATP from ADP and inorganic phosphate. This cycle can remain functional and constantly produce ATP to sustain the cell only when the electrochemical proton gradient is maintained at a constant level with enough available ADP. $\Delta\Psi_m$ is the key component of this electrochemical potential gradient, therefore it is important to develop instrumentation technologies to monitor $\Delta\Psi_m$ in order to efficiently evaluate mitochondrial function.[31]

Mitochondria are known to regulate cell life and death by control of apoptosis, through a critical, irreversible step involving the mitochondrial permeability transition pore (mPTP), a megapore complex triggered to open under certain conditions at both the mitochondrial inner and outer membranes.[17,32–36] Once opened, the permeability of the mitochondrial inner membrane increases drastically, causing the release of bioactive proteins including cytochrome C and the inflow of protons, resulting in an irreversible collapse of the mitochondrial membrane potential. This process is known to lead to apoptosis. In addition, malfunctions and abnormal behaviors of mitochondria are highly associated with the degenerative diseases and the aging process.[12,13]

A lipophilic cation such as tetraphenylphosphonium (TPP^+) diffuses through the mitochondrial inner membrane, the concentration ratio depending on $\Delta\Psi_m$, determined by the Nernst equation, i.e.

$$\frac{[TPP^+]_{out}}{[TPP^+]_{in}} = e^{\frac{\Delta\Psi_m}{kT}} \qquad \text{(Equation 2.1)}$$

By measuring the concentration of TPP^+ outside the mitochondria, $[TPP^+]_{out}$, using electrochemical ion selective electrode technology, one can infer the concentration of cation taken up into the mitochondria, $[TPP^+]_{in}$, to determine the membrane potential[37]. Previously, an electrochemical mitochondrial functional assay using a miniaturized on-chip mitochondrial membrane potential sensor equipped with TPP^+ ion selective electrodes was developed in Burke lab.[19] This first generation planar-type mitochondrial assay sensor showed good sensitivity and a fast response to $\Delta\Psi_m$ by monitoring the activity of TPP^+ in the sample solution. However, there were some challenges with the construction process and other factors that could limit the use of the sensor. First, the ion selective membrane was manually cut from a thin jelly membrane sheet on the glass substrate itself and then individually transferred onto an open trench of PDMS layers. This was laborious and often caused wrinkles resulting in weak bonding between the membrane and the PDMS layer and, subsequently, electrolyte leakage. This could lead to unstable sensor performance and a shorter sensor lifetime. In order to improve the production yield, we sought to evolve our fabrication approaches with new substrate materials to replace the manual, serially fabricated single sensor built upon a microscope slide with an efficient batch, parallel fabrication process based on semiconductor industry models.

Here, we demonstrate a second generation, wafer-scale lab-on-a-chip design and fabrication process for mitochondrial bioenergetic measuring which is compatible with

microfabrication technology. This product is much more efficient to produce and proves to have significantly higher reproducibility and durability than the first generation model. We use industry standard 4" silicon wafer as the substrate along with a new membrane transfer technique. Changes in the mitochondrial membrane potential of isolated mitochondria from the established human cell lines Heb7A and 143B and from mouse muscle tissue are evaluated in response to treatments with known modulators of mitochondrial function. The sensor is validated by taking the measured TPP^+ concentration, converting into $\Delta\Psi_m$ and calibrating against the theoretical values. This latest sensor model improves upon all of the functional parameters of the previous version, is capable of higher throughput analysis and, importantly, is much more time and cost-effective to fabricate. This lays the foundation for low cost, high throughput screening of bioenergetics and metabolism in an on-chip format.

Methods

Fabrication steps

The microfabrication process is schematically depicted in Figure 2.1. A 4" bare silicon wafer (Boron doped P-type) was used as the device substrate to allow compatibility with standard semiconductor wafer-scale microfabrication technologies. The wafers were treated with boiling piranha solution (3:1 = sulfuric acid: DI water) for an hour followed by an organic solvent clean, then rinsed with copious DI water. Thin films of Ti (50 nm) and Ag (1.5 μm) were deposited using e-beam evaporation. The silver film was lithographically patterned into electrodes using Shipley 1827 photoresist (Figure 2.1 (a)). Wet etching was carried out using a silver etchant made of 1:1 mixture of nitric acid and DI water followed by Ti etching. The patterned silver electrodes were chlorinated chemically by dropping 50 μl of

0.1 M $FeCl_3$ solutions onto the electrode area, situated within the inner electrolyte chamber, for 40 seconds at room temperature to create Ag/AgCl electrodes (Figure 2.1 (b)). Three layers of silicone rubber (PDMS) were prepared separately by soft lithography. The first layer has a microfluidic channel (400 μm x 50 μm) to contain the 10 mM TPP^+ inner filling solution needed for the ion selective sensing. These microfluidic channels were produced by soft lithography with a thick negative photo resist (SU-8) mold to keep the volume of the inner filling solution constant compared to the hand-cut L-shaped reservoirs from our previous reported sensor (Figure 2.1 (c)). A 2 mm hole was drilled through the center of the microfluidic channel to provide an interface between the inner filling solution and the medium in the sensing chamber through the ion selective membrane. The TPP^+ ion selective (IS) membrane solution was prepared with a mixture of 4.4 mL of tetrahydrofuran (THF) and dioctyl phthalate, 0.15 g of polyvinyl chloride (PVC), and 6 mg of precipitation of tetraphenylboron (Na^+TBP^-),[37] and transferred onto a PDMS layer by a new transfer technique (described below). To streamline the fabrication process, we utilized a commercial, leakage-free Ag/AgCl reference electrode (Warner Instruments) and fabricated only the working electrode with the IS membrane.

In order to create reproducible membranes and ensure their secure, wrinkle-free bonding with the underlying PDMS layer, we developed a transfer method in which the IS membranes are first prepared and cured on a separate PMDS scaffold before being positioned and deposited on the chip.

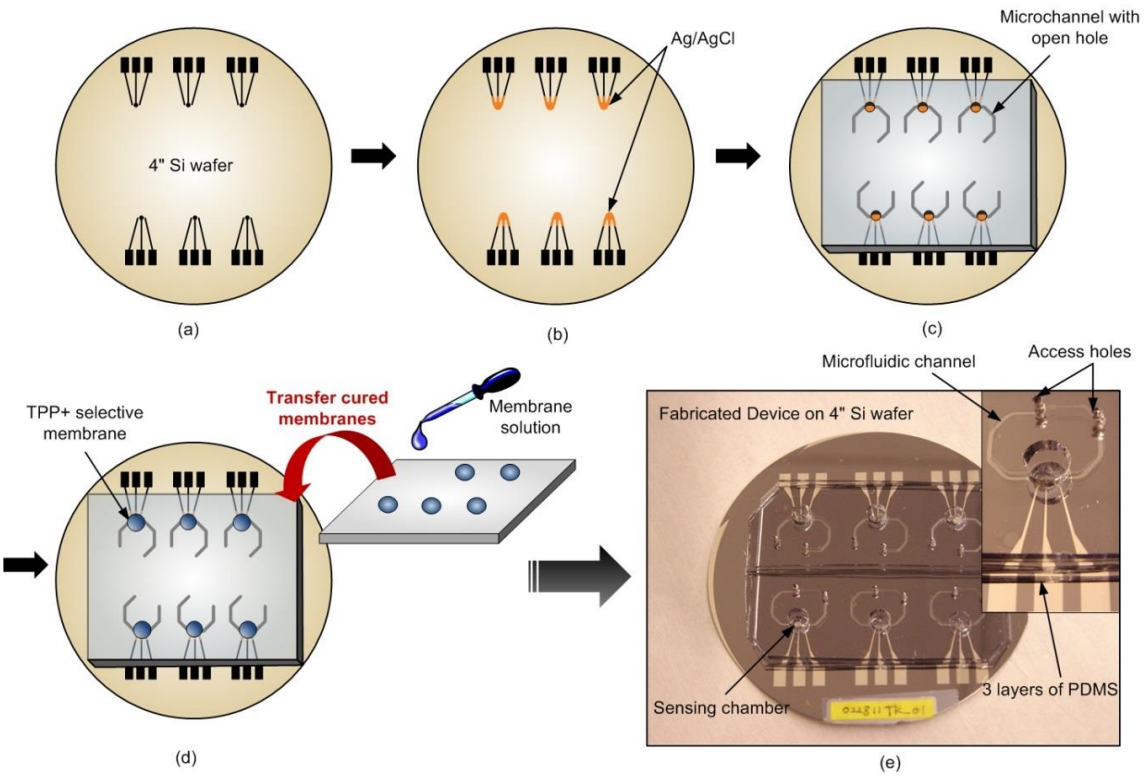

Figure 2.1. Schematic diagrams of microfabrication steps and the fabricated device. (a) Silver thick film deposition and patterning into electrode arrays on a 4" Si wafer. (b) Chlorination of silver to make Ag/AgCl on the sensing areas. (c) Assembly of the 1st PDM

As depicted in Figure.2.1 (d), a clean 2 mm thick PDMS scaffold was first aligned atop the first PDMS layer, such that the open 2 mm center holes of six microfluidic channels are visible from above. 30 µL of freshly prepared ion selective membrane solution was then carefully dropped onto the scaffold to correspond to the position of the channel holes underneath. These were allowed to cure overnight at room temperature. The following day, the scaffold was flipped over, carefully positioned so the cured IS membranes fell within the chamber holes, and gently pressed out for 5-10 minutes. This resulted in intact IS membranes that were completely and accurately transferred into position without wrinkles. We also tried this transfer method at elevated temperature (~ 60° C) in a hot oven, assuming that the membrane would be more pliable and allow for easier transfer. Although the transfer

was successful, we found that the high-temperature treated membranes did not exhibit proper responses to changes in [TPP^+]. We believe this is because the sensitivity of the IS membrane is a non-linear function of temperature (data not shown). The remaining two PDMS layers were aligned and assembled together manually under a stereomicroscope. The bottom microfluidic channel was filled with 10 mM TPP^+ through the access holes using a micropipette. The completed mitochondrial lab-on-a-chip device in Figure 2.1 (e) shows an array of 6 fully manufactured sensors, with three layers of PDMS constructed on a 4" silicon wafer. The inset reveals the components of the chip including the bottom microfluidic channel with its access holes and the open 80 µL circular sensing chamber.

To summarize, the advantages of this second generation technology over the first generation include 1) A Si 4" wafer process (rather than microscope slides), 2) Lithographically defined PDMS microfluidic channels (as opposed to hand cut), 3) Batch compatible, transfer process for membrane assembly (rather than manual membrane glue in place), and 4) A batch, completely automatable, parallel manufacturing process that can be scaled up to multiple devices per wafer) as opposed to manual, serial assembly of each device component by component. We now turn to the performance of the improved devices.

Results and Discussion

Characterization

The experimental set-up for the sensor calibration and measurement is shown in Figure 2. 2. One of the patterned working electrodes (Ag/AgCl) was connected to a digital multimeter (Agilent 34401A, input impedance setting = 10 GΩ) along with a commercial leakage-free Ag/AgCl reference electrode (Warner Instruments). A computer installed with LabView was

linked to the digital multimeter for data acquisition *via* a GPIB interface (National Instrument, GPIB-USB-HS). The acquired data was analyzed and plotted using Igor Pro (WaveMetrics).

The sensor was primed for use by filling the sensing chamber and underlying microfluidic chamber with 10 mM TPP^+ solution overnight to activate the TPP^+ IS membrane. The next day, the inner filling solution was replaced with care taken to prevent bubble formation which could create an open circuit against the IS membrane and signal-reading errors. The sensing chamber was rinsed with DI water and respiration buffer 3 times before filling with fresh respiration buffer. The sensor was extensively characterized using a 5-point calibration curve with TPP^+ concentrations ranging from 0.3 µM to 600 µM. The potential difference between the reference and working electrodes was monitored while incrementally increasing the TPP^+ concentrations within the sensing chamber.

Figure 2.2 (c) shows two calibration curves measured before and after a typical mitochondrial measurement (see below) and demonstrate the sensors reproducibility, durability, and small drift between experiments. The insert plot shows the signal stabilizing just a few seconds following each successive addition of TPP^+ (arrows) which marks a 60 % faster response time compared with our original sensor without its tapering large signal spikes. TPP^+ concentrations were plotted logarithmically to reveal the linear relationship between concentrations and IS electrode (ISE) potential (mV) as predicted by the Nernst equation. Since our experimental concentration range is between 5 and 10 µM, we typically perform a 2-point curve fit between our 2^{nd} and 3^{rd} calibration points (3 µM and 30 µM respectively). These measurements of ISE potential were used to determine sensor variation using the following equation:

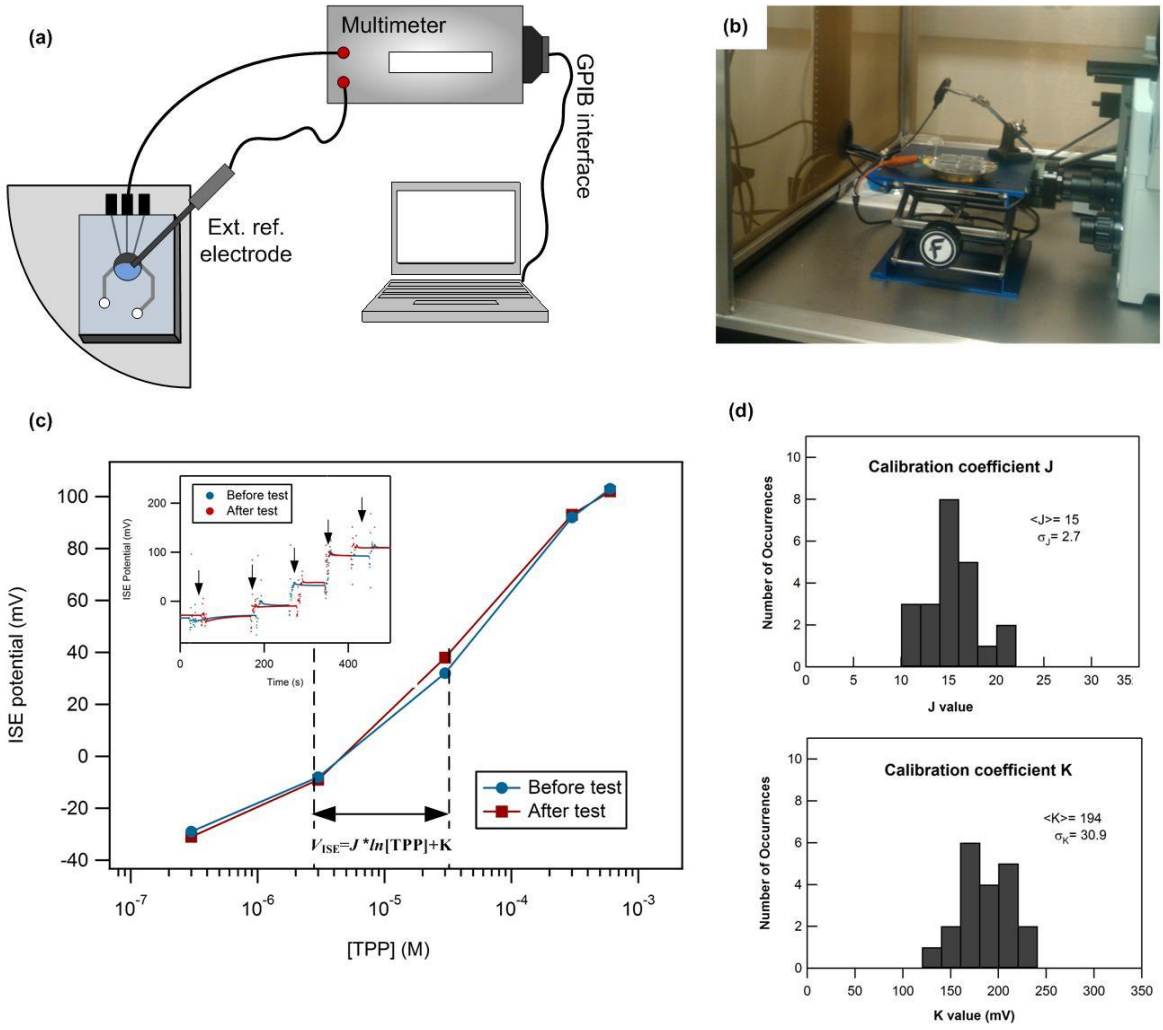

Figure 2.2.(a) Schematic of experimental set-up showing the sensing chamber, the sensor connected to the external reference electrode, and one of the electrode pads connected to a multimeter which is linked to a computer installed with Lab View for data acquisition. (b) Photograph of set-up. (c) 5-point calibration curves performed before/after mitochondrial assays showing reproducibility of the sensor. The slope of the highlighted area was used for data conversion (Inset: time trace of ISE potential response during the calibration, arrows showing additions of TPP^+.) (d) Statistical variation of J and K values from 21 separate calibrations from 8 separate devices.

$$(V_{ISE} = J * ln[TPP^+] + \mathrm{K}), \qquad \text{(Equation 2.2)}$$

where V_{ISE} is the measured ISE potential, and J and K are the two calibration coefficients.

An important issue is the statistical variation among sensors, which we now address. Figure 2.2 (d) illustrates the statistical data from 21 separate calibration curves performed on eight different devices. The J and K coefficients of variation represent the ratio of the standard deviations to the averages which, in our hands, resulted in values of ≈18% and ≈16%, respectively. This includes the effects of *both* device-to-device variations, as well as variations from run-to-run within one device. This narrow data distribution indicates good reproducibility of the sensor response and a small device-to-device variation. This is an improvement over the previous devices designed in Burke lab where the slope and offset from both sources of error (device-to-device and run-to-run) varied by a much larger amount, specifically ≈25% and ≈82% for J and K equivalent, respectively, and indicates the significance of developing a wafer scale manufacturing process. While excellent, this variation in calibration coefficients may still require a careful calibration before each measurement for some envisioned assays that require high accuracy, an issue we hope to address in future generations of our chips.

Mitochondrial membrane potential measurement

As a demonstration with known cell lines, a mitochondrial membrane potential assay was performed in respiration buffer at room temperature using isolated mitochondria prepared from human cell lines, including Heb7A and 143B TK-, and also from mouse liver (Isolation protocols given in the Appendix I). During the measurement, the isolated mitochondria were maintained on ice to prevent degradation. For each individual sample, the TPP^+ concentration traces were monitored before and after the addition of mitochondria to establish a basal "resting" potential. Then, changes in the mitochondrial membrane potential

were recorded as OXPHOS complex I substrates (pyruvate and malate) and ADP were added to the sensor chamber.

The [TPP^+] measurements were converted to membrane potential and compared according to the following equation:

$$\Delta\Psi_m = \frac{RT}{F}\ln\frac{V_0[TPP^+]_0/[TPP^-]_t - V_t - K_0P}{V_mP + K_iP}, \qquad \text{(Equation 2.3)}$$

where $[TPP^+]_o$ and $[TPP^+]_t$ represent TPP^+ concentration in the test chamber before the addition of mitochondria and at time t respectively. V_o is the initial buffer volume in the chamber and V_t represents the final volume in the chamber which includes the total mass (in mg) of mitochondrial protein (P) added in the assay. For our purposes, the mitochondrial matrix volume (V_m) was assumed to be equal to 1 µL/mg protein. The partition coefficients describe the innate binding and accumulation of the TPP^+ ion to the matrix (K_i) and external (K_o) faces of the inner membrane and are given values of 7.9 µL/mg and 14.3 µL/mg, respectively.[38] For our purposes, we used the values V_0 =70.5 µL; V_t= 75.5 µL and used 750 ng of isolated mitochondrial protein per assay (P).

In order to allow for improved quantitative measurements of the membrane potential of various cell lines, we developed a procedure in which all of the initial starting concentrations and volume of solution and mitochondria were the same from experiment to experiment, the only variable being the cell line that produced the mitochondria. We chose an initial concentration of 7.2 µM for all the experiments, allowing for the same initial starting point (prior to the introduction of mitochondria) for all experiments. Using this technique, the initial value of TPP^+ was always known, and only changes in TPP^+ were needed. Thus, for

the calibration, only the logarithmic slope of the TPP^+ vs. V_{ISE} curve was important. In an experiment where the TPP^+ vs V_{ISE} curve was measured immediately before and immediately after the experiment, the values of J changed by ~ 15% (20.8 vs. 17.5 mV for J). In our experiments, we used only the logarithmic slope (J^{-1}) to determine the value of TPP^+ after introduction of the mitochondria. More on the error analysis will be presented below.

A representative result from a mitochondrial membrane potential experiment is shown in Figure 2.3 with [TPP^+] values obtained from the calibration curve conversion. After adjusting the chamber working concentration of TPP^+ to 7.2 μM, 5 μL of 150 ng/μL freshly isolated mitochondria were introduced into the 80 μL sensing chamber. Our experimental working concentration, 10 ng/μL, is three orders of magnitude less than is needed by conventional assays.[37,39] The chamber solutions were mixed gently three times using a micropipette and the trace was allowed to stabilize and remain constant showing that the solution is thoroughly mixed and no further diffusion occurred due to the incomplete mixing during the measurement (data not shown). Upon introduction of mitochondria, mitochondria quickly absorbed TPP^+ according to their $\Delta\Psi_m$ leading to decrease in [TPP^+] in the sensing chamber.

In our experiments, the addition of 5 μL of solution containing mitochondria would lower the TPP^+ concentration (even in the absence of mitochondria) by about 0.5 μM. Because of the membrane potential, there is an additional reduction in [TPP^+] due to uptake by the mitochondria. In Figure 2.4, we plot the relationship of the inferred membrane potential to the measured [TPP^+] concentration change due to the mitochondria $\Delta\Psi_m$.

To test functional activities of complex I by adding the OXPHOS substrates, pyruvate and malate (P/M) were added, to stimulate the active shuttling of protons out of the

mitochondrial matrix. This resulted in an increase in the magnitude of $\Delta\Psi_m$, thus diffusion of TPP^+ into the matrix, resulting in a decrease in $[TPP^+]$ in the medium. Indeed, the response to P/M was instantaneous and stabilized to reveal a drastically decreased $[TPP^+]$ by 1.5 μM in the sensing chamber. Once these data were collected, we wanted to ensure the viability of our mitochondria to validate that the TPP^+ efflux is active and not merely due to defunct OXPHOS machinery, degraded membranes, etc. To that end, we added ADP to take advantage of the fact that OXPHOS complex V (ATP synthase) utilizes the $\Delta\Psi_m$ to convert ADP to ATP. Accordingly, we detected the increase of TPP^+ ions in the chamber, indicating a partial depolarization of the $\Delta\Psi_m$ which was used to drive ATP synthesis. Due to the physical effect of manual injections using a micropipette, signal noise was recorded as scattered data when injections were performed. This could be eliminated by employing an automated fluidic perfusion system in future designs.

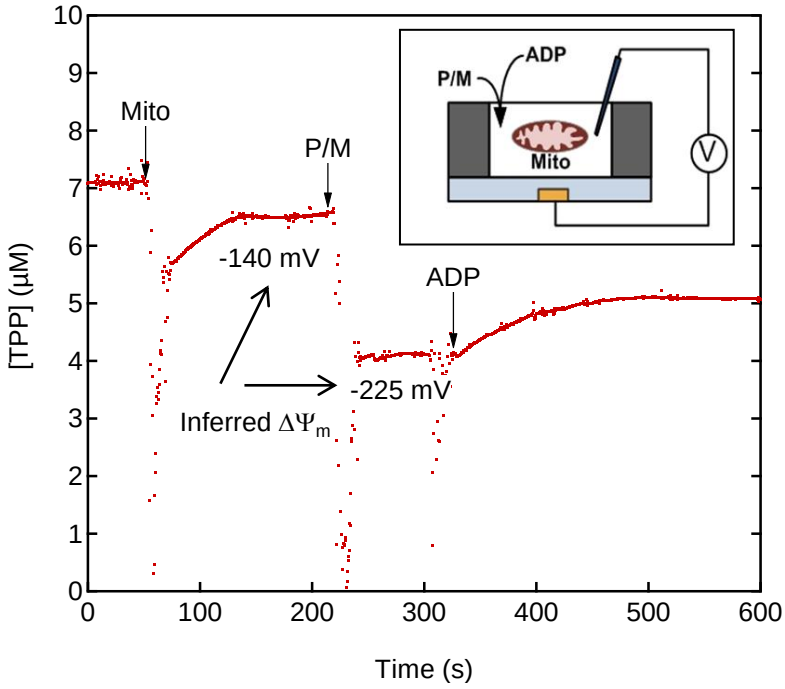

Figure 2.3. Measurement of [TPP+] with isolated mitochondria from 143B TK- osteosarcoma cells. Vertical arrows indicate successive addition of 5 μL of 150 ng/μL isolated mitochondria, 10 μL of 1 M pyruvate/0.5 M Malate and 1μL of 10 mM ADP. See text for discussion.

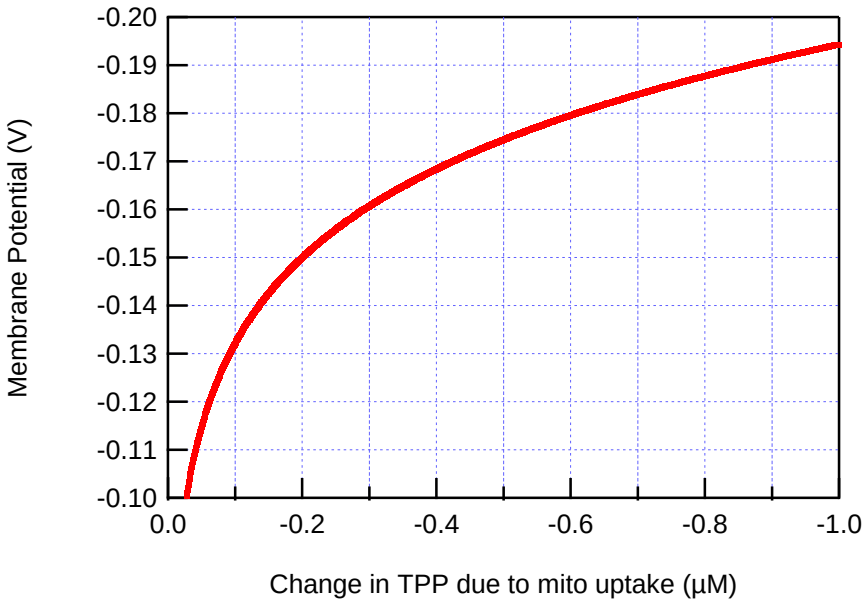

Figure 2.4. Conversion of measured [TPP+] into ΔΨm.

The same series of measurements with mitochondria from Heb7A and mouse muscle cell lines were performed and compared. The amount of mitochondria and chemicals as well as the sequence of injections remained the same to avoid variations from assay to assay. Drops of [TPP^+] after addition of mitochondria, and the corresponding $\Delta\Psi_m$ values are plotted in Figure 2.5 which were obtained from 6 different assays. As expected from prior studies of mitochondrial bioenergetics, $\Delta\Psi_m$ of mitochondria from mouse skeletal muscle showed the largest value among other cell lines indicating the vibrant activity of the skeletal muscle tissue. (Run to run variations are attributed to sensor drift, to be discussed below in further detail.) The membrane potential of Heb7A was slightly higher than that of 143b. Overall the results of the mitochondrial assays were consistent with the results of prior studies.[40]

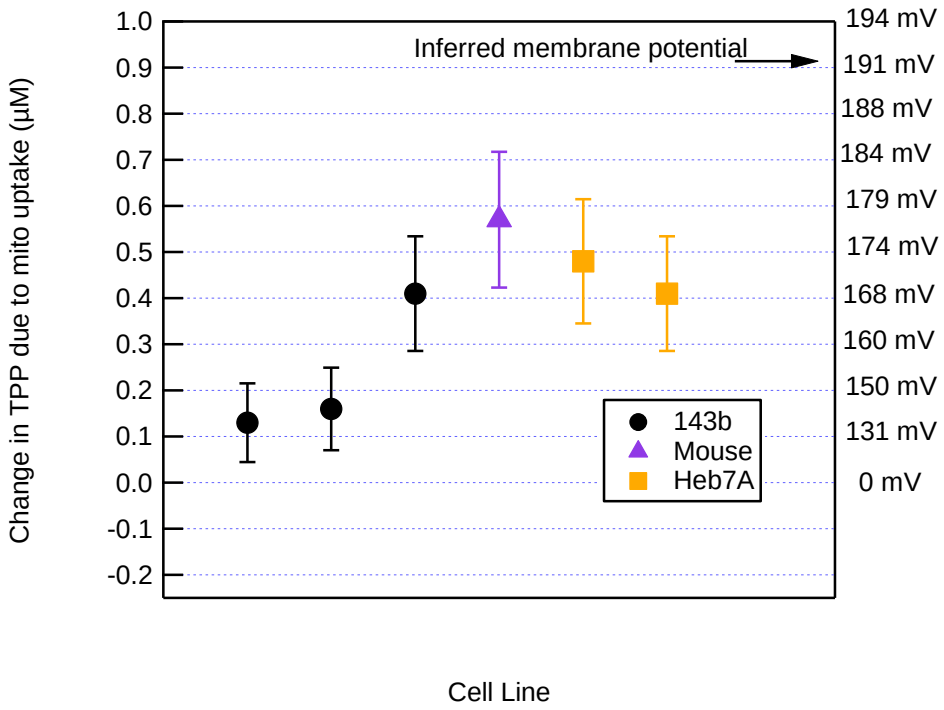

Figure 2.5. Data comparisons of drops in [TPP+] due to mitochondrial uptake measured right after addition of mitochondria. Right axis shows calculated ΔΨm of isolated mitochondria. Data are from three different cell lines (143b, mouse muscle, Heb7A). Error bars are due to calibration uncertainty of the ISE electrode potential to [TPP^+].

We now turn to a detailed error analysis of our procedure. In our experiments, the statistical variation (as a function of time) when the sensor was stable was quite low. For example, the standard deviation of the measured ISE potential for the time trace shown in Figure 2.3 in the stable region between t~500 s and t~600 s is only 50 µV. In this experiment, for this trace, this corresponds to a standard deviation of 0.02 µM in the value of [TPP^+]. The inferred value of $\Delta\Psi_m$ has a standard deviation of only 0.5 mV. Each point was integrated for ~ 1 second. (For a 10 ms integration time, this would correspond to a 5 mV standard deviation on the inferred membrane potential.) In addition to rapid, random fluctuations due to statistical variations, we also observed permanent, progressive changes in the measured [TPP^+] values, which we attribute to the actual biochemistry of the mitochondria which respond on a much longer time scale compared to the measurement time per point of one

second. Since we do not typically observe these long term drifts during calibration without mitochondria (see e.g. the inset of Figure. 2 2 (c)) we believe the time dependent behavior we observe is not due to the sensor technology itself. Indeed, this demonstrates the ability of our technology to assay kinetic as well as equilibrium bioenergetics.

Drift of the calibration during the measurement is more significant, and we address this issue now. In principle, the histograms of Figure 2.2 provide a complete quantification of this drift between calibrations and devices. As discussed earlier, it is possible to improve on this error by performing calibrations just before and after the experiment, and using identical conditions in order to compare the behavior between devices. As discussed above, the initial value of $[TPP^+]$ is known accurately, so that the small changes from this initial value can be determined only from small changes in the measured sensor voltage and the (logarithmic) slope (J^{-1}) of the calibration curve, the offset being less important because only small changes about the known, initial value are considered. For the example experiment in Figure 2.3, the introduction of mitochondria into the chamber changed the value of $[TPP^+]$ by, at most, 1 μM. Since the initial value is known with low error, and the (logarithmic) slope is determined with a drift of less than 15% during the measurement (worst case, see above), the value of the *change* in the value of $[TPP^+]$ is known to within at worst ~ 0.1 μM. The error bar due to the uncertainty in the slope J is the dominant error, and indicated in Figure 2.5. (Note that due to the non-linear relationship between the measured ISE potential and the inferred value of $[TPP^+]$, the error in $[TPP^+]$ gets approximately linearly worse as the *change* in $[TPP^+]$ increases from 0 to 1 μM. We have determined numerically that the error is at most ± 0.12 μM error for a 1 μM drop in $[TPP^+]$ on introduction of mitochondria, and less for smaller drops in $[TPP^+]$, by calculating $[TPP^+]$ for different values of J^{-1} and determining the worst

case error at each value of inferred TPP^+ drop.) In order to relate the calibration drift component of this [TPP^+] error to an error in the inferred value of $\Delta\Psi_m$, we use equation 2.2. As can be seen in Figure 2.4, this conversion is non-linear, so the error conversion will depend on the specific parameters of the experiment. In our case, this still allows an error smaller than $\sim \pm 10$ mV for the determination of high values of $\Delta\Psi_m$. This error increases as the values of $\Delta\Psi_m$ decreases from 180 mV. These parameters will continue to allow studies on the relative value of $\Delta\Psi_m$ between different cell lines. This can thus be a powerful tool for the accurate investigation of mitochondrial membrane potential from a variety of cell lines where sample size is limited, such as clinical biopsies or embryonic stem cells.

The sensors developed here remained completely functional for longer than three months and exhibited reproducible responses for over 40 assessments without replacing the TPP^+ ion selective membrane or Ag/AgCl electrodes. For further improvement on sensor performance and the stability, there are three possible avenues. First, a temperature controller to control medium temperature would enable improved stability of the calibration curve and also bioenergetics studies, which are important to carry out at a known (rather than ambient) temperature. Second, an on-chip stirrer could be integrated into the chamber for continuous mixing during the assay. Lastly, a sensor equipped with an automated sample perfusion system with an encapsulated sensing chamber would provide better stability and measurements compared to a manual sample injection by a micropipette.

Conclusions

A wafer-scale fabrication process for a TPP^+ ion selective microsensor for mitochondrial membrane potential assays has been developed and demonstrated. The newly designed

process includes the new membrane transfer method which is compatible with microelectronic fabrication techniques resulting in high yield and high throughput process by integrating 6 devices into a single wafer. Further improvement is possible with more effort to increase the number of devices on a single wafer. Due to the improved bonding condition between the TPP^+ ion selective membrane and the bottom PDMS layer, the devices showed structural stability and robustness over an extended period of time (> 3 months) with nominally identical sensitivity to changes in $[TPP^+]$. Due to the system design, in the future it is feasible to run several assays in parallel at the same time for high throughput studies. This will allow a cost-effective method to mass-produce miniaturized mitochondrial assay chips, which are candidates to replace the current costly systems installed with large, traditional sensing chambers. For these reasons, our system can find various applications in the emerging field of mitochondrial bioenergetics.

Acknowledgements

This work was supported in part by the following grants awarded to D.C.W.: NIH-AG24373, NS21328, AG13154, DK73691, CIRM Comprehensive Grant RC1-00353, and a Doris Duke Clinical Interface Grant 2005057. P.B. acknowledges support of this work from NIH National Cancer Institute Grant 1R21CA143351-01, as well as support from the ARO (MURI W911NF-11-1-0024).

This chapter is a reprint of the material as it appears in (Lim, T.-S., Davila, A., Zand, K., Wallace, D. C., & Burke, P. J. (2012). Wafer-scale mitochondrial membrane potential assays. *Lab on a Chip, 12*(15), 2719–2725. doi:10.1039/c2lc40086c). The co-authors listed in this publication directed and supervised research which forms the basis for this chapter.

CHAPTER 3 : Nanofluidic Platform for Single Mitochondria Analysis Using Fluorescence Microscopy

Introduction

Mitochondria play a multitude of roles in cell life. For example, they generate most of the ATP needed for cellular processes, modulate the concentration of cytoplasmic and mitochondrial matrix calcium, produce and regulate reactive oxygen species, and control intrinsic apoptosis or programmed cell death. Consequently, mitochondrial dysfunctions can significantly affect the body homeostasis. In fact, there is a growing body of evidence that suggest the link between mitochondrial dysfunctions and pathological conditions such as degenerative disease, diabetes, cancer and aging.[13,41]

Advances in live imaging techniques have uncovered large morphological, functional and behavioral heterogeneity within mitochondrial populations, not just between mitochondria of different cells but also between mitochondria in a single cell.[42,43] Studying this heterogeneity can reveal further understanding of mitochondrial functions. However, so far studies on heterogeneity of single mitochondria have not resulted in very conclusive results. Part of this might be attributed to the technical difficulties of imaging individual mitochondria; mitochondria moving out of plane of focus, background fluorescence, not enough control on the chemical environment surrounding each individual mitochondrion, *etc.* This shows the need for development of innovative, advanced technologies appropriate for single mitochondrion studies.

The advent of microfluidics and nanofluidics can address the shortcomings of traditional approaches in studying isolated mitochondria. The ability to control fluids in small volumes enables assays requiring significantly less sample size, and the precise and controlled delivery of chemicals makes it ideal for testing specific hypotheses involving different processes.

Recently we miniaturized a classic assay of mitochondrial membrane potential requiring only 1000 cells.[19,44] However, even though this is a four order of magnitude improvement, it did not get us down to the single mitochondrial or even single cell level. Extensive research this decade has been carried out to assay and analyze individual cells using flow cytometry and microfluidic devices.[20] This has given rise to extraordinary technological capabilities, such as the possibility of finding one circulating tumor cell per 10^9 healthy cells in whole blood for cancer diagnosis.[21] In contrast, the field of analysis of individual sub-cellular organelles is in its infancy. Here we demonstrate a first step in this direction, developing a novel platform to trap single mitochondria inside a nanochannel where they can be subjected to different chemical environments and interrogated *via* a variety of fluorescent dyes. We demonstrate that single isolated mitochondria remain vital and functional in this trapped state.

Experimental Section

Fabrication process

Silicon wafer with photoresist patterns is used as the mold for soft lithography of PDMS. To fabricate the mold, silicon wafer was cleaned with 120° C Piranha solution (3:1 mixture of sulfuric acid and hydrogen peroxide) for 1 hour, rinsed in DI water, dried with nitrogen and dehydrated at 200° C. Wafer was primed with hexamethyldisilazane (HMDS). Channel patterns were fabricated by photolithography of Microposit SC1827 positive photoresist. Photoresist was spin coated on the wafer at 3500 rpm for 30 seconds, prebaked at 90° C for 30 minutes in a convection oven and exposed to G-Line UV light through a chromium(105 nm)/glass mask using Karl Suss MA6 mask aligner with soft contact between the mask and

the wafer. The dosage of exposure was set at 160 mJ/cm^2. Microposit MF-319 was used for developing. The developing takes around 25 seconds.

We use soft contact for lithography; the contact between the mask and the resist surface is not very close and there is a slight gap between the two surfaces (compared to vacuum contact). Due to diffraction of light passing through the mask, light that reaches the plane of the wafer does not have a step function intensity distribution; regions of the photoresist near the pattern edges get some light exposure even though they are covered by opaque parts of the mask. This is a well-known phenomenon in positive photoresist lithography that usually leads to trapezoidal cross section of the developed photoresist instead of a rectangular cross section. It can be avoided or reduced by using vacuum contact between the mask and the resist surface, lowering the dosage of exposure and using a photoresist with higher contrast. Here, we are using this phenomenon to get multiple heights with a single lithography step. Due to small width of the channel, the whole width of the channel receives some dosage of exposure; for each channel the edges get more exposure while the light intensity decreases gradually as it gets closer to the center of the channel. The resist regions that receive a higher exposure dissolve faster in the developer. When the wafer is placed in the developer solution, the regions that are exposed through the transparent parts of the mask have the fastest dissolution rate, while the resist at the trap channel region gets dissolved at a slower rate, with the lowest rate at the center (vertical axis of symmetry). Therefore the trap channels loose some of their height. In case of the larger features (access channels), the edges get some light exposure but the mask protects the bulk of the feature from light exposure, therefore larger features keep their original height after the development step. This method is very reproducible and out of the 10 molds that we fabricated, we could get these

multiple height patterns on 7 of them. Using the given lithography parameters the height of the nanochannels ranged from 450nm to750nm.

Silicone elastomer and curing agent (Sylgard® 184, Dow Corning Co.) were mixed thoroughly at a 10:1 weight ratio. PDMS was degassed for 30 minutes in a vacuum desiccator and poured over salinized mold to a thickness of 3 mm. The mold was placed in a 70° C curing oven overnight. After curing, PDMS was easily cut and peeled off from the mold. Inlet and outlet holes were punched with a diameter of 0.63 mm to allow connection to the syringe pump. To seal the channels the chips were exposed to 70 W oxygen plasma treatment at 100 mTorr for 20 seconds, immediately placed on piranha cleaned glass slides and left in 70° C oven for 20 minutes to complete the bonding process. The Oxygen plasma treatment causes the PDMS to become hydrophilic, making it easy to introduce the aqueous solution into the channels after bonding. However, after about a day the sidewalls would become hydrophobic again and the channels were not re-usable.

Fluidic channels were filled with the respiration buffer without mitochondria first and the buffer containing mitochondria was flown into the channels later.

Mitochondria Isolation and sample preparation

Mitochondria were isolated from the human cervical cancer cell line HeLa (ATCC, CCL-2). The adherent cells were cultured and maintained in log growth phase in media consisting of EMEM (ATCC, 30-2003) supplemented with 10% FBS (Invitrogen, 10438-018) and 1% Penicillin-Streptomycin (ATCC, 30-2300). All other chemicals were obtained from Sigma Aldrich, unless otherwise noted. The mitochondrial isolation protocol was adapted from[44]. Details of the isolation protocol are discussed in Appendix I.

Imaging

Mitochondria were imaged with Olympus IX71 inverted fluorescence microscope, equipped with a 12 bit monochromatic CCD camera (QIClick-F-M-12), a 60x, 0.7 NA objective, 120 W Mercury vapor excitation light source and standard FITC (490 nm-525 nm) and TRITC (557 nm-576 nm) filters. Image analysis was done with ImageJ software. 3x3 median filter was used to remove noise. Images in this paper are false-colored red or green, depending on the filter set used, for clarity. For fluorescence intensity measurements we manually selected the area with the highest intensity at the center of each mitochondrion image and averaged the fluorescence intensity over the selected area. Background fluorescence was removed by choosing 3 neighbor regions with the same area selected for the mitochondria. The fluorescence intensity was averaged over the three regions and subtracted from the mitochondrial intensity. The standard deviation in the background fluorescent intensity causes some small error (less than 10% in most cases) in calculating the fluorescence intensity. This error has been taken into account for the ratio calculations. The resolution of the imaging system and the apparent *versus* real size of the mitochondria is discussed here briefly.

The resolution of our fluorescence imaging system is 0.50 μm for 525 nm wavelength and 0.45 μm for 575 nm wavelength (based on Rayleigh criterion).[45] If two particles are closer than 0.5 μm, they will appear as one larger particle. Also objects that are smaller than our resolution limit are still detectable but will appear as diffraction disks with a diameter of around 0.5 μm regardless of their actual size and shape. The intensity at the central diffraction spot is proportional to the total energy emitted by the particle that reaches the aperture,[46] so we can still measure the intensity from mitochondria that are smaller than 0.5μm even though we cannot resolve the size of the particle. In general the contrast and

brightness of the fluorescence images in the figures are adjusted to make the mitochondria easier to spot on the figures, this affects their apparent size.

Fluorescence Dyes

Mito Tracker green (MTG), obtained from life technologies, is a mitochondrial selective fluorescent probe that binds to mitochondria proteins regardless of the membrane potential of the mitochondria[47] and emits a bright green fluorescence at 519 nm when excited at 490 nm. Mitotracker Green forms a dye-protein complex with free thiol groups inside the mitochondria, yielding significantly higher fluorescence than free dye in aqueous solution. It is reported that this increase could be as much as 40 fold.[48] We used MTG to visualize the mitochondria in the channels. To stain the mitochondria, we diluted the dye in Dimethyl Sulfoxide (DMSO) to a concentration of 100 μM and then diluted it 1000 fold in the respiration buffer to a concentration of 100 nM.

To monitor the membrane potential of the trapped mitochondria, we used 5,5′,6,6′-tetrachloro-1,1′,3,3′-tetraethylbenzimidazolyl-carbocyanine iodide (JC-1) obtained from Sigma Aldrich. In energized mitochondria the membrane potential promotes an uptake of JC-1 into the mitochondrial matrix according to the Nernst equation. The high concentration of JC-1 forms aggregates inside the mitochondria. When JC-1 is excited at 488 nm it emits with peaks at 530 nm (green) and 590 nm (red). The intensity of the red emission strongly depends on the concentration of J-aggregates and therefore on the membrane potential of the mitochondria. Energized mitochondria emit a bright red fluorescence at 590 nm. In mitochondria with low membrane potential the dye does not form aggregates inside the mitochondria and the red fluorescence decreases. It has been shown that there is a significant

correlation between the ratio of red to green fluorescence of this dye and the membrane potential of mitochondria.[49,50]

We also used Tetramethylrhodamine Methyl Ester (TMRM) purchased from life technologies in some experiments. TMRM is a lipophilic cationic dye with red-orange fluorescence that is accumulated by mitochondria according to the Nernst equation. The fluorescence intensity of the stained mitochondria can be used to estimate the mitochondrial membrane potential. By monitoring the time-dependence of the fluorescence of the inner mitochondrial membrane, one can obtain qualitative information about the dynamics of the membrane potential. It was observed that TMRM sticks to the PDMS channel and produces a high background fluorescence which makes it difficult to distinguish the mitochondria from background.

For JC-1 assays, JC-1 was dissolved in DMSO and then added to the mitochondria sample to a final dye concentration of 300 nM. The solution was mixed and incubated at room temperature for 7 minutes. TMRM was added with the same method. We tried various concentrations of TMRM from 100 nM to 2 nM.

Results and Discussion

Mitochondria Trap Devices

The goal of this project was to design a nanochannel device with dimensions small enough to trap individual mitochondria as a demonstration platform for manipulation and interrogation under controlled conditions at the single mitochondrial level. Mitochondrial morphology is varied, both *in vivo* and *in vitro*. A typical morphology is a cigar shape of width from 200 nm to 1 μm.[51] For this, standard photolithographically defined PDMS

channels have not yet been pushed to the submicron scale,[52] while nanochannel technology based on etching[53] is too small to pass single mitochondria.

The mitochondria trapping device is a nanochannel array, with two access channels and two access holes for fluid inlet/outlet as shown in Figure 3.1. The nanochannels have a trapezoid cross-section that is 3.5 μm at base and gradually narrows down to around 400 nm. The average width of the channels (the width at middle of the trapezoid) is around 2 μm which is larger than the diameter of mitochondria (0.2-1.2 μm) [51] and the height of the nanochannels at its highest point (0.45-0.75 μm) is almost equal to the average diameter of the mitochondria (terminology nanochannel has been used to describe channels with dimensions smaller than 1μm.[54] These dimensions are measured from AFM images. The nanochannels are 500 μm long and are connected to two 100 μm wide, 2 μm high access channels. The device is fabricated using simple, economic and high throughput soft lithography of PDMS.

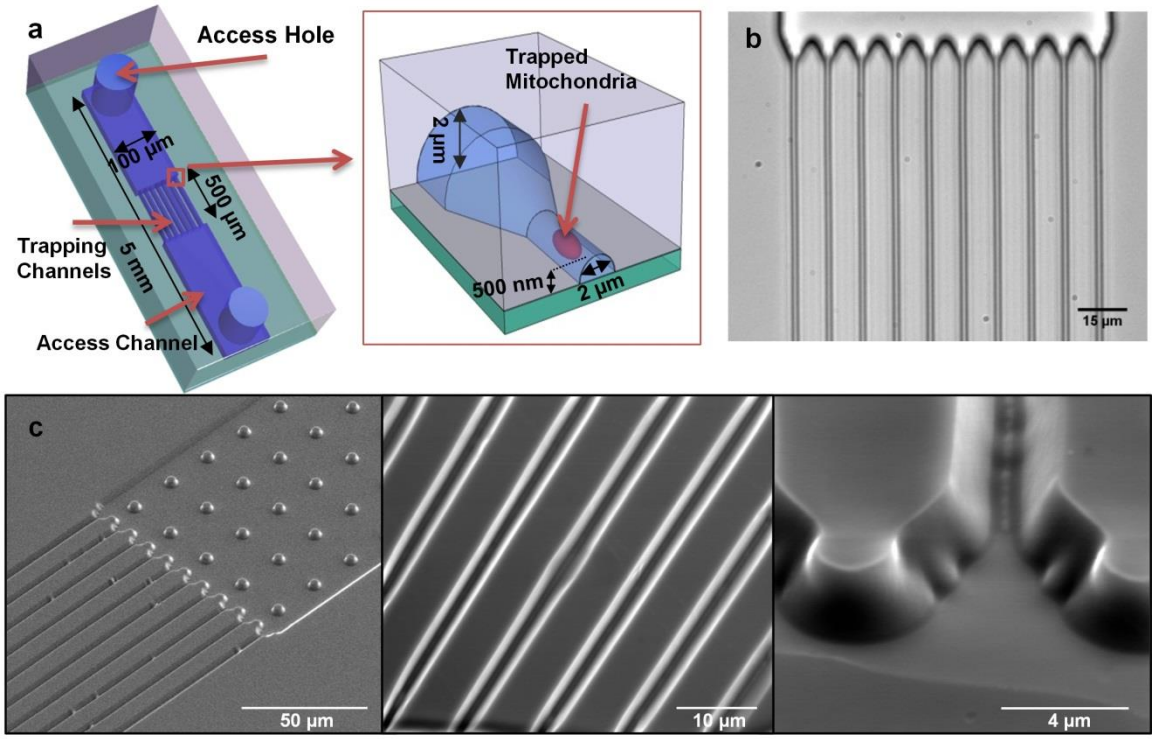

Figure 3.1. Geometry of the mitochondria trapping devices, a) Schematic of the device and trapping mechanism. b) Bright field microscope image of the device. c) SEM images of the channels in PDMS.

Immobilization of Mitochondria

Mitochondria solution is introduced into the channels with a syringe pump. Individual mitochondria start to get trapped in the nanochannels and their population gradually goes up as the flow continues. In Figure 3.2, an example trapping experimental run is shown. Mitochondria stained with MTG are flown into channels with a rate of 10 µL/hour. Time-lapse microscopy of the channels is performed at the same time. In all experiments where mitochondria were imaged, their position was fixed after the initial introduction. The chemical environment can be adjusted through additional fluid flow at rates of up to a few µL per minute. This is shown, for example, in Figure 3.2. Thus, the mitochondria are gently trapped inside the nanochannels, enabling access to fluid for them but they are not moving.

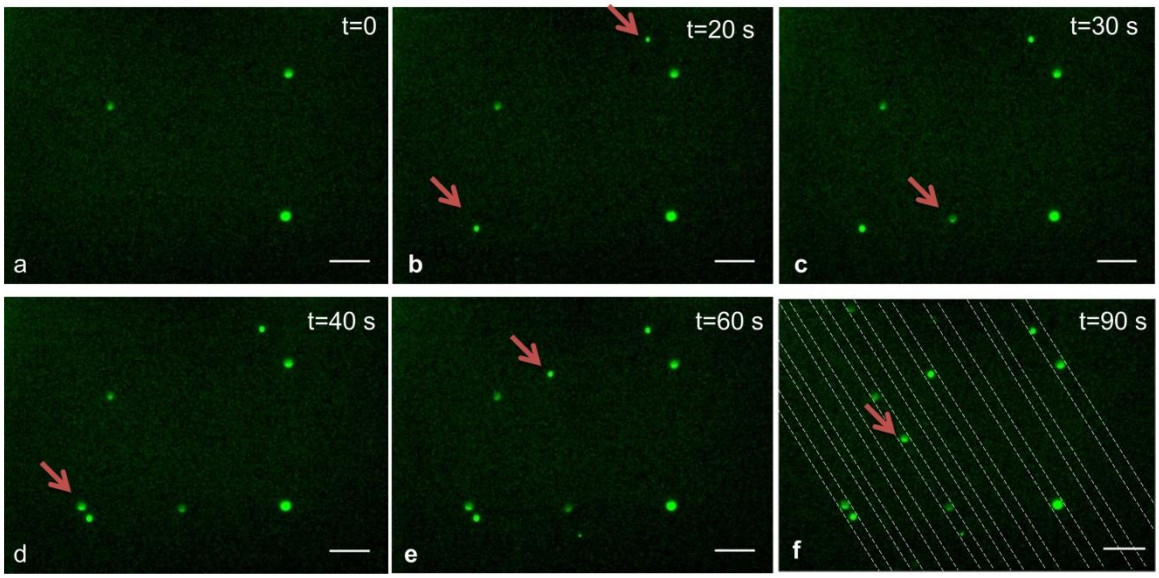

Figure 3.2. Series of time images of MTG labeled mitochondria. In each image, a new mitochondrion appears that has been flown in from the reservoir and trapped inside the nanochannel. Red arrows indicate the addition of new mitochondria. Dashed lines in panel f suggest the outline of the channels. Scale bar is 10 µm.

Trapping Mechanism

The trapping mechanism is not mitochondrial interactions with the channel sidewalls. This was shown by performing a similar experiment with larger channel sizes but otherwise nominally identical conditions. For the larger channels, the mitochondria do not stick to PDMS surfaces. It has been shown that oxidized PDMS has negative surface charge.[55] Thus, it is likely that an electrostatic repulsion between the mitochondria and the sidewalls prevents adhesion between the negatively charged mitochondrion and negatively charged channel surface.

The mitochondria are physically trapped along the channels (Figure 3.3). Since the height of the channel at the highest point is similar to the average diameter of mitochondria but the width is around two times larger, the channels act like a filter where fluid can pass through but individual mitochondria are trapped along the channels one by one. Due to variations in size of individual mitochondria and also the trapezoidal cross section of the channels,

occasionally we see that one mitochondrion is trapped in some location in the channel but a smaller mitochondrion can pass along the first mitochondrion and get trapped at a further location. Exact determination of trapping locations requires mathematical simulations, but based on our experimental observations we believe that mitochondria that are already trapped at the channel entrance due to the small height of the channel behave like obstacles that disrupt the flow in the narrow channel and create vertical components in the flow direction (vertical to the channel direction).

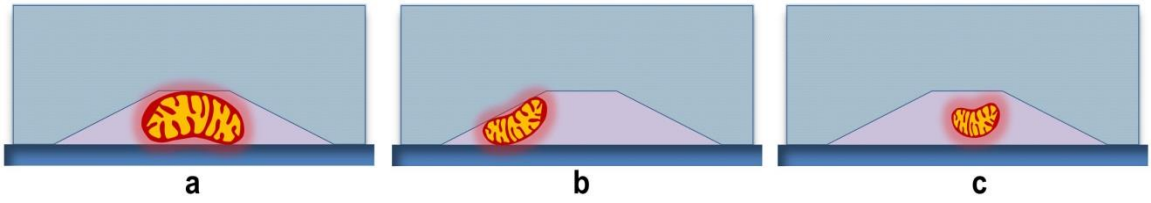

Figure 3.3. Cross section of the channels and trapping mechanism of mitochondria. a) Larger mitochondria get trapped at the middle of the channels. b) Smaller mitochondria get trapped at the corners, leaving room for other mitochondria to pass. c) Some small mitochondria will pass through the middle of the channel without getting trapped.

The flow direction, variations in mitochondria size and the trapezoidal cross section of the channel results in mitochondria getting trapped at random locations along the channel. We have found experimentally that for a flow rate of 10 µL/hour, the concentration of mitochondria in the flow buffer that results in an appropriate number of trapped mitochondria for our imaging setup is around 50 µg/mL of mitochondrial protein. The procedure to find this value is discussed in the following paragraph.

If the amount of mitochondria that reaches the channel entrance is too high, initially a few mitochondria are trapped in the channel, but additional mitochondria can block the entrance. It is important for imaging to use an optimized mitochondrial concentration. We tried different concentrations of mitochondrial protein from 300 µg/mL to 1 µg/mL while keeping

the flow rate constant at 10 µL/hour and the flow time at 2 minutes. With a mitochondrial protein density of around 300 µg/mL, concentration of trapped mitochondria was high and we could see clogs at the entrance to the channels and also inside the channels (Figure 3.4).

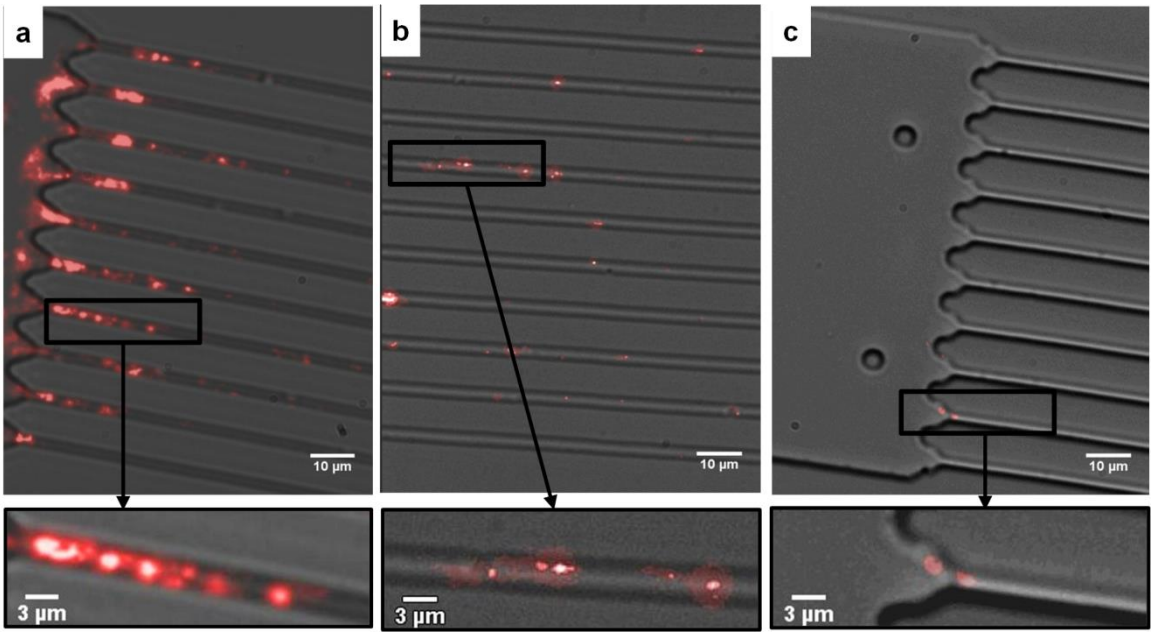

Figure 3.4. Different concentrations of trapped mitochondria (labeled with JC-1, red fluorescence shown) achieved by changing the mitochondria concentration in the filling solution. All channels have been pumped with the mitochondria solution rate of 10 µL/hour for 2 min., a) 300 µg/mL protein concentration (density too high), clogs are formed in the trap channels b) 50 µg/mL protein concentration (density optimum), c) 1 µg/mL protein concentration (density low). Bright field and fluorescence images are captured separately and merged later.

While with protein concentration of 1 µg/mL we saw only four mitochondria trapped in the whole channels (Figure 3.4 (c)). Concentration of around 50 µg/mL, on average, resulted in a few mitochondria being trapped per channel (Figure 3.4b) and most of the mitochondria were far enough from each other that we could easily distinguish them with microscope. Since the "clogs" are not observed when lower concentration of mitochondria is used, we believe they are mitochondria that are packed so closely that it is difficult to distinguish between them, the smallest resolvable distance between two mitochondria depends on the specifications of the microscope and is discussed more in the imaging section. The optimum

concentration also depends on the flow rate. With a smaller flow rate, there is more control over the number of trapped mitochondria, the channels can be monitored through the microscope and once an appropriate number of mitochondria are trapped the flow can be stopped, but that would increase the loading time and due to limited lifetime of isolated mitochondria, would decrease the number of the assays that can be performed. We have kept the loading time and the flow rate constant and used a mitochondria concentration that would result in a few trapped mitochondria in each channel. The total amount of mitochondria protein that we are flowing into the channels at a concentration of 50 μg/mL and flow rate of 10 μL/hour for 2 minutes is around 16 ng. This concentration is over an order of magnitude lower than what is used in most experiments.[56,57] This can be used to estimate the appropriate concentration for different flow conditions. The number of trapped mitochondria for each experiment using the described conditions is generally 20-40 in the field of view. It is possible to increase the throughput by increasing the number of nanochannels, and using an imaging system with higher resolution and larger field of view.

$\Delta\psi_m$ Assays

The mitochondria in our channels are vital and sustain a membrane potential. This can be demonstrated using the fluorescence dye JC-1

In Figure 3.5 (a-c), separate green and red fluorescence images of the same mitochondria are shown, as well as their superposition over the bright-field image of the nanochannels. JC-1 stained mitochondria are provided with 10 mM sodium succinate and flown into channels with a rate of 10 μL/hour. After 2 minutes the flow is stopped and the channels are imaged. Clearly, the mitochondria are trapped individually in the nanochannels, and a large

percentage of them are bright red, indicating the membrane potential is still large. The blue bars in Figure 3.5 (d) shows the histogram of red/green fluorescence intensity for 31 mitochondria that were in the field of imaging. Around 80% of the mitochondria have a ratio of 3 or higher. As a control we performed the same experiment with substrate deprived mitochondria that are expected to have a lower membrane potential. The distribution of red/green fluorescence intensity ratio for mitochondria in this sample is shown by the white bars in Figure 3.5 (d). Out of 39 mitochondria, 65% have a ratio of 2 or lower.

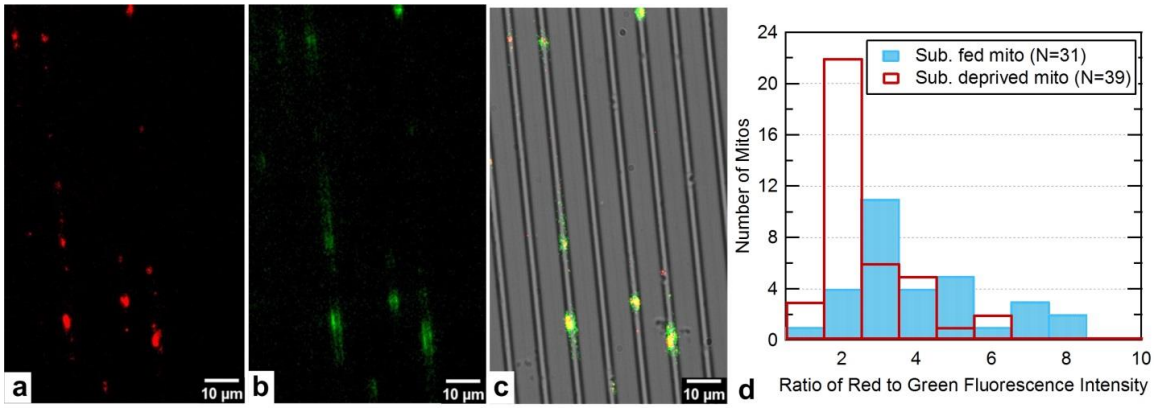

Figure 3.5. Image of JC-1 stained trapped mitochondria. a) Image taken with TRITC filter. b) Same mitochondria imaged with a FITC filter. c) Overlap of a, b and bright field image of the channels. d) Histogram of ratio of red to green fluorescence for substrate fed mitochondria) and substrate deprived mitochondria (Total number of substrate fed mitochondria is 31 and total number of substrate deprived mitochondria is 39).

of stained trapped mitochondria for over ten minutes with continuous illumination.

Mitochondria stained with 30 nM TMRM were introduced into our nanochannels, and an image was captured every 5 seconds, with an image acquisition time of 2.5 seconds per image. As can be seen in Figure 3.6, the fluorescence intensity from TMRM stained mitochondria remains relatively constant indicating that the trapped mitochondria maintain their membrane potential for a long time.

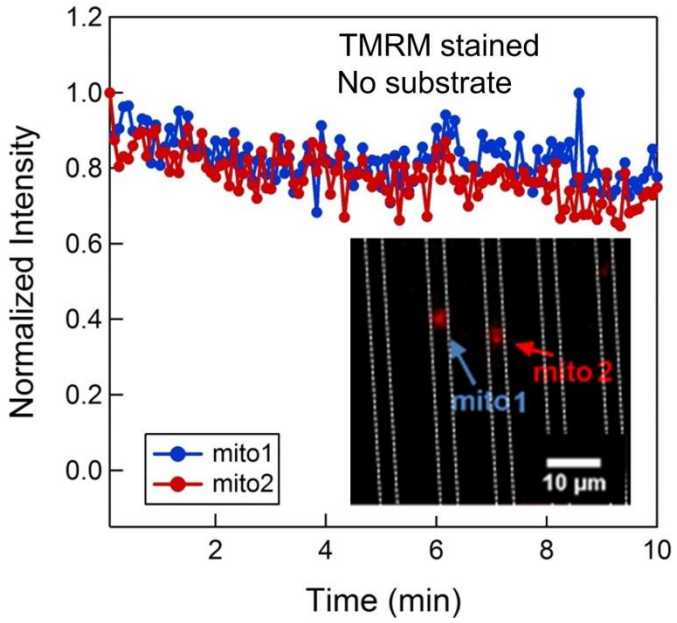

Figure 3.6. Normalized TMRM fluorescence intensity from two individual trapped mitochondria imaged every 5 s. Arrows in the inset point to the mitochondria the intensity of which is shown. Dashed lines suggest the outline of the channels.

The substrate response and MMP experiments described next were performed using JC-1. Because of our microscope setup we can only use one filter cube at a time for time-lapse fluorescence microscopy and we cannot measure both red and green simultaneously, so we only monitored the red intensity (which has been reported to be linearly correlated with membrane potential)[58]. To account for the inaccuracies such as those caused by the apparent size of mitochondria compared to their real size that might be caused by using the red fluorescence only, we are showing the normalized traces for each mitochondrion. Each trace is divided by the fluorescence intensity measured for that mitochondrion at time zero, so that all the traces start at intensity of one. This way we are not comparing different mitochondria, but we are looking at the trend of membrane potential change for one mitochondrion.

Substrate Modulation Δψm of Individual Mitochondria

Without OXPHOS substrates, the electron transport chain is idle, and the membrane potential remains in its basal, resting state. In order to demonstrate the ability to chemically modulate the electron transport chain and the bioenergetic state of the mitochondria in our nanochannels, we performed a series of experiments with and without OXPHOS substrates Pyruvate/Malate present in the respiration buffer.

In Figure 3.7, we show two sets of experiments in which the mitochondria are labeled and imaged with JC-1. In (a), substrates are not used. In (b), OXPHOS substrates, 5 mM Pyruvate and 5 mM Malate, are added to JC-1 stained mitochondria respiration buffer just before flowing the mitochondria in the channels. This activates the electron transport chain and initially increases the mitochondrial membrane potential $\Delta\psi_m$. As mitochondria gradually consume the substrates, the substrate concentration decreases, therefore the membrane potential and fluorescence intensity gradually drop and become identical to the sample without substrates.

Typical normalized red fluorescence intensity of JC-1 stained mitochondria is shown in Figure 3.7 (a) (each curve shows the fluorescence from a single mitochondrion.) It is observed that for JC-1 stained mitochondria the fluorescence intensity has dropped around 50% during the time span that they were continuously illuminated for photography, and we attribute this to photo-bleaching of the JC-1,(also reported by other groups)[59,60] since experiments with identical buffer but different stain (TMRM) showed no appreciable decay in the membrane potential (Figure 3.6).

Similarly, in Figure 3.7 (b), the fluorescence intensity decays with time but this time with a higher rate, due to gradual consumption of OXPHOS substrates

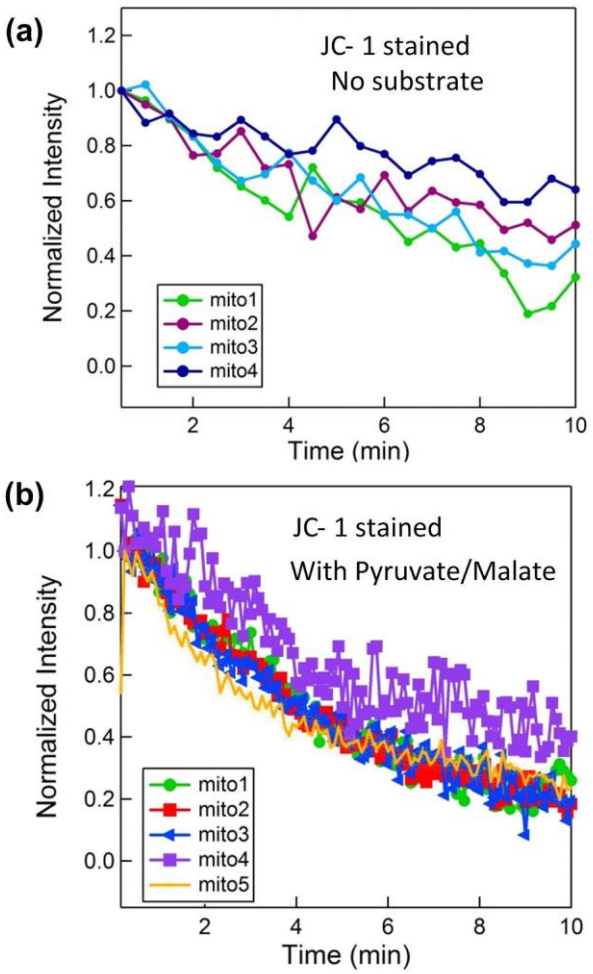

Figure 3.7. Fluorescence intensity measurement of JC-1 stained mitochondria. a) Substrates are not used. b) OXPHOS substrates (5 mM Pyruvate and 5 mM Malate) are added to respiration buffer just before flowing the mitochondria into the nanofluidic channel. This activates the electron transport chain and increases the mitochondrial membrane potential $\Delta\psi_m$ initially.

Interestingly, for one of the mitochondria (labeled mito4 in Figure 3.7 (b), we observed around 20% fluctuation in the fluorescence intensity. Fluctuations (flickering) of membrane potential of individual mitochondria from different cell types have been reported before, although the detailed conditions and causes of this flickering are not fully understood.[57,61–63] Our study is the first to observe such flickering in isolated mitochondria from HeLa cell line, and it is surprising that it is observed in substrate fed (rather than basal) mitochondria, which is contradictory to some other studies,[56] where removal of substrates resulted in flickering in

some mitochondria. Even though JC-1 is a slow response dye,[64] it has been shown that the observed flickering when using JC-1 is very similar to TMRM but with a slightly lower frequency.[65] It is our belief that the technique demonstrated herein could be useful for future studies to more quantitatively elucidate the flickering of the membrane potential, its causes, and modulators.

Calcium Induced MMP

Calcium in mitochondrial matrix controls the rate of energy production. In case of pathological calcium overload mitochondrial permeability transition pore opens irreversibly causing the mitochondria membrane to become abruptly permeable. This results in mitochondrial depolarization and swelling.

A solution of 10 mM $CaCl_2$ in DI water was prepared and diluted 10 times in respiration buffer to the final calcium concentration of 1 mM. The osmolarity of the final respiration buffer solution with 1 mM $CaCl_2$ is about 310 mOsm, which is well within the physiological osmolarity range for mitochondria.[66,67] We used a very high concentration of Ca^{+2} to make sure that the amount of calcium that reaches the mitochondria is enough to cause the swelling. The solution was pumped into the channels (with a relatively low flow rate of 5 μL $hour^{-1}$ to make sure it will not dislodge the trapped mitochondria) to induce depolarization. In order to avoid the photobleaching of JC-1, we imaged the mitochondria prior to the introduction of Calcium solution, started Calcium flow, stopped the light exposure and waited for 4 minutes. Then we turned on the illumination and imaged the same field again. (Figure 3.8) The red/green fluorescence intensity of most of the mitochondria had considerably decreased. This clearly indicates the membrane potential has been significantly reduced by the Ca^{2+}.

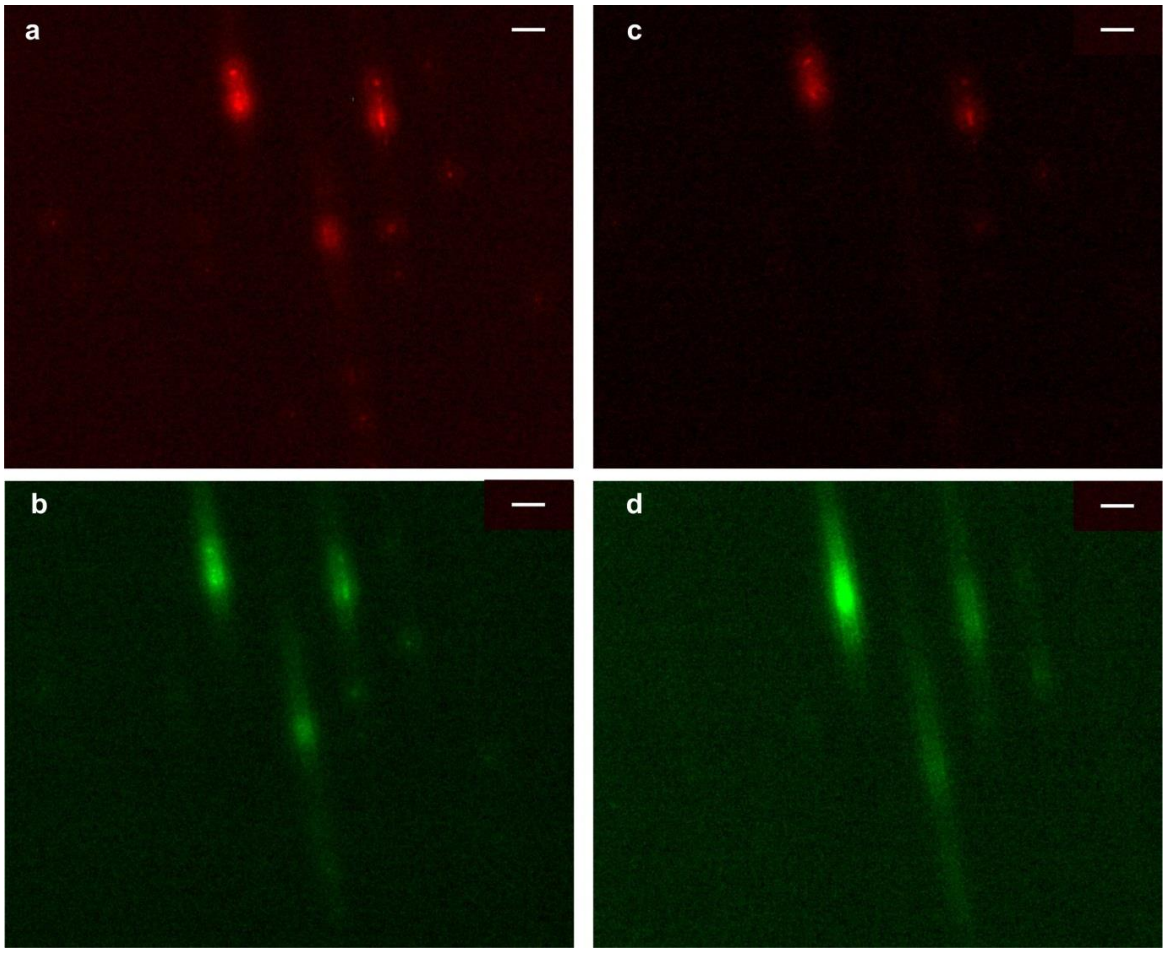

Figure 3.8. (a) and (b) Trapped mitochondria before flowing the respiration buffer with1mM Ca+2 in the channels. (c) and (d) Same mitochondria after exposure to 1mM calcium flow. Scale bar is 5 µm.

To quantify this effect, we compared the red fluorescence to green fluorescence intensity ratio prior to and after calcium treatment. The red/green ratio for all 14 mitochondria varied, but shifted to a lower value after introduction of the Calcium. In Figure 3.9, the histograms of the ratios (which is indicative of the membrane potential $\Delta\psi_m$) for the pre and post Calcium treatment are plotted. Interestingly, the results indicate the membrane potential has collapsed for all but one mitochondrion, regardless of the initial membrane potential (i.e. red/green ratio). This demonstrates the ability to study heterogeneity and statistical properties of individual mitochondria.

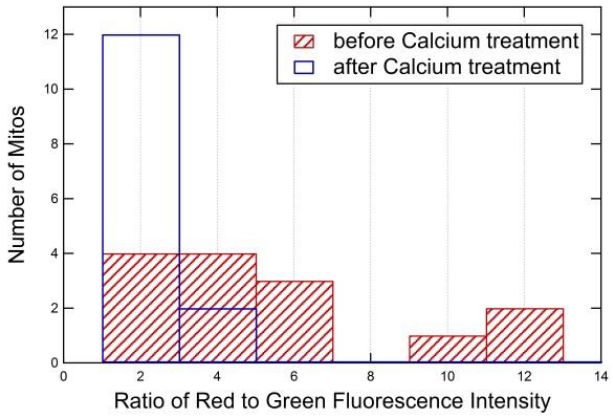

Figure 3.9. Histogram showing the distribution of JC-1fluorescence intensity ratio for the 14 mitochondria involved in the study prior to (red bars) and after calcium treatment (white bars).

Comparison to State of the Art

The vast majority of assays performed on mitochondrial function are on large quantities of mitochondria, typically requiring 10^7 cells worth of sample.[64] Below we compare our work with prior art for the analysis of individual mitochondria, of which there are only a few techniques, none of them suitable for the studies envisioned with our technology.

An alternative technique to immobilize isolated mitochondria involves adhesion to a glass microscope slide.[68–70] This technique allows visualization and characterization of up to hundreds of individual mitochondria in a single field of view. A disadvantage of this approach, however, is the large fluorescence background of the fluorophore outside of the mitochondria. If one seeks to quantitatively determine $\Delta\psi_m$ using potential sensitive dyes, it is necessary to carefully measure the ratio of the dye fluorescence intensity at the inside to the outside of the mitochondria. The measurement is complicated by the large diffuse fluorescence background of the fluorophore outside of the mitochondria. In our nanochannels, the volume of solution outside the mitochondria is minimized, leading to much lower background fluorescence. Another advantage of our method is that mitochondria

are physically trapped and cannot move around or move out of the plane of focus, allowing us to do accurate measurements. In glass immobilization method a large portion of the mitochondria do not stably get attached on the glass surface, preventing the accurate measurement of their fluorescence intensity since small movements of mitochondria will result in changes in the measured fluorescence intensity and disrupt the measurement. More importantly, parallel processing of multiple analytes is not possible on glass slide. In the fluidic channel array, it is possible to provide a large variety of different chemical environments (one in each channel) with suitably designed on-chip microfluidic circuits. For example, each of the 10 channels could be given a linearly varying concentration of Ca^{2+} by suitable design of a perpendicular microfluidic Ca^{2+} gradient at the introduction of each channel. This could allow for parallel screening in response to different calcium concentrations at the single mitochondria level, which the glass slide approach cannot easily provide. Generalizations to arbitrary chemical combinatorial conditions are clearly possible.

Several studies have demonstrated the application of flow cytometry to the analysis of individual mitochondria.[71,72] Flow cytometry has the advantage of using existing commercially available instruments. Flow cytometry provides a "snap shot" of a single mitochondrial state (*e.g.* JC-1 fluorescence, forward scatter and side scatter). In this way, statistical analysis of mitochondria under various conditions and states can be obtained. Flow cytometry cannot be used to track the status of individual mitochondria over a long time. In contrast, in our approach, the response of individual mitochondria to a variety of chemical species can be tracked over a long period of time.

Similar to flow cytometry, capillary electrophoresis with laser-induced fluorescence detection allows for analysis of single mitochondria. In this technique, a 50 μm capillary

guides individual mitochondria which migrate in response to a high electric field (*ca.* 200 V cm^{-1}). Using this technique, a variety of mitochondrial properties can be assayed, such as the electrophoretic mobility, the cardiolipin content, and ROS production.[73–78] As in flow cytometry, single mitochondria are analyzed at a snapshot in time as they migrate passed the detection window.

In short, the current approach supplies temporal information, the CE provides chemical information and the flow cytometry provides statistics on large populations.

Conclusion

We present for the first time a nanofluidic chip to trap and study isolated individual mitochondria. This provides a powerful stage for fluorescence imaging of isolated mitochondria in a controlled environment and real time investigation of their behavior under influence of different chemicals. Multiple applications of the new technology can be envisioned. We expect that the application of this and similar technologies to the analysis of sub-cellular organelles will have a variety of applications in cancer biology, stem cell biology, drug screening, and aging studies, because of the growing consensus of the general importance of functional metabolomics in biology and medicine.

Acknowledgements

This work was supported in part by the following grants awarded to D.C.W.: NIH-AG24373, NS21328, AG13154, DK73691, CIRM Comprehensive Grant RC1-00353, and a Doris Duke Clinical Interface Grant 2 005 057. P.B. acknowledges support of this work from

NIH National Cancer Institute Grant 1R21CA143351-01, as well as support from the ARO (MURI W911NF-11-1-0024).

This chapter is a reprint of the material as it appears in (Zand, K., Pham, T., Davila, A., Wallace, D. C., & Burke, P. J. (2013). Nanofluidic platform for single mitochondria analysis using fluorescence microscopy. *Analytical Chemistry*, *85*(12), 6018–25). The co-authors listed in this publication directed and supervised research which forms the basis for this chapter.

CHAPTER 4 : Resistive Flow Sensing of Vital Mitochondria with Nanoelectrodes

Introduction

Mitochondria regulate and generate energy in a cell, control cell fate through the apoptosis cell death pathway, and are believed to be the main producers and targets of reactive oxygen species. [13 79]A series of membrane protein complexes (the electron transport chain) converts the chemical energy stored in various metabolic substrates into electrical energy (stored as a membrane potential of around 150 mV), resulting ultimately in the reduction of oxygen to water. The mitochondrial membrane potential energizes the phosphorylation of ADP to ATP through the F_0F_1 ATP synthase. One of two cell death signaling pathways (the so-called "intrinsic" or mitochondrial signaling pathway) converges at the mitochondrial membrane and causes a dramatic and sudden collapse of the mitochondrial membrane potential, irreversibly committing the cell to death[33,80]. This is a highly regulated pathway and clear target for pharmacological manipulation for a variety of diseases including, e.g, cancer[818235]. While the molecular identity of the complex of proteins that leads to this collapse (the so called permeability transition pore (PTP), presumed to be a large channel) is controversial[83], the dynamics and statistics of the membrane potential collapse and in particular of the PTP opening and closing are, to date, impossible to measure with time resolution less than about 1 second, in spite of evidence of rapid flickering of the membrane potential. New, faster assays of the mitochondrial membrane potential could therefore provide important new information about a biophysical quantity that is critical for cellular energy production and, through apoptosis, cell fate.

The simplest and most convenient method to assay the membrane potential utilizes a charged, lipophilic fluorescence dye (typically Tetramethylrhodamine, Methyl Ester Perchlorate, known as TMRM) that can freely pass through a lipid bilayer membrane. The

dye concentration inside the mitochondria (and hence measured flourescence intensity) changes in response to the membrane potential through the Nernst relationship. Although convenient and prevalent, this technique is limited in the spatial resolution so that the entire mitochondria is typically a few pixels in size, and in temporal resolution, because of the weak fluorescence signal. Although fluctuations of the membrane potential in time have been demonstrated ("flickering"), [56,57,62,63,65,70,84–92] especially in the context of apoptosis and cell death, limitations on fluorescence assays have prevented investigation of the spatial distribution of the membrane potential along the length of the mitochondria, and flickering/fluctuations with time scales less than about 100 ms,[93] even though they are believed to be due to the dynamic opening and closing of pore forming complexes, the permeability transition pore (PTP).

In this work, we demonstrate proof of concept of an alternative method to measure mitochondrial membrane potential using nanotube electrodes which sense the mitochondria as they flow passed the electrodes one by one. With this initial proof of concept, we demonstrate a statistical noise resolution on the membrane potential measurement of better than 10 mV in 3 milliseconds, at least an order of magnitude faster than any published fluorescence membrane potential measurement. In addition, we present a careful, quantitative analysis of the fundamental and practical limits of membrane potential measurements using fluorescence microscopy and show that our initial proof of concept electrical assays provide superior time resolution even when compared against a (hypothetical) perfect, shot noise limited fluorescence configuration.

While an obvious advantage of this approach (in addition to dramatically improved time resolution) is the compatibility to scale to high throughput assays on millions of individual

mitochondria at a time using modern CMOS electronics (which fluorescence approaches are not compatible with), the most exciting possibility of this approach is the potential to scale the spatial resolution down to that of a single ion channel. Our recent demonstrations[94–97] of using nanoelectrodes to sense the current through individual ion channels indicates this is an exciting avenue for extending this initial proof of concept to enable qualitatively new methods of investigating mitochondrial electrophysiology using nanotechnology.

Mitochondrial Nanoelectrode Sensor: Design & Fabrication

Our design consists of an array of nanotube transistors fabricated on a 4" quartz wafer (Figure 4.1). A PDMS microfluidic channel (1 μm by 2 μm by 500 μm) enables delivery of electrolyte buffers that act as a liquid "gate" to turn the nanotube channel on and off when a suitable voltage is applied using a Ag/AgCl electrode at the channel entrance (Figure 4.2). The channel dimensions are designed to allow passage of mitochondria (which typically are about 0.5 μm across) one by one across the surface of the nanotube electrodes, which then sense the electrical charge of the mitochondria as they pass by.

The active nanotube channel consists of a random network of purified semiconducting carbon nanotubes with a density of approximately 20 tubes/μm^2, deposited using methods recently developed by our lab .[98,99] This provides a simple method to integrate with optical lithography for patterning of the metal contacts to the nanotube network. In our design, only the nanotubes (and not the metal contacts) are exposed to the solution.

The metal contacts to each side of the nanotube network serve as "source" and "drain" electrodes. The conductance from source to drain is measured using either a semiconductor parameter analyzer or a lock-in analyzer (see methods). The interfacial capacitance (gate

capacitance) is composed of three components; the electrolyte-CNT double layer capacitance, tube-tube capacitances and quantum capacitance of carbon nanotubes. Electrolyte-CNT double layer capacitance for salty water is around $7x10^{-9}$ F/m[100], and the tube-tube interactions are negligible. The quantum capacitance of a carbon nanotube is $4x10^{-10}$ F/m which is more than 10 times smaller than the contribution from the double layer capacitance and therefore is the dominant component of the gate-carbon nanotube capacitance. The total interfacial capacitance is approximately 1 μF/cm^2. Based on this capacitance estimation Mobility for holes is calculated as 0.6 cm^2/(V·s) and the calculated electron mobility is 0.15 cm^2/(V·s).

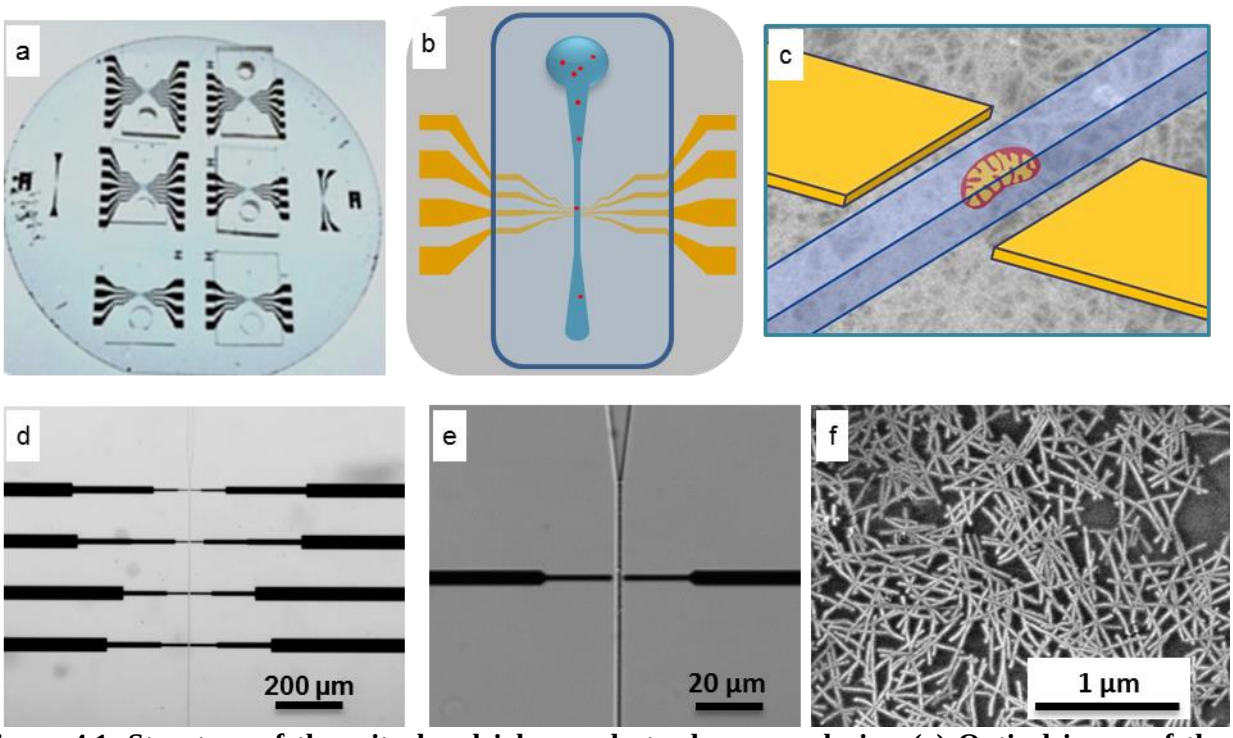

Figure 4.1. Structure of the mitochondrial nanoelectrode sensor device. (a) Optical image of the quartz wafer with 6 devices. (b) Schematic of the device showing the PDMS channel and the integrated electrodes. (c) Schematic showing the relative location of the carbon nanotube transistor and the flowing mitochondria. (d) and (e) Bright field microscope images of the device with 20x and 60x magnifications. (f) Scanning electron micrograph exhibiting the carbon nanotubes deposited on the wafer surface.

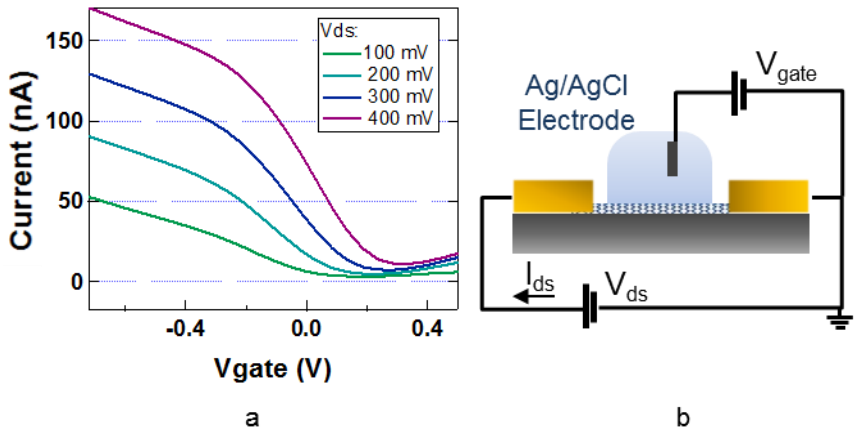

Figure 4.2. DC characterization of the device. (a) Drain-Source current vs. (electrolyte) gate voltage for a 3 µm x 3 µm device at different applied drain-source voltages. (b) Schematic showing the DC measurement set-up.

Resistive flow sensing of vital mitochondria

Vital mitochondria, isolated from HeLa cells using well known protocols,[101] are introduced into the channel using a variety of buffers known to affect the metabolic & bioenergetics status of the mitochondria (Figure 4.3). As the mitochondria flow over the nanoelectrode network, distinct changes in the conductance are observed (Figure 4.4). Control experiments using buffer only (no mitochondria) show a constant conductance, confirming the changes in the conductance are due to the presence of the mitochondria (Fig. 4). Since mitochondria in its vital state sustains a large membrane potential, the surface has a net charge which "gates" the nanotube devices into a less conducting state (Figure 4.3). Once we achieved this initial proof of concept, we turned our attention to the effect of the metabolic state of the mitochondria on the measured conductance change pulse heights.

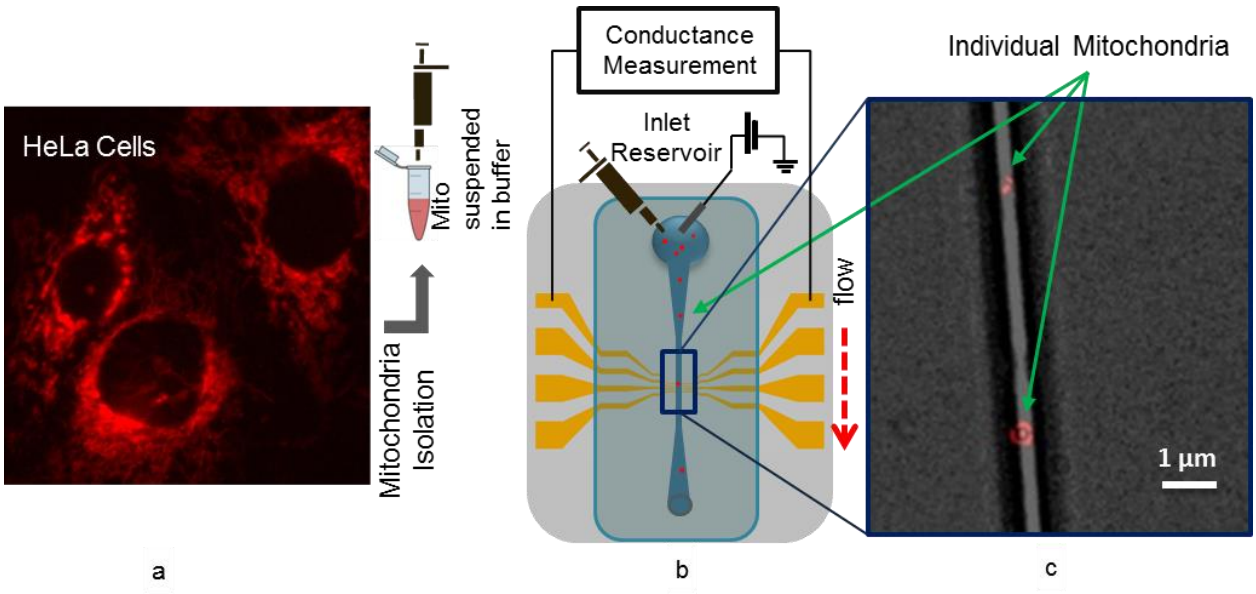

Figure 4.3. Mitochondria detection set-up. (a) Fluorescence image of HeLa cells labeled with TMRM dye. TMRM stains the mitochondria inside the cells. Mitochondria are isolated from HeLa cells and suspended in buffer. (b) Schematic depicting the electrical measurement with lock-in amplifier. Buffer containing the isolated mitochondria is pipetted in the inlet reservoir of the channel and flows through the channel. (c) Fluorescence image of TMRM labeled individual mitochondria in the fluidic channel.

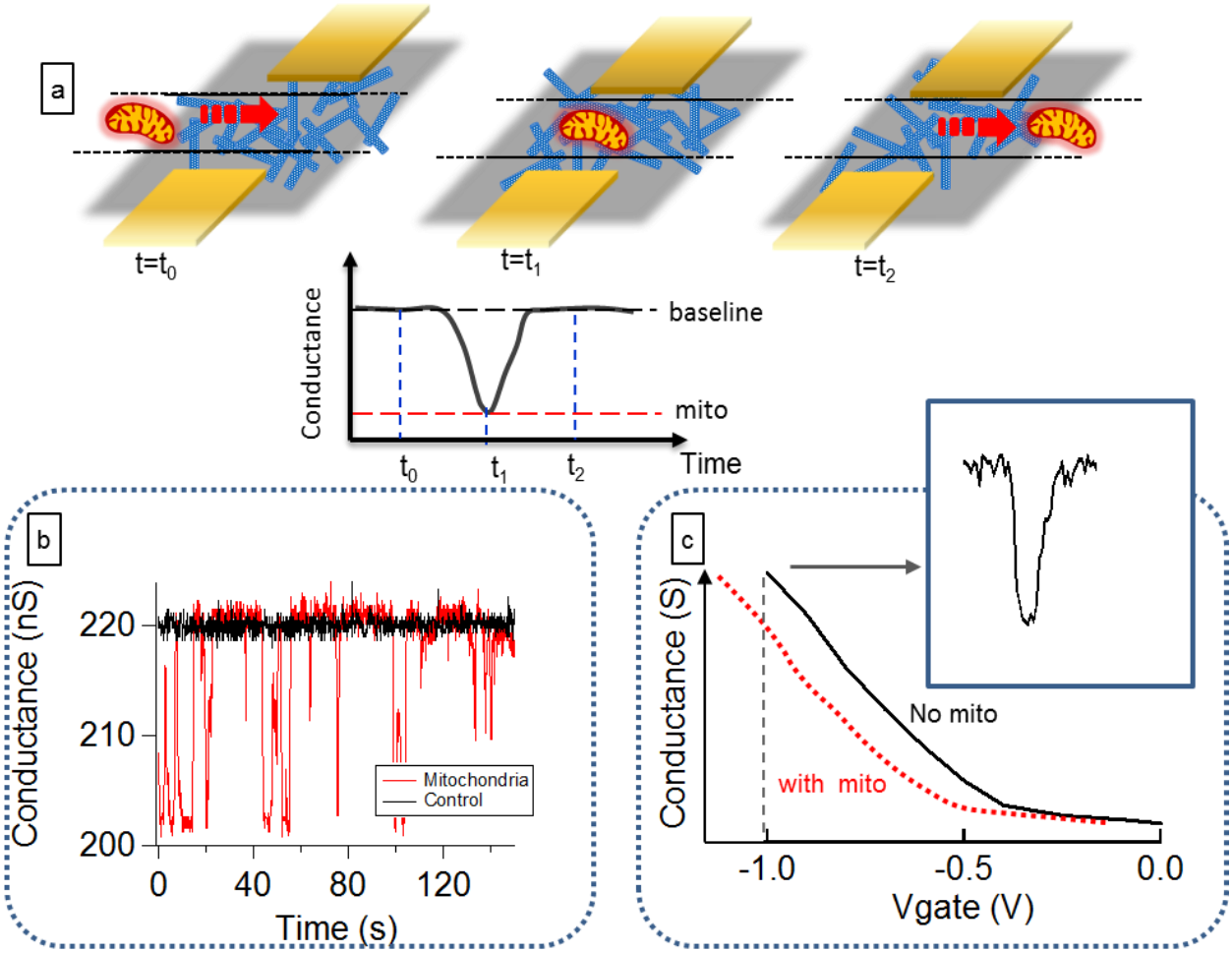

Figure 4.4. Carbon nanotube detection of vital, individual mitochondria. (a) As a mitochondrion approaches the nanotube electrodes, the source drain current starts to change, and when the mitochondria moves past the transistor channel area, the device current goes back to the baseline. (b) Conductance vs. time data recorded from a device without mitochondria in the flow buffer (black trace) and with mitochondria flowing in the channel (red trace). The spikes in the red curve correspond to mitochondria passing over the sensor area. This device is biased at a (liquid) gate voltage of -1 V. (c) The magnitude and direction of spikes depend on the gate bias voltage. The current change is negative for negative bias voltages, indicating a negative shift of the device threshold voltage as mitochondria approach the device.

Threshold voltage shift

For a negative gate voltage, mitochondria induce a decrease in the conductance, whereas if the device is biased at a positive gate voltage the current changes are in the opposite direction (Figure 4.5). This trend shows a negative shift in the threshold voltage of CNTFET.[102] We attribute this change to induction of electrons in the carbon nanotubes due

to the surface charge of the mitochondria. The inner mitochondrial membrane maintains a transmembrane potential. The transmembrane potential is created as protons are pumped into the intermembrane space as a result of redox reactions in the electron transport chain. The anions remain in the matrix and cause a negative charge density in the mitochondrial matrix while the positive ions accumulate outside of the mitochondria and screen the negative charges in the matrix[103]. The details of the distribution of charges on the mitochondrial surface is not known yet. Our measurements indicate the induction of a negative charge density in the CNT mat.

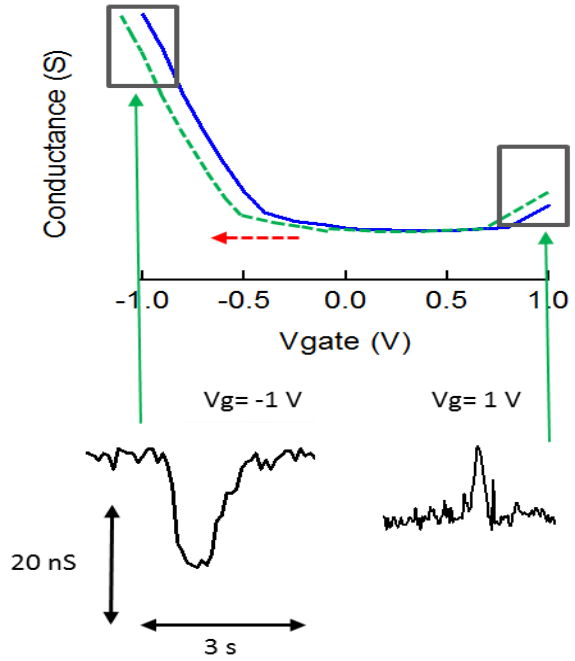

Figure 4.5. The magnitude and direction of spikes depend on the gate bias voltage, the current change is negative for negative bias voltages and positive for positive bias voltages, indicating a negative shift of the device threshold voltage mitochondria approach the device.

Mitochondrial energetic state can be assayed with nanoelectrodes

In order to further demonstrate the utility of this approach, we next assayed the mitochondrial induced conductance change under three common biochemical conditions[11]: 1)

Substrate deprived mitochondria. These mitochondria are depleted of their endogenous substrates and the membrane potential is low, due to lack of chemical energy to fuel the electron transport chain proton pumps. This is commonly referred to as Respiratory State 1.[11] 2) Succinate fed mitochondria. Succinate is a substrate that fuels complex II of the electron transport chain, causing a large membrane potential, in the absence of ADP. This is commonly referred to as Respiratory State 2.[11] 3) Depolarized mitochondria. The chemical agent CCCP (carbonyl cyanide m-chloro phenyl hydrazine) is a lipid soluble uncoupling agent that discharges the proton gradient and results in the collapse of the membrane potential of mitochondria.

In state 1 (substrate deprived), the change in the electrode conductance is measurable but small (Figure 4.6). Once the mitochondria are provided with substrates (state 2), the concomitant changes in the nanotube conductance are much larger, due to the larger membrane potential. After depolarization of the membrane potential with CCCP, no further pulses are observed. This clearly demonstrates that the nanoelectrode conductance change is a sensitive probe of the mitochondrial membrane potential, and probe the bioenergetics state of individual mitochondria.

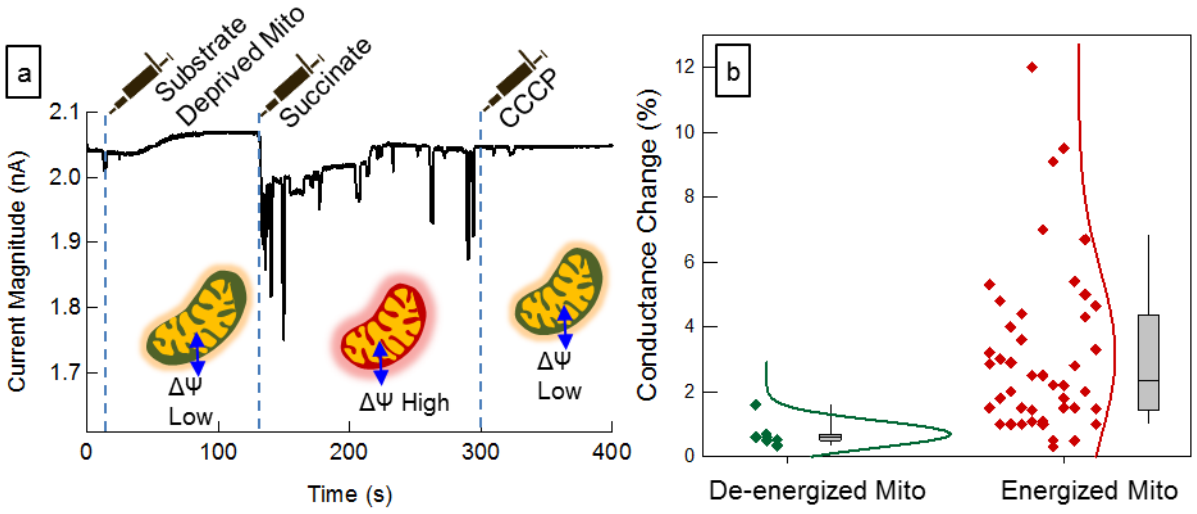

Figure 4.6. Effect of the metabolic/bioenergetic state of the mitochondria on the conductance change. (a) Addition of different reagents to the reservoir during the measurement alters the membrane potential of mitochondria. Initially mitochondria were suspended in a substrate free buffer and flown into the channel; next mitochondria were energized by adding sodium succinate to a final concentration of 10 mM; finally CCCP was added to the reservoir (final concentration 50 µM) to depolarize the mitochondria. (b) Normalized scatter plot showing the distribution of the events observed for energized and de-energized mitochondria.

Mitochondrial membrane potential fluctuations can be quantitatively assayed

Our measurements above clearly show the conductance change is sensitive to the metabolic state of the individual mitochondria (i.e. to its membrane potential). Prior measurements have shown that the surface charge of the mitochondria (which is responsible for gating our nanotubes) is related to the membrane potential (Figure 4.7).

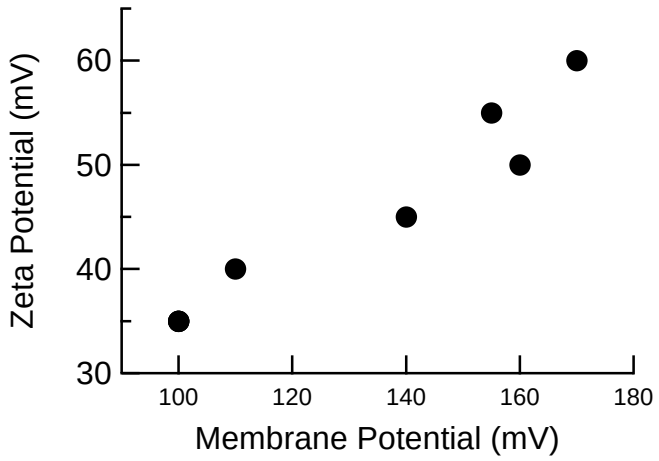

Figure 4.7. Linear relationship between mitochondrial membrane potential and surface potential (adapted from Table 1 in reference[104] and Figure 2 in reference[105]). In the original reference, the membrane potential of the isolated mitochondria was measured with an ion-selective electrode, and the electrophoretic mobility was measured using a miro-electrophoretic device. The electrophoretic mobility was used to calculate the surface potential (surface charge density). The surface potential and membrane potential were given separately versus different mitochondrial bioenergetics stimulants and inhibitors; here those data are merged to plot the surface potential versus membrane potential. This shows a clear linear relationship between the two parameters.

While an absolute calibration of the membrane potential is challenging, it is clear that we can sensitively assay changes in the membrane potential from one mitochondria to the next, and as a function of the metabolic state of the mitochondria in response to its biochemical environment. We now discuss how to calibrate the sensitivity of this technique to differences in membrane potential from the measured conductance change.

The change in the conductance of the nanoelectrode is larger at larger mitochondrial membrane potentials. Due to the capacitive nature of the detection mechanism, the assumption of a linear small signal relationship between the magnitude of change in conductance and the membrane potential of mitochondria is reasonable. Assuming that the resting membrane potential is 150 mV, we can calibrate the sensitivity of the device by measuring the current change from baseline. In our proof of concept devices, at a gate bias

voltage of -1 V, an average of 0.1 nA (4.5%) current change from the base line occurs as the energized mitochondria pass over the detector. This gives a current to membrane potential conversion factor of typically 0.1 nA per 150 mV of mitochondrial membrane potential. Using this, an estimate for the statistical noise in the membrane potential measurement can be ascertained.

With a second order low pass filter with time constant of 3 ms, the measured standard deviation of measured current in the absence of mitochondria ranged from as low as 1.2 pA to as high as 8 pA. By increasing the time constant and the order of the low pass filter the output becomes less noisy. The time constant and the filter order also determine how long does it take for the filter output signal to respond to changes in the device conductance. For these filter settings the delay time (time it takes for the measured current to reach 50% of its final value) is approximately 5 ms.

For error calculations we assumed a standard deviation of 6 pA. This corresponds to a maximum of 9 mV of error in the measurement of a membrane potential of -160 mV for a measurement time of 3 ms. This is an unprecedented measurement as the prior best result has a measurement time of almost 2 orders of magnitude longer (100 ms) based on fluorescence, and most fluorescence measurements are even longer than that (second). It should be pointed out that the noise sources in our electronic measurement have not been analyzed in detail and this measurement represents an initial proof of concept spot measurement of the noise that could be improved with further effort. We next compare the initial proof of concept device realized in our lab with the fundamental limit that fluorescence microscopy can be expected to provide under optimum conditions, as well as practical conditions with various commercially available camera systems.

Comparing the fundamental and practical limits of fluorescence membrane potential assays

Fluorescence imaging of vital mitochondria is the established method for the study of membrane potential of single mitochondria using membrane potential sensitive dyes ("voltage dyes").[106,107] In this method the membrane potential indicator is generally a lipophilic cationic fluorescence dye that is taken up by mitochondria in proportion to the membrane potential according to the Nernst equation. Mitochondria with higher membrane potential accumulate more dye in the matrix. The fluorescence intensity of the dye is dependent (usually linearly) on the concentration of dye. Fluorescence intensity of the dye is detected inside and outside of the mitochondrion and the ratio is used to calculate the membrane potential.

Although this is a powerful tool, it has some disadvantages associated with it. First, high intensity illumination generates reactive oxygen species in mitochondria and leads to phototoxicity which in many cases actually causes ROS induced depolarization of the membrane potential one is trying to study.[108] This effect (in addition to photobleaching of the fluorescence dye) constrains the maximum the illumination intensity that can be used, and hence the maximum brightness that can be expected from the flourophores. In this section, we analyze this relationship in detail and develop quantitative estimates for the best case scenario fluorescence measurement of membrane potential, as well as that for practical configurations with commercially available cameras of various cost and sensitivities.

There are various fluorescence probes that can be used to assess the mitochondrial membrane potential. Examples of the most commonly used fluorescent dyes are tetramethylrhodamine methyl ester (TMRM), tetramethylrhodamine ethyl ester (TMRE),

Rhodamine 123 and JC-1. TMRM has been shown to have the lowest non-Nernstian binding to the membrane[8] and therefore is suitable for quantitative measurements of membrane potential.

The fluorescence intensity of the dye can be measured by a wide-field or confocal microscope. Confocal microscopy leads to a better spatial resolution compared to the wide field Epi-fluorescence microscope, it also enables 3-D reconstruction of the image and elimination of out of focus fluorescence. On the other hand, it needs a higher excitation light intensity that induces faster photo-bleaching of the fluorophore and might also cause phototoxicity in mitochondria. Here we base our analysis on wide field fluorescence microscopy of TMRM labeled mitochondria.

In order to determine the resolution of the measurement of the membrane potential, we first determine the noise on the measurement of the fluorescence intensity, and later convert that to a noise on the measured membrane potential. Noise sources on the fluorescence intensity measurement can come from many sources, but in a properly optimized lab setup, are dominated by three main contributions:

1) Shot noise of the emitted light due to the discrete nature of the photon
2) Dark current noise on the photodetector
3) Read noise on the CCD readout electronics.

Table 4.1. Specifications and coefficients used to drive the accuracy of membrane potential measurements by fluorescence microscopy

<table>
<tr><th colspan="2">Microscope System</th><th colspan="2">TMRM Characteristics</th></tr>
<tr><td>Illumination</td><td>120 W-Mercury lamp</td><td>Absorption/Emission</td><td>549/574 nm</td></tr>
<tr><td>Filter Cube</td><td>TRITC</td><td>Quantum Yield</td><td>0.34</td></tr>
<tr><td rowspan="3">Objective Lens</td><td rowspan="3">Oil Immersion
60X
NA=1.4
Field Number : 22 mm
FOI= 0.001 cm^2</td><td>Extinction Coefficient</td><td>1.1 x10^5 $M^{-1}cm^{-1}$ [109]</td></tr>
<tr><td>Absorption Cross Section</td><td>3.824 x 10^{-19} cm^2</td></tr>
<tr><td>Concenteration (Nonquench)</td><td>1-30 nM</td></tr>
<tr><td colspan="4">Mitochondrial Matrix Volume: 0.04-0.08 μm^{-3} [110]</td></tr>
</table>

We next estimate the noise in the measured fluorescence intensity from these main contributions, using typical parameters for a membrane potential experiment (Table 4.1). At a typical power density of 60 W/cm^2, the flux of photons incident on a 1 μm^2 mitochondrion is 1.7 x 10^{12} photon.s^{-1}. Although it is possible to use higher powers to illuminate mitochondria, phototoxicity effects have been reported for even lower illumination powers.[65,84]

How many photons does a TMRM labeled mitochondrion emit per second? The number of photons emitted by a single fluorophore per second can be calculated from the following equations described in:[111]

$f_{\lambda em} = f_{\lambda ex} . B_s$ (Equation 4.1)

Where $f_{\lambda em}$ is the photon emission rate in photons per molecule per second, $f_{\lambda ex}$ is the incident light intensity in photons per second per square centimeter and B_s is the brightness which, at the single molecule level is calculated from:[111]

$$B_s = \phi_{\lambda ex/\lambda em} \cdot \sigma_{\lambda ex} \qquad \text{(Equation 4.2)}$$

$\phi_{\lambda ex/\lambda em}$ is the fluorescence quantum yield of TMRM molecules , and $\sigma_{\lambda ex}$ is the absorption cross section of a single fluorophore molecule in square centimeter, Using the values given in Table 4.1, the brightness of a TMRM molecule is calculated to be 0.13 x 10^{-18} cm^2. Therefore for each molecule of TMRM under the above discussed excitation condition the photon emission rate is 22 photons/s/molecule.

The concentration of TMRM in an energized mitochondrion can be calculated from Nernst equation:

$$\Delta\Psi = 2.303 \frac{RT}{zF} \log \frac{[C_{out}]}{[C_{in}]} \qquad \text{(Equation 4.3)}$$

Where C_{in} and C_{out} are ion concentrations inside and outside the mitochondria, respectively, T the temperature, z the charge on the ion, F Faraday's constant, and R the ideal gas constant. The effect of non-Nernstian binding of TMRM has been ignored since it has been shown that it is relatively low. Taking the higher end of 30 nM TMRM concentration in the respiration buffer, for a mitochondrion with a membrane potential of -160 mV, the concentration of dye inside the mitochondria is 15 µM. Therefore there are approximately 550 TMRM molecules inside the mitochondria, and the total number of photons emitted from each mitochondrion is 12000 photon/s. The objective assumed in Table 4.1 has a 1.4 NA and therefore captures 30% of the photons. Part of the light is also lost while being transmitted through the objective and dichoric mirror. The flux of photons emitted by a mitochondrion arriving at the camera detector is estimated as 3000 photons/s. The average number of

photons arriving at each camera pixel every second can be calculated by dividing this photon flux by the total area of the mitochondrion on the image in pixels.

Noise of fluorescence intensity measurements

Fluorescence measurement is fundamentally limited by the statistical uncertainty of photon emission and detection. The rate of electron generation in the photodetector is not a constant value but follows a Poisson distribution. The average value (S_{avg}) and variance (σ^2) in the number of electrons generated in the photo-detector in an exposure time of t_0 is equal to:

$$S_{avg} = f_0 Q_e t_0 \qquad \text{(Equation 4.4)}$$

$$\sigma^2 = f_0 Q_e t_0 \qquad \text{(Equation 4.5)}$$

Here f_0 is the average number of incident photons per pixel per unit time and Q_e is the quantum efficiency of the detector. This variance generates a noise (shot noise or Poisson noise, N_p) in the number of the detected electrons that is given by:

$$N_p = \sqrt{f_0 Q_e t_0} \quad (\#electrons) \qquad \text{(Equation 4.6)}$$

The lowest bound on the noise in fluorescence microscopy is reached with an ideal detector, where N_p is the only source of noise and camera quantum efficiency is 1. In case of imaging TMRM labeled mitochondria, the total photon flux emitted by a mitochondrion was calculated in the previous section as 3000 photons/s. The lowest shot noise is achieved when all the photons arrive at a single pixel (f_0 = 3000 photons/pixel/s) and the generated noise in this case is equal to:

$$N_p = \sqrt{3000.\, t_0} \approx 55\sqrt{t_0} \quad \text{(\#electrons)} \qquad \text{(Equation 4.7)}$$

This gives rise to a signal to noise ratio of:

$$SNR_{limit} = \frac{S_{avg}}{N_p} = 55\sqrt{t_0} \qquad \text{(Equation 4.8)}$$

The magnitude of the noise and also SNR depend on the duration of the exposure time (also referred to as the integration time).

We next take into account the practical case where other sources of camera noise are present and the quantum efficiency is smaller than 1. In this case, other major sources of noise are the camera dark noise, N_D, which is caused by thermally created electron-hole pairs in camera pixels, also following a Poisson distribution ($N_D = \sqrt{D.t_0}$), and the camera read noise, N_R , from the camera amplifier circuit (Figure 4.8 (a)). [112] The values for D (electrons/pixel/s) and N_R (electrons rms/pixel) depend on the camera type. Assuming emission from TMRM molecules is the only source of light and there is no background fluorescence, the total noise intensity is given by:

$$N_t = \sqrt{N_p^2 + N_R^2 + N_D^2} \qquad \text{(Equation 4.9)}$$

taking into account the camera quantum efficiency, dark current, read noise and the photon shot noise, and the binning mode, the practical signal to noise ratio is given by:

$$SNR_{practical} = \frac{f_{.0}M..t_0.Q_e}{\sqrt{f_{0.}M.t_0.Q_e + N_R^2 + D.M.t_0}} \qquad \text{(Equation 4.10)}$$

Here M is the number of binned pixels. As a result of binning, adjacent pixels are combined together and their charges are read simultaneously. This improves the SNR and also allows for faster pixel read outs.

What is the error in ΔΨ caused by noise of the fluorescence measurement?

Assuming a linear relationship between the emitted fluorescence intensity and the TMRM concentration (which holds at low concentrations of TMRM), the mitochondrial membrane potential can be found from:

$$\Delta\Psi = 2.303\frac{RT}{zF}\log\frac{[C_{out}]}{[C_{in}]} = -59\log\frac{f_0}{f_{out}}\ mV \quad \text{(Equation 4.11)}$$

Here f_0 and f_{out} are the measured fluorescence intensity from inside and outside the mitochondrion, respectively. Using analysis similar to the one used to find f_0, f_{out} can be calculated. The total photon flux that reaches the camera pixels from TMRM molecules in solution outside of mitochondria, is approximately 1 photons/s/pixel for typical camera pixel sizes.

Measurement Accuracy of Absolute Membrane Potential Changes

The sensitivity of the membrane potential to changes in the fluorescence intensity can be calculated from:

$$\partial(\Delta\Psi) = 59\frac{1}{ln10}\left(\left|\frac{\partial f_0}{f_0}\right| + \left|\frac{\partial f_{out}}{f_{out}}\right|\right) = -59\frac{1}{2.3}\left(\frac{1}{SNR_{in}} + \frac{1}{SNR_{out}}\right)\ mV \quad \text{(Equation 4.12)}$$

Since f_{out} is very weak, this error can get very large. For a high accuracy measurement of absolute membrane potential a long exposure time is required. This considerably limits the time resolution of absolute membrane potential measurements using fluorescence microscopy.

Measurement Accuracy Of Relative Membrane Potential Changes

Although some labs perform the extensive calibrations required for an absolute measurement of the mitochondrial membrane potential from fluorescence[113], in a more typical situation one is only interested in *changes* in the membrane potential in response to an

altered chemical or metabolic condition, or even (more simply) whether the membrane potential has collapsed. Therefore, in most situations it is acceptable to only measure the changes in the intensity of the fluorescence of the organelle as an indicator of the changes in the membrane potential, and ignore the intensity of the fluorescence of the region outside the organelle. Quantitatively, this can be stated as follows: The relative change in the membrane potential can be calculated from:

$$\Delta\psi_2 - \Delta\psi_1 = -59\left(\log\frac{f_{02}}{f_{out2}} - \log\frac{f_{01}}{f_{out1}}\right) = -59\left(\log\frac{f_{02}}{f_{01}} - \log\frac{f_{out2}}{f_{out1}}\right) \quad \text{(Equation 4.13)}$$

$$\Delta\psi_2 - \Delta\psi_1 \approx -59\left(\log\frac{f_{02}}{f_{01}}\right) \quad \text{(Equation 4.14)}$$

For a well-designed experiment, the changes in the TMRM concentration in the buffer is small. The error that is caused by ignoring the $(\log\frac{f_{out2}}{f_{out1}})$ term, will be limited to a few millivolts of membrane potential.

In this case the error in measurement of changes in membrane potential is given by:

$$\partial(\Delta\Psi_2 - \Delta\Psi_1) = 59\frac{1}{ln10}\left(\left|\frac{\partial f_{02}}{f_{02}}\right| + \left|\frac{\partial f_{01}}{f_{01}}\right|\right) = 59\frac{1}{2.3}\left(\frac{1}{SNR_2} + \frac{1}{SNR_1}\right) = 59\frac{1}{2.3}\left(\frac{2}{SNR_{in}}\right) mV$$

(Equation 4.15)

Finally, combining these, we find, for the ideal photo-detector:

$$\partial(\Delta\Psi_2 - \Delta\Psi_1) = \frac{59}{2.3}\left(\frac{2}{55\sqrt{t_0}}\right) \approx \frac{1}{\sqrt{t_0}}\ \text{mV} \quad \text{(Equation 4.16)}$$

This gives the fundamental limits of the accuracy of fluorescence measurement of membrane potential changes (Figure 4.8 (b)). In this case, the measurement error is caused only by the inherent shot noise of the arriving photons, and therefore cannot be improved.

In a practical fluorescence microscopy set-up, the accuracy of the measurement can be found from:

$$\partial(\Delta\Psi_2 - \Delta\Psi_1) = \frac{59}{2.3}\left(\frac{2\sqrt{f_0.M.t_0.Q_e + N_R^2 + D.M.t_0}}{f_0.M.t_0.Q_e}\right) \quad \text{(Equation 4.17)}$$

This accuracy depends on the characteristics of the detection system. Using a high binning mode, the effect of read noise can be suppressed considerably at the price of loss of spatial resolution of mitochondria. Another factor limiting the temporal resolution of the camera system is the frame rate, which also improves using a higher binning mode. The parameters for several different scientific grade low light camera systems are summarized in Table 4.2. The measurement accuracy for these camera systems in their working integration times are plotted in Figure 4.8 (c). In this analysis we have ignored the time it takes for TMRM molecules to diffuse across the mitochondrial membrane in response to changes in the membrane potential. This rate can also limit the temporal resolution of membrane potential measurement with fluorescence microscopy.

Table 4.2. Specifications of different low light camera systems.

Camera	QE	D (e/p/s)	N_R (e/p)	Pixel Size (um)	Fast Frame rate at 512x512 pixel (f/s)	Largest Binning (pixels)	Spatial Resolution of mitochondria with binning
QIClick	0.55	1.5	8	6.45x6.45	~80	8x8	1x1 (pixels)
QIClick Data Sheet: http://www.qimaging.com/products/datasheets/QIClick.pdf							
HQ2	0.62	0.001	4.5	6.45x6.45	81	8x8	1X1 (pixels)
HQ2 data sheet: http://www.photometrics.com/products/datasheets/HQ2.pdf							
iXon 897	0.92	0.001	<1	16x16	206	4x4	1x1(pixels)
iXon 897 data sheet: http://www.andor.com/pdfs/specifications/Andor_iXon_897_Specifications.pdf							
Flash2.8	0.52		3	3.63	236 (1920x240 pixels)	2x2	8x8 (pixels)
Flash 2.8: http://www.hamamatsu.com/us/en/community/life_science_camera/product/search/C11440-10C/index.html							
Flash4.0	0.7	0.06	1.9	6.5x6.5	400	4x4	2x2 (pixels)
https://www.hamamatsu.com/us/en/community/life_science_camera/product/search/C11440-22CU/index.html							

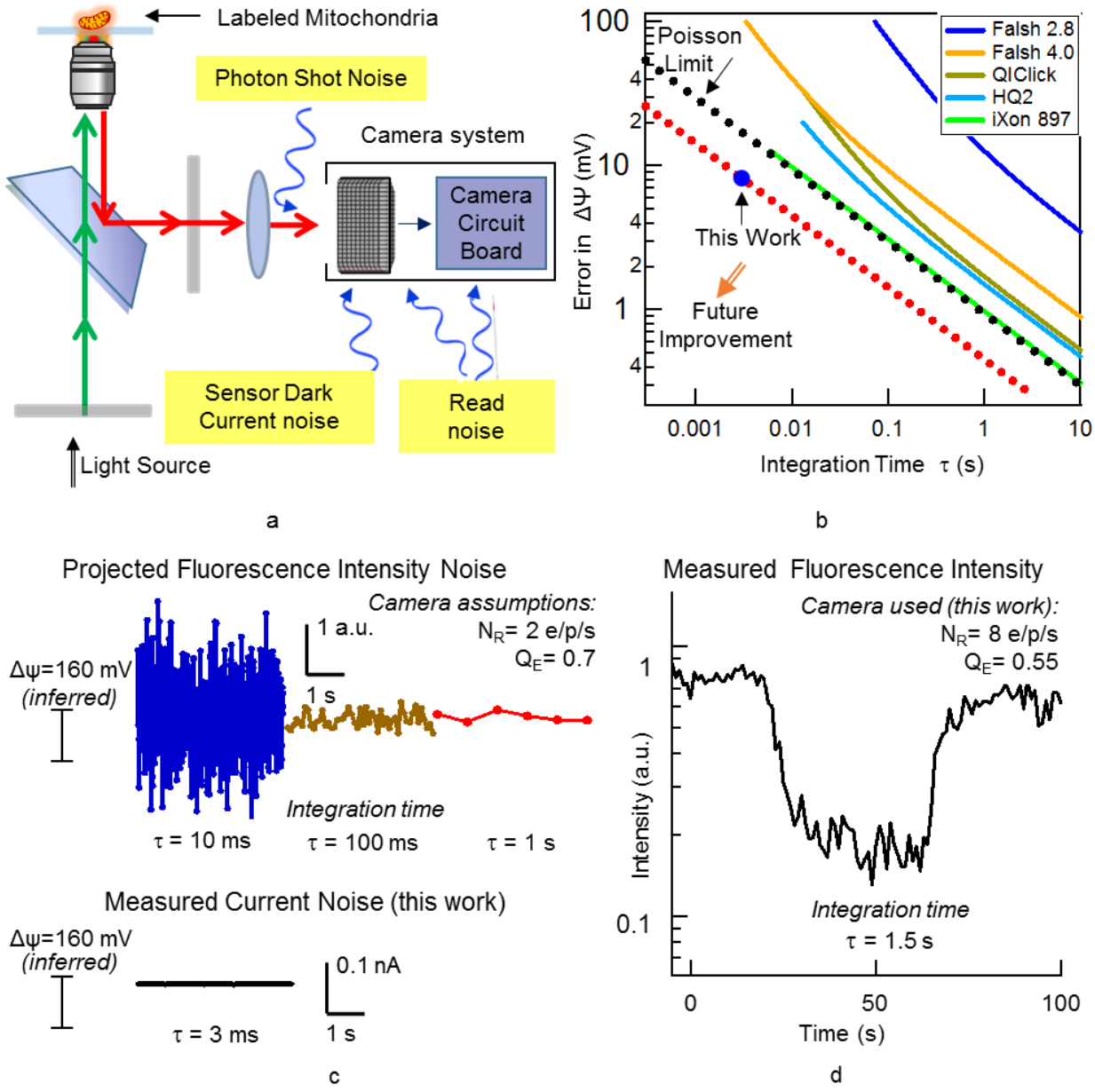

Figure 4.8. Fuorescence measurement of mitochondrial membrane potential. (a) System schematics and sources of measurement noise. (b) Membrane Potential Measurement error versus integration time for different cameras compared to the shot noise limit (black dotted line) and electrical measurement noise of the fabricated devices (red dotted line). (c) Simulated (projected) time traces for measured flourescence intensity with different integration times and the electricaly measured current of the nanoelectrodes. (d) Measured Fluorescence time trace for a single flickering mitochondria. Fluorescence measurement we performed on individual mitochondria (Figure 6d) using the set up described in the methods section shows an SNR of approximately 5.4, resulting in an error of 10 mV, which is in good agreement with the predictions of the derived formula (12 mV).

Discussion

Normalized simulated time traces for measured flourescence intensity for different integration times (Figure 4.8 (c)) and the electricaly measured current versus time of the nanoelectrodes and the membrane potential error versus integration time plot for these two methods clearly indicate that the nanoelectrode device in the set-up reported in this work achieves a better measurement error compared to the fluorescence microscopy. Furthermore, even our prototype results are not obtainable by fluorescence microscopy due to the shot noise limit of the photons. By optimizing the device design and measurement conditions, we anticipate that further improvement in the electrical measurement; ultimately, the electronic sampling frequency can be increased as high as the cut-off frequency of the nanotube transistor, which can be in the GHz range.

This work shows for the first time that single isolated mitochondria can be directly detected by changes in conductance of carbon nanotube devices, as mitochondria flow one by one over the carbon nanotubes in a microfluidic channel. The surface charge of mitochondria induces a change in the threshold voltage of the carbon nanotubes that leads to changes in the transistor conductance. The magnitude of this conductance change depends on the energization state of the mitochondria and therefore can be used as a method for rapid, label free assessment of mitochondria membrane potential. Our analysis reveals that electrical measurements of membrane potential provides orders of magnitude higher time resolution and accuracy compared to the conventional method of fluorescence microscopy for study of the membrane potential of isolated mitochondria. This work is a step towards high resolution, high throughput measurements of single mitochondria bioenergetics.

Methods

Device fabrication

4 inch quartz wafer is cleaned with hot Piranha solution for one hour, followed by carbon nanotube deposition according to the procedure described in[98] . In short, the cleaned quartz wafer is immersed in 1% 3-aminopropyltriethoxy silane (APTES) in isopropanol solution for one hour. This treatment creates a monolayer of amine terminated silane on the surface. This monolayer helps with selective absorption of semiconductive carbon nanotubes. The quartz wafer is then rinsed with isopropanol and purified 99% semicunductiong carbon nanotube solution (IsoNanotubes-S 99%, Nanointegris Inc) is drop-casted on the surface. The CNT solution is left on the surface for 1 hour. Subsequently the wafer is rinsed with DI water and baked in a 60^{o} C oven overnight. The Ti(5 nm)/Pd (15 nm)/Au (30 nm) electrodes are deposited by E-beam evaporation and patterned by liftoff procedure using PMGI SF6 and Microposit SC 1827 (MicroChem Corp) photoresists. Fluidic channels are fabricated by soft lithography of Polydimethylsiloxane (PDMS). Silicone elastomer and curing agent (Sylgard® 184, Dow Corning Co.) are mixed at a 10:1 ratio, degassed and poured over a silicon mold. The mold is placed in a 60° C curing oven overnight. After curing, PDMS is cut and peeled off from the mold. Inlet reservoir and outlet hole are punched, followed by exposure of the PDMS channels to 70 W Oxygen plasma. This treatment takes 30 seconds and turns the PDMS from hydrophobic to hydrophilic; this improves the bond with the quartz wafer and also enhances the fluid flow by capillary force. The PDMS chip is immersed in methanol immediately after the oxygen plasma treatment. Then the PDMS channel is placed on the quartz wafer and manually aligned under a microscope. Methanol lowers the friction

between the CNT device and the PDMS, enabling the alignment without PDMS sticking to the substrate and damaging the transistor device. After the alignment the methanol evaporates and the PDMS bonds to the quartz wafer. The device is baked at 60^0 C for 30 minutes to improve the bonding.

The PDMS channel consists of a 2 µm wide, 1 µm long, 500 µm long flow channel, connected to two wider (100 µm) access channels with a 70 µl inlet reservoir and an outlet hole to introduce the liquid. The access channel lengths are 2cm. Different source-drain electrodes widths and gaps ranging from 3 to 20 µm have been fabricated.

Electrical Measurement

For conductance versus time measurements, 10 mv AC voltage at 10 KHz is applied between the drain-source electrodes and the current is measured using an SR-830 lock-in amplifier. The integration time is set at 3 ms. Therefore 3 ms is the 1/e time to detect abrupt changes in the nanoelectrode conductance, and is the rate limiting step in our existing setup. A custom built semiconductor parameter analyzer was used to measure the DC transport curve of the devices.

Yield and statistics

15 devices were tested using this procedure, out of which 5 devices displayed sensitivity to flow of mitochondria. 9 devices failed due to leakage, carbon nanotubes not gating or high measurement noise. One device was tested with carboxylate modified polystyrene bead, and showed sensitivity to flow of the beads.

In our experiments, the measured noise of the nanoelectrode devices varied from device to device. Results reported here are from devices with SNR values of 1600 to 270 at a time

constant of 3 ms (in the described measurement conditions). The factors contributing to this noise requires further analysis and is not discussed in this study.

Cell Culture and Mitochondria Isolation

Mitochondria were isolated from the human cervical cancer cell line HeLa (ATCC, CCL-2). The adherent cells were cultured and maintained in log growth phase in media consisting of EMEM (ATCC, 30-2003) supplemented with 10% FBS (Invitrogen, 10438-018) and 1% Penicillin-Streptomycin (ATCC, 30-2300). All other chemicals were obtained from Sigma Aldrich, unless otherwise noted. The mitochondrial isolation protocol is described in more details in Appendix I. Briefly, cells were harvested at 100% confluence in a T-75 flask. Approximately $8x10^6$ cells were pelleted and washed in Phosphate Buffered Saline. Ice-cold H-buffer (210 mM mannitol, 70 mM sucrose, 1 mM EGTA, 5 mM HEPES, 0.5% BSA, pH adjusted to 7.2 with 1M KOH) was used in all of the following isolation steps. The cells were physically sheared with 20 passes in an ice-cold dounce homogenizer and centrifuged at low speed (800 x g for 5 min) at 4° C in an Eppendorf 5417R centrifuge. The cell lysate was further purified for the removal of cell debris through 2 additional rounds of low speed spins. The resulting supernatant was subjected to 2 rounds of high speed centrifugation (10,000 x g for 20 min). BSA-free H-buffer was used to re-suspend the resulting pellet, which was spun again at high speed. The isolated mitochondrial sample was pelleted and diluted in ice-cold respiration buffer (225 mM Mannitol, 75 mM Sucrose, 10 mM KCl, 10 mM Tris-HCl, 5 mM KH2PO4, pH adjusted to 7.2 with 1M KOH) and used. 1:1, 1:2, 1:10 dilutions of the suspension were used in protein determination with the BCA Protein Assay Kit (Thermo Scientific, 23227).

Fluorescence Imaging

For Fluorescence assays of membrane potential mitochondria were labeled with TMRM (Life Technologies) in non-quench mode. TMRM was dissolved in DMSO and added to the mitochondrial respiration buffer to a final concentration of 30 nM. Mitochondria were incubated with TMRM for 20 minutes prior to imaging. Mitochondria were imaged with Olympus IX71 inverted fluorescence microscope, equipped with a 12 bit monochromatic CCD camera (QIClick-F-M-12), a 60x, 0.7 NA objective, 120 W Mercury vapor excitation light source and standard FITC (490 nm-525 nm) and TRITC (557 nm-576 nm) filters. Image analysis was performed with ImageJ software.

Mitochondrial injection into channel

50 µL respiration buffer is pipetted inside the reservoir, the capillary force carries the buffer inside the channel resulting in a flow rate of approximately 0.01 µl/hr. Mitochondria are isolated from cells through a differential centrifugation process described in the methods section and suspended in the respiration buffer. Mitochondria suspension and other reagents are pipetted into the same reservoir. To reduce the electrical measurement noise syringe pump is not used.

The exposure time required to image the flowing mitochondria is long, therefore it is not possible to image the mitochondria as they are flowing past the CNT device; but we had previously developed a method to decrease the height of the flow channel to 500 nm and trap the mitochondria inside the flow channel.[114] This method allowed us to verify that mitochondria enter the channel one by one and they remain vital and functional.

Acknowledgements

This work was supported in part by the following grants awarded to D.C.W.: NIH-AG24373, NS21328, AG13154, DK73691, CIRM Comprehensive Grant RC1-00353, and a Doris Duke Clinical Interface Grant 2 005 057. P.B. acknowledges support of this work from NIH National Cancer Institute Grant 1R21CA143351-01, as well as support from the ARO (MURI W911NF-11-1-0024. Ted Pham is supported by the National Science Foundation Lifechips Integrative Graduate Education and Research Traineeship 0 549 479.

CHAPTER 5 : Summary and Future Proposals

Summary of Findings and Conclusions

The aim of this project was to develop technologies based on microfluidics to analyze mitochondria. These studies led to several critical advancements in terms of technology and science.

First in chapter 2, a wafer-scale mitochondrial functional assay lab-on-a-chip devices was developed. This ion-selective device requires mitochondrial protein quantities three orders of magnitude less than current commercial ion-selective electrodes and is integrated onto 4" standard silicon wafer with new fabrication processes and materials. This new fabrication procedure results in increases in production yield and decreases in total cost of fabrication. Membrane potential changes of isolated mitochondria from various well-established cell lines such as human HeLa cell line (Heb7A), human osteosarcoma cell line (143b) and mouse skeletal muscle tissue were investigated and compared.

Next, In chapter 3, we used nanofluidic channels in PDMS of cross section 500 nm x 2 μm, to trap and interrogate individual, isolated mitochondria for the fisrt time. Fluorescence labeling revealed the immobilization of mitochondria at discrete locations along the channel. Interrogation of mitochondrial membrane potential with different potential sensitive dyes (JC-1 and TMRM) indicated that the trapped mitochondria are vital in the respiration buffer. Fluctuations of the membrane potential were observed at the single mitochondrial level. A variety of chemical challenges was delivered to each individual mitochondrion in the nanofluidic system. A variety of applications in cancer biology, stem cell biology, apoptosis studies and high throughput functional metabolomics studies can be envisioned using this technology.

In chapter 4, a new technic for mitochondrial membrane potential measurement was introduced. High sensitivity label free detection of single isolated mitochondria using carbon nanotubes was demonstrated. Electrical measurement of the conductance of carbon nanotube transistors shows that the device conductance is sensitive to flow of mitochondria and changes discretely as individual mitochondria flow over the nanoelectrodes in a microfluidic channel. This conductance change is induced by the electrostatic effects of mitochondrial surface charge and the magnitude of conductance change depends on the bioenergetic state of the mitochondria. Using this method, fluctuations of the mitochondrial membrane potential can be measured with a resolution of 10 mV (inferred) in a measurement time of order milliseconds. A quantitative analysis of the practical and fundamental limits of traditional fluorescence based probes of membrane potential was performed and revealed that fluorescence assays are an order of magnitude slower in ideal, photon shot noise limited setups, and two orders of magnitude slower under typical operating conditions, as compared to the electronic measurement presented here in.

The reason this speed increase is significant is that mitochondrial depolarization is known to involve a large membrane pore that opens transiently in response to a variety of biochemical and pharmacological inputs as well as stress, ROS, and DNA damage. However, the mechanism of the large pore opening, its pharmacological regulation, and even its molecular identity are unknown and controversial. Therefore, this technique can enable higher resolution studies of this pore, and allow for studies of its dynamic opening and closing, flickering of the membrane potential, and statistics, all classical approaches for electrophysiolgical studies of ion channels that (to date) could not be applied to mitochondria because of their small size and the slow speed of fluorescent based voltage dyes. Collapse of

the membrane potential caused by pore opening controls cell fate through the apoptosis pathway. In fact, resistance to apoptosis in response to cell death signals (cytokines, oxidative stress, DNA damage, etc.) is a hallmark of cancer. Collapse of the membrane potential caused by pore opening controls cell fate through the apoptosis pathway. the molecular identity of the membrane protein complex(es) that cause inner membrane depolarization is not known[33,83,115,116]. The inner membrane is thought to depolarize due to the dimerization of ATP synthase. Screening of mitochondrial depolarization is a possible method to screen for new chemotherapy drugs.

Future Proposals

Here I will be describing the future steps and directions that will improve each of the three developed devices.

The integrated lab on a chip ion-selective sensor described in chapter 2, in the current state can already be used reliably to assay the membrane potential of mitochondria. However integration of a mechanism to control the temperature of the chamber will allow us to perform the experiments at body temperature and will be very useful for some applications.

For the nanofluidic platform introduced in chapter 3, implementing a fluidic delivery system instead of the two access channels currently used, will make it possible to introduce a different type and concentration of metabolites into each of the trap channels. Such a device will have great potential applications in drug discovery.

Detailed analysis of the noise generation mechanisms in the nanoelectrode device described in chapter 4, is useful to optimize the device design and experiment conditions for fast, high-throughput, high-resolution single mitochondria membrane potential assays. Based

on our current experiments, it is likely that the dominant component of the measured noise, is the flicker noise of the carbon nanotubes and seems to increase with the density of the deposited CNTs. Optimizing the carbon nanotube density or using a different nanomaterial, such as graphene will enable mitochondrial membrane potential measurements with even higher sensitivity. Also performing a series of experiments with these devices on mitochondria in different metabolic states might lead to new understanding of mitochondrial membrane surface charge distribution, a topic that is still controversial.

Finally, another possible future direction is to merge the two devices described in chapters 3 and 4 to trap individual mitochondria on top of the nanoelectrode sensor and perform time lapse electrical measurements of membrane potential (or simultaneous electrical and fluorescence assays). This approach is especially beneficial for mitochondrial flickering and PTP opening studies, and to understand the role of photo toxicity in the observed flickering.

Appendix I.Mitochondria Isolation Protocol

Cells were harvested at 100% confluence in a T-75 flask on the days of experiment. Approximately 8x106 cells were pelleted and washed in Phosphate Buffered Saline. Ice-cold H-buffer (210 mM mannitol, 70 mM sucrose, 1 mM EGTA, 5 mM HEPES, 0.5% BSA, pH adjusted to 7.2 with 1M KOH) was used in all of the following isolation steps. The cells were physically sheared with 20 passes in an ice-cold dounce homogenizer and centrifuged at low speed (800 x g for 5 min) at 4° C in an Eppendorf 5417R centrifuge. The cell lysate was further purified for the removal of cell debris through 2 additional rounds of low speed spins. The resulting supernatant was subjected to 2 rounds of high speed centrifugation (10,000 x g for 20 min). BSA-free H-buffer was used to resuspend the resulting pellet, which was spun again at high speed. The isolated mitochondrial sample was pelleted and diluted in ice-cold respiration buffer (225 mM Mannitol, 75 mM Sucrose, 10 mM KCl, 10 mM Tris-HCl, 5 mM KH2PO4, pH adjusted to 7.2 with 1M KOH) and used. 1:1, 1:2, 1:10 dilutions of the suspension were used in protein determination with the BCA Protein Assay Kit (Thermo Scientific, 23227).

	KCl	NaCl	$MgCl_2$	Mannitol	Sucrose	KH_2PO_4	Buffer	pH	EGTA	ATP	ADP	Subs.
A[67]	10	x	x	225	75	5	10 Tris/HCl	7.2	x	x	x	x
B	110	x	10	x	x	x	20 MOPS	7.5	1	10	x	Sodium Succina
C.[62]	140	10	2	x	x	0.5	20 HEPES	7.2	0.5	x	added later	added later
D	110	15	1	x	x	2	5 HEPES	7.2-7.4	x	x	x	x
E	x	x	1	220	75	2	5 HEPES	7.4	x	x	x	x
F	x	x	x	x	250	2	5 MOPS	7.4	x	x	x	x
G	125	x	1	x	x	2	5 HEPES	7.2-7.4	x	x	x	x

Table AI: Incubation buffers for isolated mitochondria (All units are in mM, except for pH)

TableA1 description: Through the course of technology development, we investigated several respiration buffers to see which one is best suited for our purpose of using the fluorescent dyes TMRM, Mitotracker Green, and JC-1. Listed in table A1 are the compositions for seven buffers used in the literature. Also included is the color-coded explanation of the role of each ingredient. The results reported in the thesis were based on either buffer A or buffer B. We observed that the mitochondria incubated with buffer B yielded higher fluorescence signal than those incubated with buffer A, probably due to the presence of 10 mM of sodium succinate, which is the substrate for complex II of the electron transport chain. However, the use of buffer B is limiting to experimentation because it already contains substrates of OXPHOS. The low intensity signal obtained from using buffer A prompted us to test other buffers. We have tested buffer C, a composition with similar ionic strength to buffer B and did not see a significant difference in signal intensity. The interesting result was that addition of Succinate and ADP would cause high amplitude flickering of mitochondria membrane potential whereas addition of small concentrations of Calcium (50 nM) into the buffer would suppress the flickering. Buffers D, E, F and G were adapted from OXPHOS.org.

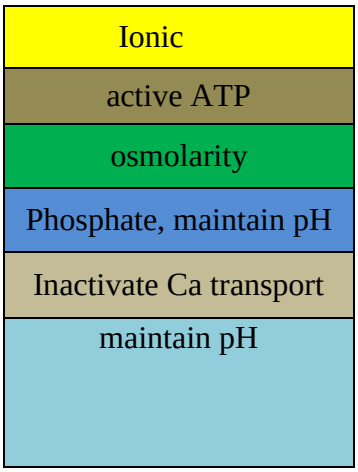

Appendix II. Carbon Nanotube Deposition

Recipe 1, Using APTES

1. Piranha clean the substrate for 1 hour at 120 ^{0} C, Piranha solution consists of Sulfuric Acid : Hydrogen peroxide (3:1)
2. Dry the substrate with N_2, dehydrate for a few minutes
3. Make a 1% APTES solution in isopropanol (IPA), immerse the wafer in the solution for an hour.
4. Take the substrate out of the solution, rinse with IPA, dry with nitrogen, place in another container, drop cast the Nanointegris 99% semiconducting CNT solution on the surface (approximately 100 µl for 1 cm^2 area).
5. Leave the solution on the surface for 1 hour.
6. Rinse with water very gently.
7. Leave in 60^0 C oven overnight to dehydrate.

Recipe 2, Vacuum Filtration

1. Dilute Nanointegris CNT solution to 1 µg/mL in a combination of water and 1% w/v sodium dodecyl (SDS). Sonicate for 30 minutes.
2. Using a vacuum filtration apparatus, pass 250 µL of the diluted solution through an MCE filter.
3. A thin film of CNTs will accumulate on the surface. Allow the resulting film to set for 15 minutes.

4. Gently rinse the film with 200 mL of water.
5. Allow the film to set again for at least 2 hours.
6. Dip the CNT coated filter in ethanol.
7. Press the filter, film side down on the substrate and immediately suspend over a bath of boiling acetone. Acetone gradually dissolves the filter. Let sit for about 1 hour until the filter is no longer visible.
8. Place the substrate in a stirred bath of acetone for 30 minutes to remove MCE residue.
9. Transfer the substrate to a stirred bath of methanol for 15 minutes.
10. Gently dry the film with N_2.
11. Bake for 1-2 hours.

Appendix III. CNT-Nanochannel Device Fabrication

Photolithography and Lift-off

4 inch quartz wafer is cleaned with hot Piranha solution for one hour, followed by carbon nanotube deposition according to the procedures described in Appendix II.

Photolithography is done with PMGI SF6 lift-off photoresist and Shipley 1827 photoresist. Use MF319 Developer. (Detail photolithography procedure described below.)

The Ti(5 nm)/Pd (15 nm)/Au (30 nm) electrodes are deposited by E-beam evaporation and patterned by liftoff procedure, in PG remover. Heat the PG remover to 60^{o} C on hotplate. Leave the substrate in PG remover overnight, rinse with IPA. Immerse the wafer in IPA for a few hours. Rinse with IPA and dry with N_2.

Lift Off procedure with PMGI (SF6):

1. Substarte Preparation: (HMDS typically not required)
   1.1. Solvent cleaning or rinse with diluted acid
   1.2. Rinse with DI water
   1.3. Dehydrate at 200^{0} C for 5min on hot plate.
2. Coating Process, (The PMGI film should be thicker than the metal deposition thickness. typically 1.2 - 1.33 times the thickness of the metal film.)
   2.1. Dispense 3ml of SF6 on 4" wafer 10 min before spin coat.
   2.2. Spin at 3500 rpm for 45 s (ramping 500 rpm/s)
   2.3. Prebake at 150-170 ^{0}C for 5 min, on hotplate

3. Apply Shipley as usual/ prebake/expose(gap 55 um?)
4. Develop in MF-319 , rinse in DI water, blow dry
5. E-beam evaporation
6. Lift-off : Immerse in Microchem Remover PG for overnight

Shipley 1827 photolithography procedure

1. Spin coat (~ 2.7 µm thick):

   1.1. 500 rpm for 5 sec

   1.2. 3500 rpm for 35 sec (ramp rate 500 rpm/s)

2. Soft-bake: 90^{o} C hot oven for 30 min
3. Exposure: 150 mV/cm2 (Expose 25 sec with 6 mW/cm^2)
4. Develop: . MF319, No dilution needed, Develop for 30 sec to 1 min with gentle stirring, Rinse with DI water

Fluidic Channel Fabrication and Device Assembly

Fluidic channels are fabricated by soft lithography of Polydimethylsiloxane (PDMS) over a Si mold. The mold is fabricated by photolithography of Shipley 1827 on Si wafer. Use adhesion promoter; leave the piranha cleaned wafer in HMDS oven for one hour right before spin coating the photoresist, use low exposure dose 140 mJ/cm^2-150 mJ/cm^2 and hard or vacuum contact. Monitor the developing process to make sure nanochannels don't get dissolved. Use Dektak to measure the height of channels.

Silicone elastomer and curing agent (Sylgard® 184, Dow Corning Co.) are mixed at a 10:1 ratio, degassed for 30 min and poured over the salinized silicon mold to a thickness of 3-4 mm. The mold is placed in a 60° C curing oven overnight. Use a few drops of Sigmacote on the mold for 15 minutes prior to pouring the PDMS to salinize the mold.

After curing, PDMS is cut and peeled off from the mold. Inlet reservoir and outlet hole are punched, followed by exposure of the PDMS channels to 70 W Oxygen plasma for 30s at 200 mTorr. This treatment turns the PDMS from hydrophobic to hydrophilic; improves the bond with the quartz wafer and also enhances the fluid flow by capillary force.

The PDMS chip is immersed in methanol immediately after the oxygen plasma treatment. Then the PDMS channel is placed on the quartz wafer and manually aligned under a microscope. Methanol lowers the friction between the CNT device and the PDMS, enabling the alignment without PDMS sticking to the substrate and damaging the transistor device. After the alignment the methanol evaporates and the PDMS bonds to the quartz wafer. The device is baked at 60^0 C for 30 minutes to improve the bonding.

Flow the liquid inside the channel and run the experiment within 1-2 hour of bonding, monitor the liquid inside the channel to make sure it does not evaporate during the experiment.

REFERENCES

1. Krauss, S. Mitochondria: Structure and Role in Respiration. In *eLS*; John Wiley & Sons, Ltd, 2001; pp. 1–6.

2. Mannella, C. a Structure and Dynamics of the Mitochondrial Inner Membrane Cristae. *Biochim. Biophys. Acta* **2006**, *1763*, 542–8.

3. Tait, S. W. G.; Green, D. R. Mitochondria and Cell Signalling. *J. Cell Sci.* **2012**, *125*, 807–15.

4. Whelan, S. P.; Zuckerbraun, B. S. Mitochondrial Signaling: Forwards, Backwards, and in Between. *Oxid. Med. Cell. Longev.* **2013**, *2013*, 351613.

5. Rizzuto, R.; Stefani, D. De; Raffaello, A.; Mammucari, C. Mitochondria as Sensors and Regulators of Calcium Signalling. *Nat. Rev. Mol. Cell Biol.* **2012**, *13*, 566–78.

6. Alberts, B.; Johnson, A.; Lewis, J.; Raff, M.; Roberts, K.; Walter, P. Programmed Cell Death (Apoptosis). In *Molecular Biology of the Cell*; Garland Science: New York, 2002.

7. Tait, S. W. G.; Green, D. R. Mitochondria and Cell Death: Outer Membrane Permeabilization and Beyond. *Nat. Rev. Mol. Cell Biol.* **2010**, *11*, 621–32.

8. Perry, S. W.; Norman, J. P.; Barbieri, J.; Brown, E. B.; Gelbard, H. a Mitochondrial Membrane Potential Probes and the Proton Gradient: a Practical Usage Guide. *Biotechniques* **2011**, *50*, 98–115.

9. Duchen, M. R. Mitochondria in Health and Disease: Perspectives on a New Mitochondrial Biology. *Mol. Aspects Med.* **2004**, *25*, 365–451.

10. Chance, B.; Williams, G. R. Respiratory Enzymes in Oxidative Phosphorylation. *J Biol Chem* **1955**, *217*, 409–428.

11. Gnaiger, E. *Mitochondrial Pathways and Respiratory Control. An Introduction to OXPHOS Analysis*; 3rd ed.; Mitochondr Physiol Network 17.18. OROBOROS MiPNet Publications, 2012; p. 64.

12. Wallace, D. C.; Lott, M. T.; Procaccio, V. Mitochondrial Genes in Degenerative Diseases, Cancer and Aging. In *Emery and Rimoin's Principles and Practice of Medical Genetics*; Rimoin, D. L.; Connor, J. M.; Pyeritz, R. E.; Korf, B. R., Eds.; Churchill Livingstone Elsevier: Philadelphia, PA, 2007; Vol. Volume 1,, pp. 194–298.

13. Wallace, D. C. A Mitochondrial Paradigm of Metabolic and Degenerative Diseases, Aging, and Cancer: A Dawn for Evolutionary Medicine. *Annu. Rev. Genet.* **2005**, *39*, 359–407.

14. Wallace, D. C. Bioenergetic Origins of Complexity and Disease. *Cold Spring Harb. Symp. Quant. Biol.* **2011**, *76*, 1–16.

15. Votyakova, T. V; Reynolds, I. J. DeltaPsi(m)-Dependent and -Independent Production of Reactive Oxygen Species by Rat Brain Mitochondria. *J. Neurochem.* **2001**, *79*, 266–77.

16. Elliott, H. R.; Samuels, D. C.; Eden, J. A.; Relton, C. L.; Chinnery, P. F. Pathogenic Mitochondrial DNA Mutations Are Common in the General Population. *Am. J. Hum. Genet.* **2008**, *83*, 254–260.

17. Galluzzi, L.; Zamzami, N.; La Motte Rouge, T. de; Lemaire, C.; Brenner, C.; Kroemer, G. Methods for the Assessment of Mitochondrial Membrane Permeabilization in Apoptosis. *Apoptosis* **2007**, *12*, 803–813.

18. Lemasters, J. J.; Ramshesh, V. K.; Liza, A. P.; Eric, A. S. Imaging of Mitochondrial Polarization and Depolarization with Cationic Fluorophores. In *Methods in Cell Biology*; Academic Press, 2007; Vol. Volume 80, pp. 283–295.

19. Lim, T.-S.; Davila, A.; Wallace, D. C.; Burke, P. J. Assessment of Mitochondrial Membrane Potential Using an on-Chip Microelectrode in a Microfluidic Device. *Lab Chip* **2010**, *10*, 1683–1688.

20. Zare, R.; Kim, S. Microfluidic Platforms for Single-Cell Analysis. *Annu. Rev. Biomed. Eng.* **2010**, *12*, 187–201.

21. Nagrath, S.; Sequist, L. V; Maheswaran, S.; Bell, D. W.; Ryan, P.; Balis, U. J.; Tompkins, R. G.; Haber, D. A. Isolation of Rare Circulating Tumour Cells in Cancer Patients by Microchip Technology. *Nature* **2011**, *450*, 1235–1239.

22. Hahm, J.; Lieber, C. M. Direct Ultrasensitive Electrical Detection of DNA and DNA Sequence Variations Using Nanowire Nanosensors. *Nano Lett.* **2004**, *4*, 51–54.

23. Tang, X.; Bansaruntip, S.; Nakayama, N.; Yenilmez, E.; Chang, Y.-L.; Wang, Q. Carbon Nanotube DNA Sensor and Sensing Mechanism. *Nano Lett.* **2006**, *6*, 1632–6.

24. Choi, Y.; Moody, I. S.; Sims, P. C.; Hunt, S. R.; Corso, B. L.; Perez, I.; Weiss, G. a; Collins, P. G. Single-Molecule Lysozyme Dynamics Monitored by an Electronic Circuit. *Science* **2012**, *335*, 319–24.

25. Wang, W. U.; Chen, C.; Lin, K.; Fang, Y.; Lieber, C. M. Label-Free Detection of Small-Molecule-Protein Interactions by Using Nanowire Nanosensors. *Proc. Natl. Acad. Sci. U. S. A.* **2005**, *102*, 3208–12.

26. Lin, T.-W.; Hsieh, P.-J.; Lin, C.-L.; Fang, Y.-Y.; Yang, J.-X.; Tsai, C.-C.; Chiang, P.-L.; Pan, C.-Y.; Chen, Y.-T. Label-Free Detection of Protein-Protein Interactions Using a Calmodulin-Modified Nanowire Transistor. *Proc. Natl. Acad. Sci. U. S. A.* **2010**, *107*, 1047–52.

27. Stern, E.; Klemic, J. F.; Routenberg, D. a; Wyrembak, P. N.; Turner-Evans, D. B.; Hamilton, A. D.; LaVan, D. a; Fahmy, T. M.; Reed, M. a Label-Free Immunodetection with CMOS-Compatible Semiconducting Nanowires. *Nature* **2007**, *445*, 519–22.

28. Patolsky, F.; Zheng, G.; Hayden, O.; Lakadamyali, M.; Zhuang, X.; Lieber, C. M. Electrical Detection of Single Viruses. *Proc. Natl. Acad. Sci. U. S. A.* **2004**, *101*, 14017–22.

29. Patolsky, F.; Timko, B. P.; Yu, G. H.; Fang, Y.; Greytak, A. B.; Zheng, G. F.; Lieber, C. M. Detection, Stimulation, and Inhibition of Neuronal Signals with High-Density Nanowire Transistor Arrays. *Science (80-.).* **2006**, *313*, 1100–1104.

30. Gao, R.; Strehle, S.; Tian, B.; Cohen-Karni, T.; Xie, P.; Duan, X.; Qing, Q.; Lieber, C. M. Outside Looking in: Nanotube Transistor Intracellular Sensors. *Nano Lett.* **2012**, *12*, 3329–33.

31. Solaini, G.; Sgarbi, G.; Lenaz, G.; Baracca, A. Evaluating Mitochondrial Membrane Potential in Cells. *Biosci Rep* **2007**, *27*, 11–21.

32. Apte, S. P.; Sarangarajan, R. *Cellular Respiration and Carcinogenesis*; Humana Press Springer: New York City, 2009.

33. Kroemer, G.; Galluzzi, L.; Brenner, C. Mitochondrial Membrane Permeabilization in Cell Death. *Physiol. Rev.* **2007**, *87*, 99–163.

34. Galluzzi, L.; Larochette, N.; Zamzami, N.; Kroemer, G. Mitochondria as Therapeutic Targets for Cancer Chemotherapy. *Oncogene* **2006**, *25*, 4812–4830.

35. Rustin, P.; Kroemer, G. Mitochondria and Cancer. *Ernst Shering Found. Symp. Proc.* **2008**, *4*, 1–21.

36. Galluzzi, L.; Vitale, I.; Kepp, O.; Seror, C.; Hangen, E.; Perfettini, J. L.; Modjtahedi, N.; Kroemer, G. Methods to dissect mitochondrial membrane permeabilization in the course of apoptosis. In *Programmed Cell Death, General Principles for Studying Cell Death, Pt A*; Elsevier Academic Press Inc: San Diego, 2008; Vol. 442, pp. 355–374.

37. Kamo, N.; Muratsugu, M.; Hongoh, R.; Kobatake, Y. Membrane Potential of Mitochondria Measured with an Electrode Sensitive to Tetraphenyl Phosphonium and Relationship Between Proton Electrochemical Potential and Phosphorylation Potential in Steady State. *J. Membr. Biol.* **1979**, *49*, 105–121.

38. Rottenberg, H. Membrane Potential and Surface Potential in Mitochondria: Uptake and Binding of Lipophilic Cations. *J. Membr. Biol.* **1984**, *81*, 127–138.

39. Labajova, A.; Vojtiskova, A.; Krivakova, P.; Kofranek, J.; Drahota, Z.; Houstek, J. Evaluation of Mitochondrial Membrane Potential Using a Computerized Device with a Tetraphenylphosphonium-Selective Electrode. *Anal. Biochem.* **2006**, *353*, 37–42.

40. Zolkiewska, A.; Zabocka, B.; Duszynski, J.; Wojtczak, L. Resting State Respiration of Mitochondria: Reappraisal of the Role of Passive Ion Fluxes. *Arch. Biochem. Biophys.* **1989**, *275*, 580–590.

41. Remedi, M. S.; Nichols, C. G.; Koster, J. C. The Mitochondria and Insulin Release: Nnt Just a Passing Relationship. *Cell Metab.* **2006**, *3*, 5–7.

42. Kuznetsov, A. V; Margreiter, R. Heterogeneity of Mitochondria and Mitochondrial Function Within Cells as Another Level of Mitochondrial Complexity. *Int. J. Mol. Sci.* **2009**, *10*, 1911–29.

43. Anand, R. K.; Chiu, D. T. Analytical Tools for Characterizing Heterogeneity in Organelle Content. *Curr. Opin. Chem. Biol.* **2012**, *16*, 1–9.

44. Lim, T.-S.; Davila, A.; Zand, K.; Wallace, D. C.; Burke, P. J. Wafer-Scale Mitochondrial Membrane Potential Assays. *Lab Chip* **2012**, *12*, 2719–2725.

45. Douglas, M. B.; Michael, D. W. *Fundamentals of Light Microscopy and Electronic Imaging*; 2nd ed.; Wiley-Blackwell, 2012.

46. Born, M.; Wolf, E. *Principles of Optics*; 6th ed.; Cambridge university press, 1998; pp. 387–397.

47. Pendergrass, W.; Wolf, N.; Poot, M. Efficacy of MitoTracker Green and CMXrosamine to Measure Changes in Mitochondrial Membrane Potentials in Living Cells and Tissues. *Cytometry. A* **2004**, *61*, 162–9.

48. Presley, A. D.; Fuller, K. M.; Arriaga, E. A. MitoTracker Green Labeling of Mitochondrial Proteins and Their Subsequent Analysis by Capillary Electrophoresis with Laser-Induced Fluorescence Detection. *J. Chromatogr. B* **2003**, *793*, 141–150.

49. Cossarizza, A.; Ceccarelli, D.; Masini, A. Functional Heterogeneity of an Isolated Mitochondrial Population Revealed by Cytofluorometric Analysis at the Single Organelle Level. *Exp. Cell Res.* **1996**, *222*, 84–94.

50. Keil, V. C.; Funke, F.; Zeug, A.; Schild, D.; Müller, M. Ratiometric High-Resolution Imaging of JC-1 Fluorescence Reveals the Subcellular Heterogeneity of Astrocytic Mitochondria. *Pflugers Arch.* **2011**, *462*, 693–708.

51. Klima, J. *Cytologie Eine Einf. F. Studierende D. Naturwiss. U. Medizin*; Stuttgart G. Fischer , 1967.

52. Qin, D.; Xia, Y.; Whitesides, G. M. Soft Lithography for Micro- and Nanoscale Patterning. *Nat. Protoc.* **2010**, *5*, 491–502.

53. Liang, X.; Chou, S. Y. Nanogap Detector Inside Nanofluidic Channel for Fast Real-Time Label-Free DNA Analysis. *Nano Lett.* **2008**, *8*, 1472–6.

54. Xia, D.; Yan, J.; Hou, S. Fabrication of Nanofluidic Biochips with Nanochannels for Applications in DNA Analysis. *Small* **2012**, *8*, 2787–801.

55. Duffy, D. C.; McDonald, J. C.; Schueller, O. J.; Whitesides, G. M. Rapid Prototyping of Microfluidic Systems in Poly(dimethylsiloxane). *Anal. Chem.* **1998**, *70*, 4974–84.

56. Vergun, O.; Votyakova, T. V; Reynolds, I. J. Spontaneous Changes in Mitochondrial Membrane Potential in Single Isolated Brain Mitochondria. *Biophys. J.* **2003**, *85*, 3358–3366.

57. Hattori, T.; Watanabe, K.; Uechi, Y.; Yoshioka, H.; Ohta, Y. Repetitive Transient Depolarizations of the Inner Mitochondrial Membrane Induced by Proton Pumping. *Biophys. J.* **2005**, *88*, 2340–2349.

58. Cossarizza, A.; Ceccarelli, D.; Masini, A. Functional Heterogeneity of an Isolated Mitochondrial Population Revealed by Cytofluorometric Analysis at the Single Organelle Level. *Exp. Cell Res.* **1996**, *222*, 84–94.

59. Lecoeur, H.; Chauvier, D.; Langonné, A.; Rebouillat, D.; Brugg, B.; Mariani, J.; Edelman, L.; Jacotot, E. Dynamic Analysis of Apoptosis in Primary Cortical Neurons by Fixed- and Real-Time Cytofluorometry. *Apoptosis* **2004**, *9*, 157–69.

60. McGill, A.; Frank, A.; Emmett, N.; Turnbull, D. M.; Birch-Machin, M. a; Reynolds, N. J. The Anti-Psoriatic Drug Anthralin Accumulates in Keratinocyte Mitochondria, Dissipates Mitochondrial Membrane Potential, and Induces Apoptosis through a Pathway Dependent on Respiratory Competent Mitochondria. *FASEB J.* **2005**, *19*, 1012–4.

61. Duchen, M. R. Transient Mitochondrial Depolarizations Reflect Focal Sarcoplasmic Reticular Calcium Release in Single Rat Cardiomyocytes. *J. Cell Biol.* **1998**, *142*, 975–988.

62. Huser, J.; Blatter, L. A. Fluctuations in Mitochondrial Membrane Potential Caused by Repetitive Gating of the Permeability Transition Pore. *Biochem. J.* **1999**, *343*, 311–317.

63. Kurz, F. T.; Aon, M. a; O'Rourke, B.; Armoundas, A. a Spatio-Temporal Oscillations of Individual Mitochondria in Cardiac Myocytes Reveal Modulation of Synchronized Mitochondrial Clusters. *Proc. Natl. Acad. Sci. U. S. A.* **2010**, *107*, 14315–20.

64. Nicholls, D. G. Fluorescence Measurement of Mitochondrial Membrane Potential Changes in Cultured Cells. *Methods Mol. Biol.* **2012**, *810*, 119–33.

65. Buckman, J. F.; Reynolds, I. J. Spontaneous Changes in Mitochondrial Membrane Potential in Cultured Neurons. *J. Neurosci.* **2001**, *21*, 5054–5065.

66. Halestrap, A. The Regulation of the Matrix Volume of Mammalian Mitochondria in Vivo and in Vitro and Its Role in the Control of Mitochondrial Metabolism. *Biochim. Biophys. Acta* **1989**, *973*, 355–82.

67. Trounce, I. A.; Kim, Y. L.; Jun, A. S.; Wallace, D. C. Assessment of Mitochondrial Oxidative Phosphorylation in Patient Muscle Biopsies, Lymphoblasts, and Transmitochondrial Cell Lines. *Methods Enzymol.* **1996**, *42*, 484–508.

68. Huser, J.; Rechenmacher, C. E.; Blatter, L. A. Imaging the Permeability Pore Transition in Single Mitochondria. *Biophys. J.* **1998**, *74*, 2129–2137.

69. Uechi, Y.; Yoshioka, H.; Morikawa, D.; Ohta, Y. Stability of Membrane Potential in Heart Mitochondria: Single Mitochondrion Imaging. *Biochem. Biophys. Res. Commun.* **2006**, *344*, 1094–1101.

70. Higuchi, Y.; Miura, T.; Kajimoto, T.; Ohta, Y. Effects of Disialoganglioside GD3 on the Mitochondrial Membrane Potential. *FEBS Lett.* **2005**, *579*, 3009–13.

71. Medina, J. M.; López-Mediavilla, C.; Orfao, A. Flow Cytometry of Isolated Mitochondria During Development and Under Some Pathological Conditions. *FEBS Lett.* **2002**, *510*, 127–132.

72. Lecoeur, H.; Langonné, A.; Baux, L.; Rebouillat, D.; Rustin, P.; Prévost, M.-C.; Brenner, C.; Edelman, L.; Jacotot, E. Real-Time Flow Cytometry Analysis of Permeability Transition in Isolated Mitochondria. *Exp. Cell Res.* **2004**, *294*, 106–17.

73. Strack, A.; Duffy, C. F.; Malvey, M.; Arriaga, E. A. Individual Mitochondrion Characterization: A Comparison of Classical Assays to Capillary Electrophoresis with Laser-Induced Fluorescence Detection. *Anal. Biochem.* **2001**, *294*, 141–147.

74. Fuller, K. M.; Arriaga, E. A.; Ã, E. A. A. Advances in the Analysis of Single Mitochondria. *Curr. Opin. Biotechnol.* **2003**, *14*, 35–41.

75. Duffy, C. F.; MacCraith, B.; Diamond, D.; O'Kennedy, R.; Arriaga, E. A. Fast Electrophoretic Analysis of Individual Mitochondria Using Microchip Capillary Electrophoresis with Laser Induced Fluorescence Detection. *Lab Chip* **2006**, *6*, 1007–1011.

76. Johnson, R. D.; Navratil, M.; Poe, B. G.; Xiong, G.; Olson, K. J.; Ahmadzadeh, H.; Andreyev, D.; Duffy, C. F.; Arriaga, E. A. Analysis of Mitochondria Isolated from Single Cells. *Anal. Bioanal. Chem.* **2007**, *387*, 107–118.

77. Kostal, V.; Arriaga, E. A. Recent Advances in the Analysis of Biological Particles by Capillary Electrophoresis. *Electrophoresis* **2008**, *29*, 2578–2586.

78. Kostal, V.; Katzenmeyer, J.; Arriaga, E. A. Capillary Electrophoresis in Bioanalysis. *Anal. Chem.* **2008**, *80*, 4533–4550.

79. Wallace, D. C. Colloquium Paper: Bioenergetics, the Origins of Complexity, and the Ascent of Man. *Proc. Natl. Acad. Sci. U. S. A.* **2010**, *107*, 8947–53.

80. Galluzzi, L.; Maiuri, M. C.; Vitale, I.; Zischka, H.; Castedo, M.; Zitvogel, L.; Kroemer, G. Cell Death Modalities: Classification and Pathophysiological Implications. *Cell Death Differ.* **2007**, *14*, 1237–43.

81. Wallace, D. C. Mitochondria and Cancer. *Nat. Rev. Cancer* **2012**, *12*, 685–698.

82. Sarosiek, K. A.; Ni Chonghaile, T.; Letai, A. Mitochondria: Gatekeepers of Response to Chemotherapy. *Trends Cell Biol.* **2013**, *23*, 612–619.

83. Bernardi, P. The Mitochondrial Permeability Transition Pore: a Mystery Solved? *Front. Physiol.* **2013**, *4*, 95.

84. Duchen, M. R.; Leyssens, A.; Crompton, M. Transient Mitochondrial Depolarizations Reflect Focal Sarcoplasmic Reticular Calcium Release in Single Rat Cardiomyocytes. *J. Cell Biol.* **1998**, *142*, 975–988.

85. Diaz, G. Homogeneous Longitudinal Profiles and Synchronous Fluctuations of Mitochondrial Transmembrane Potential. *FEBS Lett.* **2000**, *475*, 218–224.

86. Krippeit-drews, P.; Du, M.; Drews, G.; D¸fer, M. Parallel Oscillations of Intracellular Calcium Activity and Mitochondrial Membrane Potential in Mouse Pancreatic B-Cells. *Biochem. Biophys. Res. Commun.* **2000**, *267*, 179–183.

87. Aon, M. a; Cortassa, S.; Marbán, E.; O'Rourke, B. Synchronized Whole Cell Oscillations in Mitochondrial Metabolism Triggered by a Local Release of Reactive Oxygen Species in Cardiac Myocytes. *J. Biol. Chem.* **2003**, *278*, 44735–44.

88. O'Reilly, C. M.; Fogarty, K. E.; Drummond, R. M.; Tuft, R. a; Walsh, J. V Spontaneous Mitochondrial Depolarizations Are Independent of SR Ca2+ Release. *Am. J. cell Physiol.* **2004**, *286*, C1139–51.

89. Falchi, A. M.; Isola, R.; Diana, A.; Putzolu, M.; Diaz, G. Characterization of Depolarization and Repolarization Phases of Mitochondrial Membrane Potential

Fluctuations Induced by Tetramethylrhodamine Methyl Ester Photoactivation. *FEBS J.* **2005**, *272*, 1649–59.

90. Vergun, O.; Reynolds, I. J. Distinct characteristics of Ca(2+)-induced depolarization of isolated brain and liver mitochondria. In *Biochimica et biophysica acta*; 2005; Vol. 1709, pp. 127–37.

91. Nicholls, D. G. Fluorescence Measurement of Mitochondrial Membrane Potential Changes in Cultured Cells. *Methods* **2012**, *810*, 119–133.

92. Schwarzländer, M.; Logan, D. C.; Johnston, I. G.; Jones, N. S.; Meyer, A. J.; Fricker, M. D.; Sweetlove, L. J. Pulsing of Membrane Potential in Individual Mitochondria: A Stress-Induced Mechanism to Regulate Respiratory Bioenergetics in Arabidopsis. *Plant Cell* **2012**, *24*, 1188–1201.

93. Gerencser, A. a; Adam-Vizi, V. Mitochondrial Ca2+ Dynamics Reveals Limited Intramitochondrial Ca2+ Diffusion. *Biophys. J.* **2005**, *88*, 698–714.

94. Wang, Y. Y.; Pham, T. D.; Zand, K.; Li, J.; Burke, P. J. Charging the Quantum Capacitance of Graphene with a Single Biological Ion Channel. *ACS Nano* **2014**, *8*, 4228–4238.

95. Lim, T.-S.; Jain, D.; Burke, P. J. Biomembrane-Gated Carbon Nanotube Transistor as a Sensing Platform. *Proc. 15th Int. Conf. Miniaturized Syst. Chem. Life Sci.* **2011**, 1770–1772.

96. Lim, T.-S.; Jain, D.; Burke, P. J. Fabrication of Supported Lipid Bilayer (SLB) and Nanotube Transistor Hybrid Biosensing Platform Using Microfluidic Channels. *Proc. 11th IEEE Conf. Nanotechnol.* **2011**, 371–373.

97. Lim, T.-S.; Jain, D.; Burke, P. J. Protein Nanopore-Gated Bio-Transistor for Membrane Ionic Current Recording. *Proc. 69th Device Res. Conf.* **2011**, *26*, 131–132.

98. Rouhi, N.; Jain, D.; Zand, K.; Burke, P. J. Fundamental Limits on the Mobility of Nanotube-Based Semiconducting Inks. *Adv. Mater.* **2011**, *23*, 94–99.

99. Rouhi, N.; Jain, D.; Burke, P. J. High-Performance Semiconducting Nanotube Inks: Progress and Prospects. *ACS Nano* **2011**, *5*, 8471–8487.

100. Rosenblatt, S.; Yaish, Y.; Park, J.; Gore, J.; Sazonova, V.; McEuen, P. L. High Performance Electrolyte Gated Carbon Nanotube Transistors. *Nano Lett.* **2002**, *2*, 869–872.

101. Trounce, I.; Neill, S.; Wallace, D. C. Cytoplasmic Transfer of the mtDNA Nt 8993 T--> G (ATP6) Point Mutation Associated with Leigh Syndrome into mtDNA-Less Cells

Demonstrates Cosegregation with a Decrease in State III Respiration and ADP/O Ratio. *Proc. Natl. Acad. Sci.* **1994**, *91*, 8334.

102. Heller, I.; Janssens, A. M.; Mannik, J.; Minot, E. D.; Lemay, S. G.; Dekker, C. Identifying the Mechanism of Biosensing with Carbon Nanotube Transistors. *Nano Lett.* **2008**, *8*, 591–595.

103. Dukhin, A. S. Biospecific Mechanism of Double Layer Formation and Peculiarities of Cell Electrophoresis. **1993**, *13*, 29–48.

104. Kamo, N.; Muratsugu, M.; Kurihara, K.; Kobatake, Y. Change in Surface Charge Density and Membrane Potential of Intact Mitochondria During Energization. *FEBS Lett.* **1976**, *72*, 247–50.

105. Dukhin, a S.; Ulberg, Z. R.; Karamushka, V. I.; Gruzina, T. G. Peculiarities of Live Cells' Interaction with Micro- and Nanoparticles. *Adv. Colloid Interface Sci.* **2010**, *159*, 60–71.

106. Loew, L. M.; Tuft, R. A.; Carrington, W.; Fay, F. S. Imaging in Five Dimensions: Time-Dependent Membrane Potentials in Individual Mitochondria. *Biophys. J.* **1993**, *65*, 2396–407.

107. Scaduto, R. C.; Grotyohann, L. W. Measurement of Mitochondrial Membrane Potential Using Fluorescent Rhodamine Derivatives. *Biophys. J.* **1999**, *76*, 469–77.

108. Zorov, D. B.; Filburn, C. R.; Klotz, L. O.; Zweier, J. L.; Sollott, S. J. Reactive Oxygen Species (ROS)-Induced ROS Release: a New Phenomenon Accompanying Induction of the Mitochondrial Permeability Transition in Cardiac Myocytes. *J. Exp. Med.* **2000**, *192*, 1001–14.

109. Kenmoku, S.; Urano, Y.; Kojima, H.; Nagano, T. Development of a Highly Specific Rhodamine-Based Fluorescence Probe for Hypochlorous Acid and Its Application to Real-Time Imaging of Phagocytosis. *J. Am. Chem. Soc.* **2007**, *129*, 7313–8.

110. Kaasik, A.; Safiulina, D.; Zharkovsky, A.; Veksler, V. Regulation of Mitochondrial Matrix Volume. **2007**, 157–163.

111. Applications, S. *Handbook of Single-Molecule Biophysics*; Hinterdorfer, P.; Oijen, A., Eds.; Springer US: New York, NY, 2009.

112. Waters, J. C. Accuracy and Precision in Quantitative Fluorescence Microscopy. *J. Cell Biol.* **2009**, *185*, 1135–48.

113. O'Reilly, C. M.; Fogarty, K. E.; Drummond, R. M.; Tuft, R. A.; Walsh, J. V Quantitative Analysis of Spontaneous Mitochondrial Depolarizations. *Biophys. J.* **2003**, *85*, 3350–7.

114. Zand, K.; Pham, T.; Davila, A.; Wallace, D. C.; Burke, P. J. Nanofluidic Platform for Single Mitochondria Analysis Using Fluorescence Microscopy. *Anal. Chem.* **2013**, *85*, 6018–25.

115. Giorgio, V.; Stockum, S. von; Antoniel, M.; Fabbro, A.; Fogolari, F.; Forte, M.; Glick, G. D.; Petronilli, V.; Zoratti, M.; Szabó, I.; *et al.* Dimers of Mitochondrial ATP Synthase Form the Permeability Transition Pore. *Proc. Natl. Acad. Sci.* **2013**, *110*, 5887–5892.

116. Kokoszka, J. E.; Waymire, K. G.; Levy, S. E.; Sligh, J. E.; Cai, J.; Jones, D. P.; MacGregor, G. R.; Wallace, D. C. The ADP/ATP Translocator Is Not Essential for the Mitochondrial Permeability Transition Pore. *Nature* **2004**, *427*, 461–465.